HV Transmission Line and Tower Inspection Safe-Fly Zone Modelling and Metrology

by

Matthew Groch

Thesis presented in partial fulfilment of the requirements for the degree Master of Engineering (Research) in the Faculty of Engineering at Stellenbosch University

Supervisor: Professor Howard Charles Reader

Department of Electrical & Electronic Engineering

December 2013

Declaration

By submitting this thesis electronically, I declare that the entirety of the work contained therein is my own, original work, that I am the sole author thereof (save to the extent explicitly otherwise stated), that reproduction and publication thereof by Stellenbosch University will not infringe any third party rights and that I have not previously in its entirety or in part submitted it for obtaining any qualification.

December 2013

Abstract

The deployment of Unmanned Aerial Vehicles (UAV) for power line inspection requires the definition of safe-fly zones. Transient Over-Voltages (TOVs) on the Overhead Transmission Lines (OHTLs) put the UAV at risk if it encroaches on these zones.

In order to determine the safe-fly zones of a UAV in the vicinity of OHTLs, realistic full-scale experimental tests are done. Non-linearity in breakdown effects renders small-scale testing and computational work inaccurate. Experimental work is used to describe the close-up approach distances for worst-case scenarios. Testing cannot provide a full solution due to the limitation of the equipment available. Further tests must therefore be done at a specialised facility.

Experiments are run in two phases, namely non-linear and linear tests in the High Voltage (HV) laboratory. The non-linear tests are done to derive Minimum Approach Distances (MAD). The linear experiments are used to calibrate FEKO, the simulation tool, to the measurement environment. Once correlation between the linear test data and the simulated data is found, confidence is derived in both the simulation model and the test setup. The simulations can then be used to determine a geometric factor as an input into F. Rizk's prediction equations.

The Rizk equations are used to describe the safe-fly zones alongside OHTLs as an addition to the non-linear experimental work. Along with the standard's suggestions, the Rizk predictions are formulated in such a way that line-specific solutions can be determined. The suggested clearance values are provided in terms of per unit values, which can be selected in accordance with historical line data.

Power line sparking is investigated to better understand the line radiation phenomenon. This understanding could assist in the line inspection process, as well as in the layout of power lines near radio quiet areas. Knowledge of OHTL radiation patterns can aid in the location of corona and sparking sources in the inspection process.

Aerial sparking measurements are taken using a UAV carrying a spectrum analyser. Measured sparking levels are used to verify a Computational Electromagnetic (CEM) model. The CEM model can then be used to further investigate OHTL radiation characteristics.

Opsomming

Die aanwending van Onbemande Vliegtuie (UAVs) vir kraglyn inspeksies, vereis die definiëring van veilige vlieg sones. Oorspannings (TOVs) op oorhoofse kraglyne (OHTLs) kan hierdie vliegtuie in gevaar stel as hulle die grense van hierdie sones oorskry.

Om die veilige vlieg sones van 'n UAV in die omgewing van OHTLs te bepaal, is realistiese volskaalse toetse gedoen. Die nie-lineariteit in afbreek effekte lewer onakkurate kleinskaal toetse en rekenaar werk. Eksperimentele werk word gebruik om die benaderde afstande vir die ergste geval te beskryf. Hierdie werk kan nie 'n volledige oplossing gee nie as gevolg van ‘n beperking op huidige toerusting. Dit beteken dat verdere toetse, by ‘n meer gespesialiseerde fasiliteit, gedoen moet word.

Eksperimente is uitgevoer in twee fases: nie-lineêre en lineêre toetse in die Hoogspannings (HV) laboratorium. Die nie-lineêre toetse word gedoen om die kleinste-benaderde-afstand (MAD) af te lei en die lineêre eksperimente word gebruik om FEKO (‘n numeriese elektromagnetika simulasie program) met die metings omgewing te kalibreer. Sodra daar ‘n korrelasie tussen die lineêre data en die gesimuleerde data is, kan daar aangeneem word dat die simulasie model en die toets-opstelling betroubaar is. Die simulasies kan dan gebruik word om 'n meetkundige faktor te bepaal as 'n bydrae tot F. Rizk se voorspellings vergelykings.

Die Rizk vergelykings word gebruik om die veilige vlieg sones langs die OHTLs te beskryf. Dit kan dus gebruik word as ‘n toevoeging tot die nie-lineêre eksperimentele werk. Saam met die normale meet standaard voorstellings, is die Rizk voorspellings geformuleer sodat dit die lyn spesifieke oplossings kan bepaal. Die voorgestelde verklarings waardes word in per eenheid waardes beskryf, wat dan gekies kan word met ooreenstemmende historiese lyn data.

Kraglyn-vonke word ondersoek om die lyn-bestraling verskynsel beter te verstaan. Hierdie begrip kan in die lyn inspeksie proses en in die uitleg van kraglyne naby radiostilte-areas help. Kennis van OHTL bestralings patrone kan help met die identifisering van corona en vonk-bronne tydens die inspeksie proses.

'n UAV met 'n aangehegte spektrum analiseerder is gebruik om die lug-vonkende metings te neem. Vonk vlakke wat gemeet is word dan gebruik om 'n Numeriese Elektromagnetiese (CEM) model te bevestig. Die CEM model kan dan gebruik word om OHTL bestralings eienskappe verder te ondersoek.

Acknowledgements

I would like to express my sincerest gratitude to Professor H.C. Reader for taking me on as a Masters student, and guiding me throughout the course of this thesis. His insightful discussions and critical evaluation of work were invaluable.

To Mr. Petrus Pieterse, I express thanks for his many hours of assistance in the high voltage laboratory. His broad knowledge in the field made measurements with limited resources possible.

I thank Ls Telcom of South Africa for their assistance in the aerial sparking measurements. The hard-working team consisting of Brian, Jan and Wessel really went the extra mile, in challenging conditions, to provide me with useable data.

I would like to thank Professor K.D. Palmer for his input regarding the antenna design and help acquiring the necessary materials.

I would like to acknowledge ESKOM TESP and OMICRON Electronics GMBH for funding this project.

Many thanks go to:

- Professor Matthys Botha for his help with FEKO.
- Dr. K. Holtzhausen for his involvement in procuring the equipment for the high voltage laboratory.
- My colleagues in Room E212, who created a stimulating working environment. It has been a great experience being part of the EMRIN group.
- Dr. Braam Otto, Dr. Gideon Wiid and Dr. Paul Van der Merwe for their willingness to share their knowledge and experience.
- Mr. Nardus Matthysen for translating my Abstract.
- Mr. Wessel Croukamp and the workshop staff for help in constructing the antennas, repairing the spark gap, and for giving me practical advice in general.

Lastly, I would like to express thanks to my wonderful mother for her unequivocal support throughout my studies. Without you none of this would have been possible.

In loving memory of my father, Andy Groch

Table of Contents

List of Figures

List of Tables

Nomenclature

AC	Alternating Current
ADC	Analogue to Digital Converter
AF	Antenna Factor
BIL	Basic Insulation Level
BSL	Basic Switching Level
CDF	Cumulative Distribution Function
CEM	Computational Electromagnetics
CFO	Critical Flashover
dB	Decibel
DC	Direct Current
DMI	Digital Measurement Instrument
EM	Electromagnetic
EMC	Electromagnetic Compatibility
EMI	Electromagnetic Interference
ESC	Electronic Speed Controller
FEM	Finite Element Method
GPS	Global Positioning System
HF	High Frequency
HV	High Voltage
IEC	International Electro-technical Commission
IEEE	Institute of Electrical and Electronics Engineers

IF	Intermediate Frequency
KML	Key-Markup Language
LG	Line-to-Ground
LL	Line-to-Line
LNA	Low Noise Amplifier
MAD	Minimum Approach Distance
MAID	Minimum Air Insulation Distance
MHAD	Minimum Helicopter Approach Distance
MOM	Method of Moments
MTID	Minimum Tool Insulation Distance
OHS	Occupational Health and Safety
OHTL	Overhead Transmission Line
RBW	Resolution Bandwidth
RFI	Radio Frequency Interference
SA	Spectrum Analyser
SFO	Statistical Flashover
STP	Standard Temperature and Pressure
T	Transient (in per unit)
TBD	Time to Breakdown
TOV	Transient Over-Voltage
UAV	Unmanned Aerial Vehicle
USB	Universal Serial Bus

Chapter 1

Introduction

1.1 Project Background

Power utilities across the world employ various inspection techniques to ensure continuity of supply to customers. Depending on the terrain, budget and flight restrictions (as in urban areas) the utility will determine the line inspection method. The most common forms of inspection are undertaken by vehicle, or by helicopter. Both inspection methods have their own distinctive advantages and disadvantages [1].

Helicopter inspections give an accurate assessment of the state of the transmission network because they can get close to live lines [2]. Mounted thermal and corona cameras can be used to detect defects in the OHTL network.

Recent technological developments have seen the use of cable-climbing robots. These are automated devices which are attached to, and move along the OHTLs. Cable-climbing robots are fully equipped with all of the necessary sensors to perform inspections [3].

Motor vehicle inspections have the advantage of a ground-level analysis of: line hardware, foundations, vegetation and resistance (tower footing) measurements. They are, however, a slower form of inspection.

UAV inspection is an attractive alternative because it is a cheaper, safer and faster method. Fixed-wing UAVs can be used to fly power lines for long distances to detect problematic line sections and inspect vegetation clearances.

Once suspect line sections are detected, multi-rotor UAVs can be deployed for a thorough examination. UAV inspection can be used to collect important information in the form of high resolution imagery (Figure 1.1) [4]. This information is important for ascertaining the state of the OHTL network. UAV inspection is already widely practised [4], [5], [6], [7].

(a) (b)

Figure 1.1: (a) UAV inspections afford a (b) detailed analysis of an OHTL network [5].

UAV inspections pose a potential flight problem - the UAV cannot be guaranteed to stick to its flight path due to wind or malfunctioning of the software. It is therefore important to know the airspace in which the UAV is at risk and where safe operation can be guaranteed.

1.2 Thesis Description

This thesis investigates the safe-fly zones for UAV operation in the vicinity of OHTLs. Additionally, power line sparking is investigated. Knowledge of OHTL radiation characteristics can be used to locate corona and sparking sources.

International standards are examined in Chapter 2 to determine MADs for UAV operation in the proximity of OHTLs. The principles governing air breakdown are also investigated as a build-up to air breakdown measurements.

A study of the MADs is presented in Chapter 3 with full-scale model experiments. These experiments are intended to predict the breakdown threshold of air for close-up UAV inspections.

The results of the experiments in Chapter 3 are compared to Rizk's equations in Chapter 4. The Rizk equations are based on empirical data for air insulation strength. With confidence in the measurements and prediction model achieved, the

equations are extended to other cases. Predictions of MADs alongside 132kV and 400kV OHTLs are formulated in such a way that they can be used based on existing line data.

Sparking and corona currents propagate along the line until all of the energy has been attenuated or radiated. Knowledge of the radiation characteristics could be used to locate the sparking or corona sources. This could aid in the OHTL inspection process.

A development of this research is the interest in mitigating OHTL radiation in radio quiet areas. Understanding the radiation characteristics can help in the design stages (layout) of OHTLs.

Chapter 5 deals with the aerial sparking measurements of a 22kV OHTL. The measured data is processed to give an electric field profile of the sparking event. The electric field profile is then compared to a Method of Moments (MOM) CEM solution. Once correlation between the measured and simulated values is achieved, the simulation model is used to investigate the radiation characteristics.

The results of this thesis are summarised in Chapter 6.

1.3 References

[1] Eskom, *The Fundamentals and Practice of Overhead Line Maintenance*, ISBN 0-620-30906-7, Crown Publications CC, March 2004.

[2] IEEE Task Force 15.07.05.05, "Recommended Practices for Helicopter Bonding Procedures for Live-Line Work", *IEEE Trans. Power Del.*, January 2000.

[3] M Nayyerloo et al. (2009). Cable-Climbing Robots for Power Transmission Lines Inspection, Mobile Robots - State of the Art in Land, Sea, Air, and Collaborative Missions, XiaoQiChen (Ed.), ISBN: 978-953-307-001-8, InTech, Available:

http://www.intechopen.com/books/mobile-robots-state-of-the-art-in-land-sea-air-and-collaborativemissions/cable-climbing-robots-for-power-transmission-lines-inspection (URL)

[4] [Online]. Available: Aibotix, http://www.aibotix.com/inspection-of-high-voltage-power lines.html, Last visited September 2013.

[5] [Online]. Available: Aerial Photography Specialists (APS), http://www.apspecialists.com.au/, Last visited September 2013.

[6] [Online]. Available: Serpent UAV, http://www.serpentuav.com/#!inspection-services/c1m77, Last visited September 2013.

[7] [Online]. Available: Microdrones, http://www.microdrones.com, Last visited September 2013.

Chapter 2

A Consideration of Air's Insulation Strength: Theory and Standards.

In this chapter, the principle factors to consider for air insulation tests are introduced. This is to better understand the mechanisms of breakdown to assist in preparing a measurement strategy in Chapter 3. To support these measurements, various international standards are also described in this chapter.

2.1 Factors Affecting Air-Gap Insulation

There are many variables which influence air's insulation strength. This theoretical study introduces the principles pertinent to the HV measurements done in Chapter 3.

2.1.1 The Breakdown Sequence

Corona is a discharge which occurs when the gases dielectric strength is exceeded by the localised electric field gradient. This occurs in an ionised region surrounding the high voltage conductor. Corona creates a conductive air path around the conductor, increasing its radius and dissipating power in the form of light, heat and Electromagnetic Interference (EMI) [1, Sec. 8, pp. 8-2].

Corona inception marks the beginning stages in the cycle of streamer development (Figure 2.1). Corona is, however, not harmful to a UAV and measures can be taken to lower the field gradients on sharp edges and on wires.

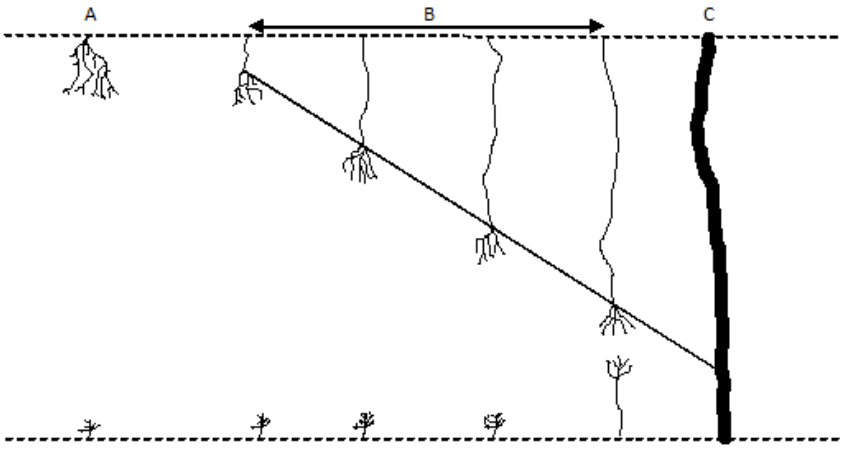

Figure 2.1: This figure shows the stages of streamer development with increasing voltage. Stage A represents corona, stage B shows the streamer development stages and stage C shows full dielectric breakdown (after, [2]).

The stages in the development from corona to full dielectric breakdown are shown in Figure 2.1 for increasing voltage amplitude over time. Corona is initiated first (stage A), followed by streamers (stage B) which propagate along the length of the channel. Full dielectric breakdown occurs in stage C. More information on corona and the breakdown processes can be found in [3].

For switching impulses, the dielectric strength of air between electrodes is dependent on the polarity of the impulse, the wave shape, the weather conditions, and the electrode geometry [1, Sec. 5, pp. 5-2]. A rod-plane electrode configuration for a positive switching impulse has been proven to exhibit the weakest dielectric strength for air gaps [1].

2.1.2 Time to Breakdown

The static voltage level (V_S) of air is the strength at which, disregarding the statistical nature of such an event, there is enough potential across the air gap to induce breakdown [4]. This means that if the statistical nature of the event were to be removed from the equation, each air gap configuration would occur at a constant voltage (the static voltage level) for the same electrodes.

The time that it takes from the instant the static voltage is exceeded to the voltage collapse is called the time to breakdown (TBD). TBD consists of two components (Figure 2.2): a statistical time lag (t_s) and a formative time lag (t_f) [4].

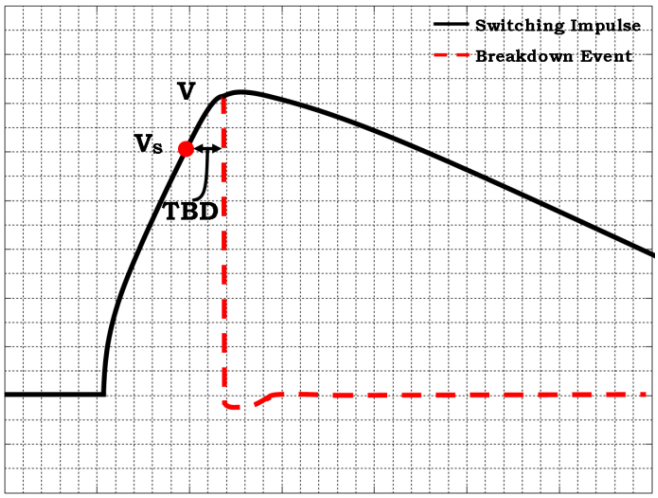

Figure 2.2: A switching impulse for a breakdown event showing the effect of the TBD. If an impulse is shorter than the required TBD, breakdown will not occur.

The statistical time lag is the time required for the initiatory electron to appear following the application of a voltage higher than the static voltage. The formative time lag is the time from the appearance of the initiatory electron to the occurrence of breakdown in the gap [4].

2.1.3 U-Curves – The Wave Front Effect

U-curves show the effect of variable rise time in Critical Flashover (CFO) voltages for switching impulse testing [7]. The CFO is the amplitude which results in a 50% probability of flashover for a given electrode configuration, the gap spacing and ambient air conditions.

A U-curve can be determined by varying the switching impulse's wave front (rise time) and keeping all other factors constant (Figure 2.3).

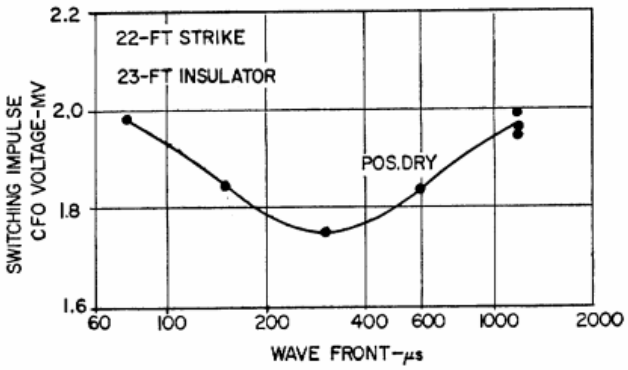

Figure 2.3 Changing the wave front (rise time) of a switching impulse results in different CFO voltages [7].

U-curves can be used to determine the critical front time. A critical front time is the rise time which results in the lowest CFO voltage. The U-curves change for different clearances between electrodes, weather conditions, polarity and electrode configurations [1, Sec. 5.2.3, pp. 5-6]. Standards declare that a switching impulse of 250/2500μs be used for repeatability of testing [6].

2.1.4 Statistical Analysis of Impulse Breakdown Probability

To determine the probability of breakdown for a set air-gap length, electric field stress, and the electrode configuration, the breakdown tests must be performed multiple times. This is because the variability of the breakdown event under apparent similar testing conditions follows a Cumulative Distribution Function (CDF) trend [1].

Two main methods of testing exist. These are the multilevel method, and the up-and-down method [1]. While the multilevel method takes longer to gather data, multiple samples per gap spacing are determined. The probability of breakdown for the multilevel method is determined by [1]:

$$P_{BREAKDOWN} = \frac{N_B}{N_S} \qquad [2.1]$$

According to 2.1, if a total of 10 impulses/strikes (N_S) are applied to the system and 4 breakdowns events (N_B) are recorded, the probability of breakdown ($P_{Breakdown}$) is 40%. To simplify the testing procedure, normal probability paper can be used to plot the probabilities against the breakdown voltage [12].

The probability scale (y-axis) is linearized from the CDF to reduce the number of samples required to predict a trend. A minimum of two samples are required between 10% and 90% to determine the CFO (U_{50}) and the standard deviation (σ).

2.1.5 HV Line and Tower Configurations

OHTLs and tower dimensions are used for the full-scale model measurements. Dimensions can be extracted from standards where electrical clearances are suggested. Long-term satisfactory operations of lines across the world at different altitudes in different conditions provide confidence in these figures.

Insulation co-ordination standards [6] can be used in conjunction with other standards [8], [9], [10] to determine system operating conditions of the OHTL line network for recreation in the HV lab.

Clearances between phase conductors and from phase conductors to earth are of importance in the measurement setup. The clearances defined in Table 2.1 are taken from [9]. These values are used for realistic scale modelling of OHTL systems.

Nominal System Voltage [kV]	Phase-to-Earth Electrical Clearance (m)	Phase-to-Phase Clearance (m)	BIL/BSL (kV)
132	1.1	1.4	550/650
400	2.8	3.6	1425/1050

Table 2.1: Electrical Clearances, as well as the Basic Insulation (BIL) and Switching Levels (BSL) of 132kV and 400kV OHTLs. [9, Table 5.3.5.3]

A phase-to-phase clearance is the minimum clearance distance, in metres, between phase lines carrying impulses of equal magnitude and opposite polarity. The phase-to-earth clearances are the conductor-tower clearances used in the HV lab experiments.

Power utilities incorporate their own safety margins in the design of their transmission networks. Such safety margins would mean a larger clearance is used in the designs of OHTL clearances.

2.2 MAIDs According to International Standards

Aerial safe zones are defined as being the zones in which conductive objects can fly without causing breakdown between the line and the conductive object or vice versa.

Modern standards are written to ensure the protection of transmission lines from helicopters when aerial inspections or maintenance are carried out by power utilities [10], [11], [13].

The Minimum Air Insulation Distance (MAID) gives the insulation strength of air. It is up to the user to incorporate safety factors dependent on the application and confidence in the measurement medium (UAV).

Applicable standards and equations will be examined here to determine the MAID values to compare to HV experiments and analytical predictions.

2.2.1 Switching Surge Prediction Models

Large air gaps are non-linear and very variable. To aptly describe large gap behaviour, empirical data was gathered for different electrode geometries under different humidity, temperature and pressure conditions with different excitation properties [14].

Once the empirical data was gathered, equations were sought to describe the air-gap behaviour to afford OHTL designers control over the variables. Many equations have since been proposed. The most popular of which are compared in this section [1].

The Gallet equation [1] is the most popular of the equations due to its simplicity and timely introduction (2.2):

$$U_{50} = 3400/(1 + 8/L) \qquad [2.2]$$

where U_{50} is the 50% flashover voltage at Standard Temperature and Pressure (STP) for the gap's critical time to crest in kiloVolts (kV). L is the gap length in metres (m). This equation is valid between 1 and 23m.

Kishizima et al. (CRIEPI) improved on the Gallet equation in 1984. This equation (2.3) is valid between 1 and 25m [1].

$$U_{50} = 1080 \cdot \ln(0.46 \cdot L + 1) \qquad [2.3]$$

In 1989, Rizk proposed an equation (2.4) based on continuous leader inception; Rizk's formula is valid for gaps greater than 4m in length [1].

$$U_{50} = ((1830 + 59 \cdot L)/(1 + 3.89/L)) + 92 \qquad [2.4]$$

These three models are compared in Figure 2.4(a) for gaps up to 30m.

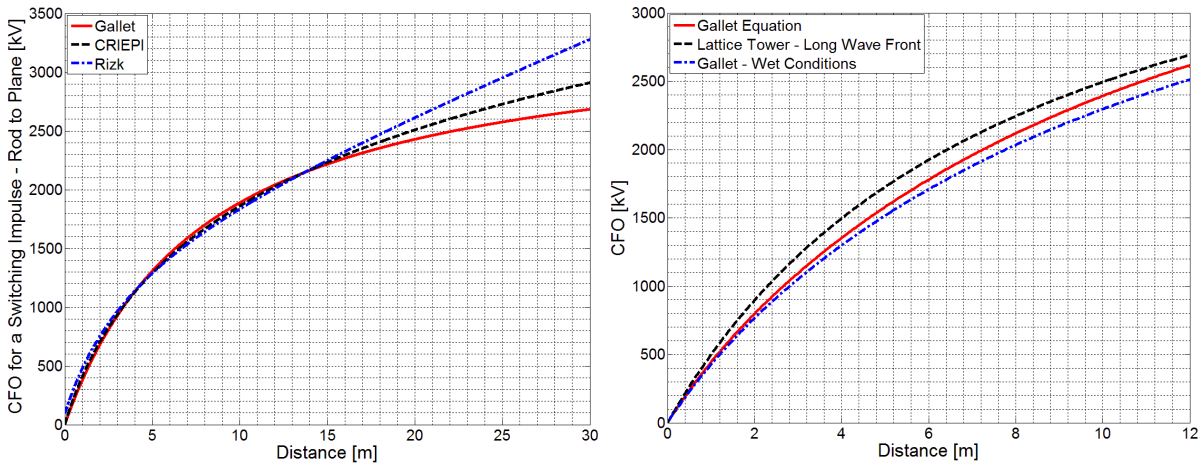

(a) (b)

Figure 2.4: Comparison of the analytical models used to describe large air gap breakdown (critical flashover) up to 30m (a). The ability to modify variables such as weather conditions, rise times and electrodes is demonstrated in (b).

CFO values are easily read off Figure 2.4. For instance, if a transient of 1.5MV is the maximum expected on the line, a distance of 6m will result in the CFO for a rod-plane air gap at STP. This is translatable into MAID values for a specific application with the knowledge of the gap factor (different electrode configurations) [1], the atmospheric conditions and the standard deviation as a function of the gap (demonstrated in Figure 2.4(b)).

IEEE and IEC standards ([11], [13]) are now examined to investigate the MAID values for the OHTLs of interest (132kV and 400kV).

2.2.2 Line-to-Ground Clearances (IEEE)

Line-to-Ground (LG) clearances, as the name suggests, are those clearances between an excited electrode and ground. Examples of LG clearances include a conductor-tower gap, conductor-earth wire gap, and a conductor-floating conductive object gap.

The LG clearances are determined from experimental data to which a modified Gallet equation is fitted to obtain an analytical curve and tables for reference.

The LG distance equation is taken from IEEE Standard 516-2003 [11]:

$$D_{MAID} = 0.3048 * (C_1 + a)(V_{LG})(T)(A) \quad [2.5]$$

Where:

- D_{MAID} – The minimum air insulation distance in metres
- C_1 – 60Hz rod gap withstand (0.01ft/kVrms)
- a – air saturation factor
- T – The maximum anticipated transient overvoltage in per unit
- A – Altitude correction factor.

Figure 2.5 is the IEEE MAID (Equation 2.5) for increasing T. These predictions assume STP conditions.

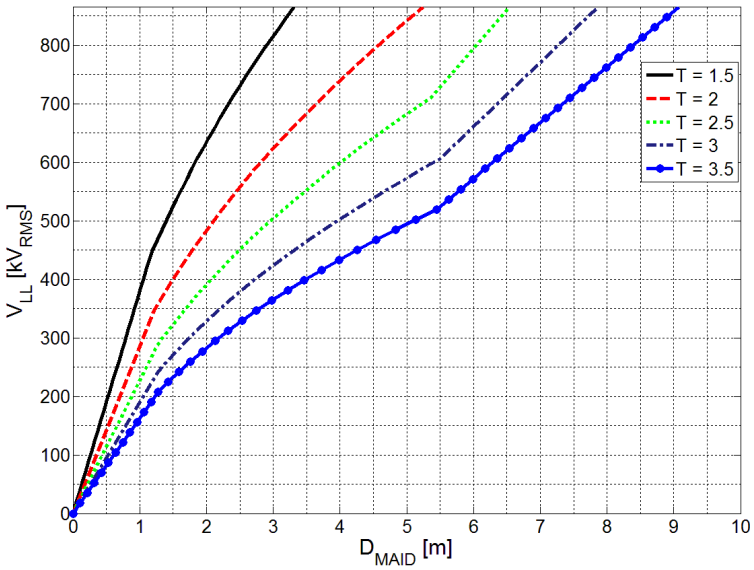

Figure 2.5: The LG MAIDs for varying T factors according to Equation 2.5.

Figure 2.5 shows air's insulation strength as a function of distance for a LG gap as a function of the transient overvoltage in per unit, T.

According to Figure 2.5, the clearance required for all possible transients on a 132kV OHTL is approximately 0.26m to 0.8m; for a 400kV OHTL, the clearance required is approximately 1m to 3.5m.

Where the impinging distance is located depends on the severity of the transient, T. The maximum expected transient can be taken for a section of the OHTL from line studies by the power utility or measured data. It must be noted that the maximum TOV is assumed across the entire line.

2.2.3 Line-to-Line Clearances (IEEE)

Line-to-Line (LL) clearances are the clearances between two excited conductors. A gap factor may also be introduced to describe a gap with a floating conductive object between phase conductors. Such an event may be described by a factor K_F which is incorporated into the modified Gallet equations in IEEE Standard 516-2009 [11, Sec. 4.7.1.4]. The standard suggests a K_F = 0.9 for a large conductive object.

For $V_{LL} \leq 242kV_{RMS}$:

$$D_M = \left(8/\left(4621/\left((1.35)(T) + 0.45\right)(V_{LL})\right) - 1\right)(A) \quad [2.6]$$

For $V_{LL} > 242kV_{RMS}$:

$$D_M = \left(8/\left(4875/\left((1.35)(T) + 0.45\right)(V_{LL})\right) - 1\right)(A) \quad [2.7]$$

In both equations [11]:

- D_M is the striking, or flashover, distance in m
- T is the transient in per unit
- V_{LL} is the OHTL's LL voltage in kV_{RMS}

- A is the altitude correction factor

Equations 2.6 and 2.7 produce Figure 2.6.

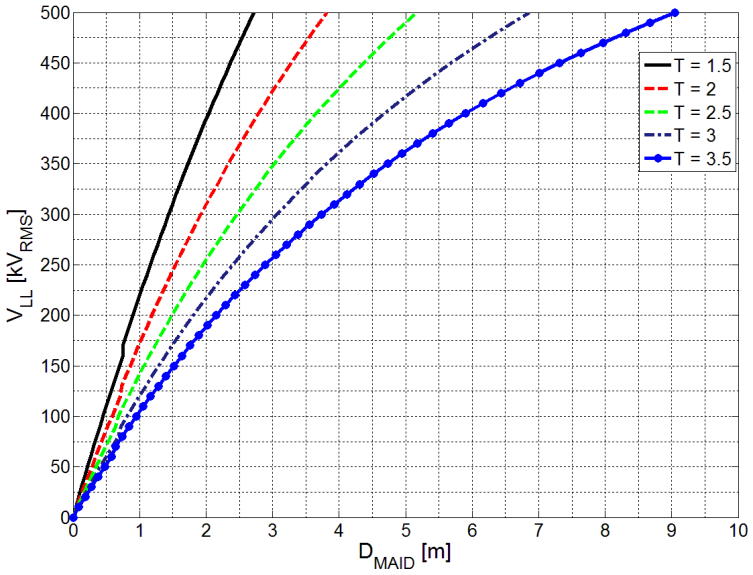

Figure 2.6: The MAID for a LL air gap required to initiate breakdown for the respective T on an OHTL.

Figure 2.6 can be analysed in the same way as its LG counterpart. The severity of the transient, T, of the OHTL determines the required gap spacing, D_{MAID}, to avoid dielectric breakdown between the electrodes. For an OHTL with a system voltage equal to 132kV a spacing in the region of 0.6-1.35m is required. A 400kV OHTL requires an approximate spacing of 2-5.9m.

To factor in the effect of a large, floating, conductive object, a gap factor, K_F, of 0.9 [11] is inserted into Equations 2.6 and 2.7. The effect of the conductive object between phase conductors on the MAID can be seen in Figure 2.7.

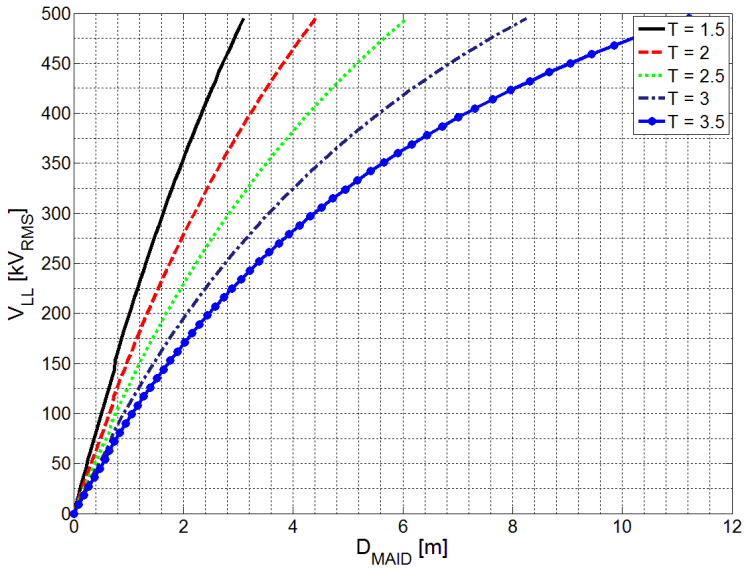

Figure 2.7: The LL air gap T required to initiate breakdown with a conductive object between phase conductors.

The required gap spacing has increased for the 132kV OHTL from (approximately) 0.65-1.35m to 0.68-1.4m. For the 400kV OHTL, the MAID has increased from (approximately) 2-5.9m to 2.3-7.1m.

2.2.4 Safe Approach Distance Prediction by the IEC Standards

The IEC standard uses the CRIEPI formula defined earlier (2.3) to determine the electrical distance. This is in essence the same as the MAID. As the thesis uses the latter, we will use MAID throughout to avoid confusion. The equation is presented again:

$$U_{50RP} = 1080 \cdot \ln(0.46 \cdot d + 1) \qquad [2.8]$$

Equation 2.8 is used to determine the 50% breakdown voltage (CFO) for a rod-plane gap distance, d, in metres. Factors are introduced to modify the equation

from a rod-plane gap to a representation of the work-site air gap. This formula applies only to LG applications.

The variables used in the formulation [13] of the MAIDs are:

- U_2 - 2% statistical overvoltage
- U_{90} - 90% withstand voltage
- U_S - Highest possible voltage in the system
- u_2 - 2% statistical overvoltage in per unit (see Table 2.1)
- k_s - Deviation factor – Typical $k_s = 0.936$ for a 5% deviation
- k_g - Gap factor – electrode dependent
- k_a - Atmospheric factor
- k_f - Floating object factor for the worksite air gap
- k_i - Minimum length of a defective insulator factor
- K_t - $K_t = k_s \cdot k_g \cdot k_a \cdot k_f \cdot k_i$
- K_S - Safety factor – 1.1 suggested
- n_d - Number of defective insulators
- n_o - Number of sound insulators, and
- F - Length of the floating object along the gap axis.

The factor k_i is determined by [13]:

$$k_i = 1 - 0.8 \cdot k_d \cdot {}^{n_d}/_{n_o} \qquad [2.9]$$

where k_d is selected as an average of 1 for glass and 0.75 for porcelain [13].

The IEC standard uses the U_{90} values, which translates to 10 flashovers and 90 withstands for 100 consecutive pulses. This is not the resulting probability of flashover because only 2% of the applied pulses will reach the voltages assumed in the equations [13].

The statistical withstand voltage, U_{90}, is given by 2.10 (from Equation 2.8):

$$U_{90} = K_t \cdot 1080 \cdot \ln(0.46 \cdot d + 1) \quad [2.10]$$

where:

$$U_2 = \frac{\sqrt{2}}{\sqrt{3}} \cdot U_S \cdot u_2 \quad [2.11]$$

$$U_{90} = K_S \cdot U_2 \quad [2.12]$$

The statistical withstand voltage, U_{90}, is simplified from Equation 2.10 [13]. The U_2 (LG) is the 2% statistical overvoltage which can be determined from the nominal system voltage, U_S (LL), and knowledge of the per unit u_2 values. Typical u_2 values are listed in Table 2.2 [13].

Us (kV)	Closing		Three-Phase Reclosing	
	Without Resistors	With Resistors	Without Resistors	With Resistors
>72.5 to 245	2.3	-	3.0	-
300 to 500	2.3	1.8	2.6	2.1
800	-	1.8	-	2.0

Table 2.2: Table of typical u_2 phase-to-ground values in per unit (after, [13]).

Manipulation of 2.10 results in the minimum electrical distance, D_U (2.13), used in the IEC standards [13].

$$D_U = 2.17\left(e^{U_{90}/(1080K_t)} - 1\right) + F \quad [2.13]$$

The MAIDs are plotted in Figure 2.8, assuming an insulator string with 10 elements for a 132kV OHTL and 20 elements for a 400kV OHTL. The floating object length, F, is the same as the sample UAV (42cm) along the axis of the air gap.

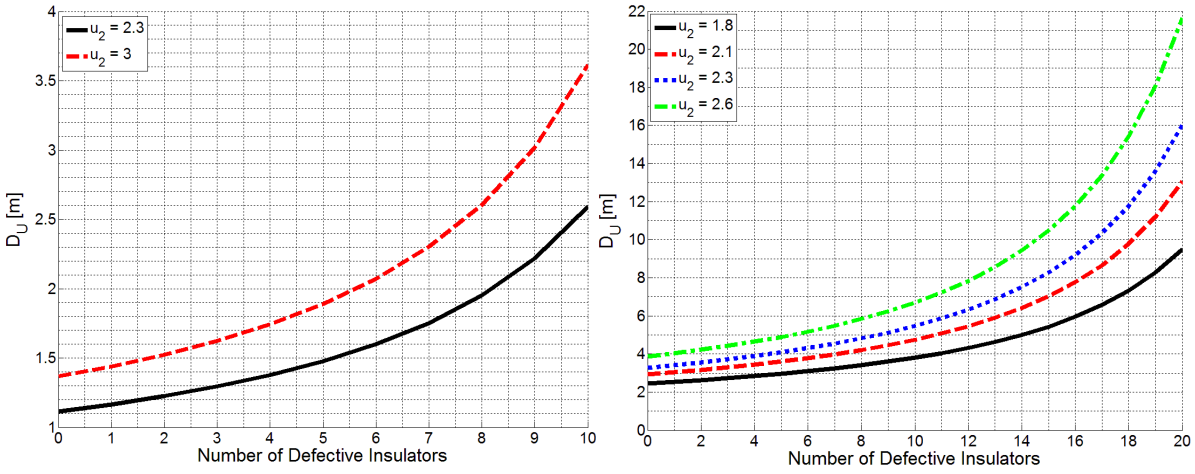

(a) (b)

Figure 2.8: The electrical distance, D_U, for a 132kV OHTL (a) and 400kV OHTL (b) versus number of defective insulators for different possible per unit over-voltages according to Table 2.2.

An ergonomic (safety) distance can be added to D_U (MAID) to give the MADs.

2.2.5 Minimum Helicopter Approach Distances

Analytical equations and tables are set out in the IEEE standard for the MAD, MAID, Minimum Helicopter Approach Distance (MHAD) and Minimum Tool Insulation Distance (MTID) [11].

The MHAD for LG can be calculated using 2.14 [11].

$$D_{FT} = \left(\left((C_1 + a)(V_{LG})(T)(A)\right)\right) + M)(H) \qquad [2.14]$$

where:

- D_{FT} denotes the distance in feet
- V_{LG} is the RMS single phase voltage in kV of the nearby transmission line
- C_1 is the rod gap withstand (100kV$_{RMS}$/ft.) at 60Hz

- a is air saturation factor pertaining to a switching operation
- T is the maximum transient overvoltage (per unit) expected
- A is the adjustment factor for altitude
- M is the movement factor of the helicopter
- H is the helicopter factor.

Tables in [11] give the values obtained by Equation 2.14 which are plotted in Figure 2.9.

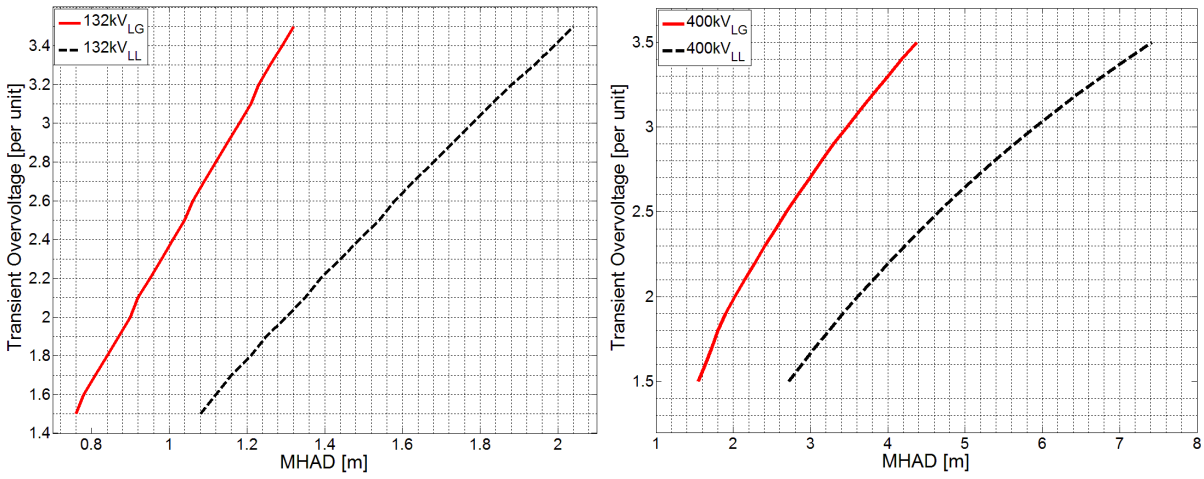

(a) (b)

Figure 2.9: The Minimum Helicopter Approach Distances in the vicinity of OHTLs (after, [11]) for the range of possible TOVs for a 132kV (a) and a 400kV OHTL (b).

The MHAD distances shown in Figure 2.9 are the MAID values with an inadvertent movement factor, M, and a helicopter factor, H.

2.3 Conclusions

This chapter is divided into two sections: a theoretical introduction to the principles affecting HV insulation testing; and a study of international standards describing live-line MAIDs.

The concepts in Section 2.1 are introduced to aid in the development of a strategy for air insulation testing in Chapter 3.

2.3.1 Approaching the HV Testing

AC tests are planned to investigate the risk for a UAV near an HV source. This knowledge will inform the user of the absolute limits to approach distances assuming no TOVs take place.

To ensure minimal risk of flashover to the UAV, the worst-case scenario needs to be considered. This was found in literature to be positive polarity switching impulses. Lightning strikes are neglected as tests will never be performed in these conditions. For breakdown to occur, the switching impulse must contain energy above the static voltage level for a time equal to the TBD.

Although the critical front time of the switching impulse can be used to find the MAID for each gap distance, the 250/2500μs switching impulse specified by the IEC regulations will be used. Testing in this way enables interested parties to easily replicate the tests. It is also not critical to find the exact MAID using the critical front time as appropriate safety factors can be added to ensure a minimal risk of flashover.

The multilevel method was selected as the preferred method of testing. Normal probability paper is used to reduce the number of required samples to predict a probability trend. The CFO (U_{50}) and the standard deviation, σ, can be determined from the probability plots. These two variables are used to describe air's insulation strength.

Realistic clearances and BSLs are listed in accordance with [9]. The clearances can be used to re-create a full-scale model environment for the switching impulse testing.

2.3.2 Comparison of the Standards

The Gallet, CRIEPI and Rizk analytical formulations, as described in section 2.2.1, provide minimum electrical clearances for a rod-plane electrode configuration for positive-polarity switching surges. The analytical formulas are analysed because they are the building blocks of the standard's equations.

The IEEE standard adopts a general approach (the standard applies to all parts of the OHTL) based on existing data to determine the MAIDs for the highest TOV expected on the line. The MAID equation (Equation 2.5) is formulated around empirical data for a rod-rod gap.

The IEEE equations are modified to describe MHADs (Equation 2.14). The modified equation makes use of an industry-accepted factor to account for the electrical size of the helicopter. The unintentional movement due to wind and drift as well the rotor-induced wind factor affecting the ionisation in the gap is also accounted for.

IEEE formulations also exist for LL clearances with a floating object between phase conductors.

The IEC method allows a more practical consideration of the line and its constituent components than the IEEE standard. The IEC approach considers the point where the electric field coupling to a floating object is at its largest (alongside a damaged insulator). Control over problematic variables is exercised by incorporating them into a single correction factor. These variables are: the gap factor; a deviation factor; an atmospheric correction factor; the number of defective insulators; the length of the floating object and a statistical impulse amplitude safety factor. The IEC standard determines the MAID for different line terminations and closing (switching method) schemes.

To determine the MADs, appropriate safety factors need to be incorporated into the formulas depending on the application and confidence in the system.

The IEC standard is overly conservative, but is also the most comprehensive when considering worst-case scenarios.

2.4 References

[1] R. Linga, *EPRI AC Transmission Line Reference Book – 200kV and Above*, 3rd ed., Palo Alto, CA: EPRI, 2005. 1011974.

[2] IEE Power Series, *High Voltage Engineering and Testing*, Peter Peregrinus Ltd., United Kingdom, 1994.

[3] I. Gallimberti, "The Mechanism of the Long Spark Formation," *Journal de Physique,* vol. C7, no. Tome 40, pp. 193-250, 1979.

[4] M. Khalifa et al., *High-Voltage Engineering Theory and Practice*, Marcel Dekker Inc., New York, 1990.

[5] H Kirkham, "Applicability of the Gallet Equation to the Vegetation Clearances of NERC Reliability Standard FAC-003-2", US Department of Energy, April 2012.

[6] *Insulation Co-ordination – Part 2: Application Guide*, IEC 60071-2, 1996.

[7] J.K. Dillard, A.R. Hileman, "UHV Transmission Tower Insulation Tests", *IEEE Trans. Power App. Syst.*, November 1970.

[8] *IEEE Standard for Insulation Coordination - Definitions, Principles, and Rules*, IEEE Std C62.82.1™, 2010.

[9] *Overhead Electrical Lines Exceeding AC 45kV – Part 3: Set of National Normative Aspects*, EN 50341-3-9, 2001.

[10] *Minimum Separation Distance to be Maintained From Energized High Voltage Electrical Equipment and Conductors, Occupational Health and Safety Act*, Guidelines Part 19, June 29, 2005.

[11] *IEEE Guide for Maintenance Methods on Energized Power Lines*, IEEE Std 516™-2009 (Revision of IEEE Std 516-2003).

[12] [Online]. Available: http://www.weibull.com/GPaper/, Last visited September 2013.

[13] *Live Working – Minimum approach distances for a.c. systems in the voltage range 72.5kV to 800kV – A method of calculation*, IEC 61472, 2004.

[14] Gela, G. "Air Gap Sparkover and Gap Factors – Analysis of Published Data." *EPRI TR-104437. Project 3787. Final Report*. December 1994.

Chapter 3

An Empirical Derivation of Minimum Approach Distances

In this chapter, the MADs are determined for a UAV in the vicinity of OHTLs.

Aerial inspection requires that safe-fly zones be specified. If the aerial inspection medium encroaches upon the MADs, it is possible that the vehicle's close proximity to the line will induce flashover between the line and the UAV. Flashover is most likely to occur in the event of a switching surge or lightning strike on the OHTL. Flashover to the UAV will damage the vehicle and its on-board measurement equipment.

This study will focus on 132kV and 400kV OHTLs which account for the majority of transmission lines in a grid. HV tests are done to determine air's insulation strength to compare with international standards and analytical methods.

3.1 The Minimum Air Insulation Distance

The Minimum Air Insulation Distance (MAID) is the electrical breakdown strength of air under Standard Temperature and Pressure (STP) conditions for an electrode configuration. MADs are derived from MAIDs with the addition of an appropriate safety factor.

Various standards exist to ensure safe practice when approaching the lines for live line work [1], [2], [3], [4]. These standards are based on empirical data for a rod-plane gap which results in the weakest dielectric strength of air [1].

The IEEE MAIDs are plotted in Figure 3.1 as a function of the expected TOV on a line [2]. This serves as an example of how the electrical clearances are determined from the standards.

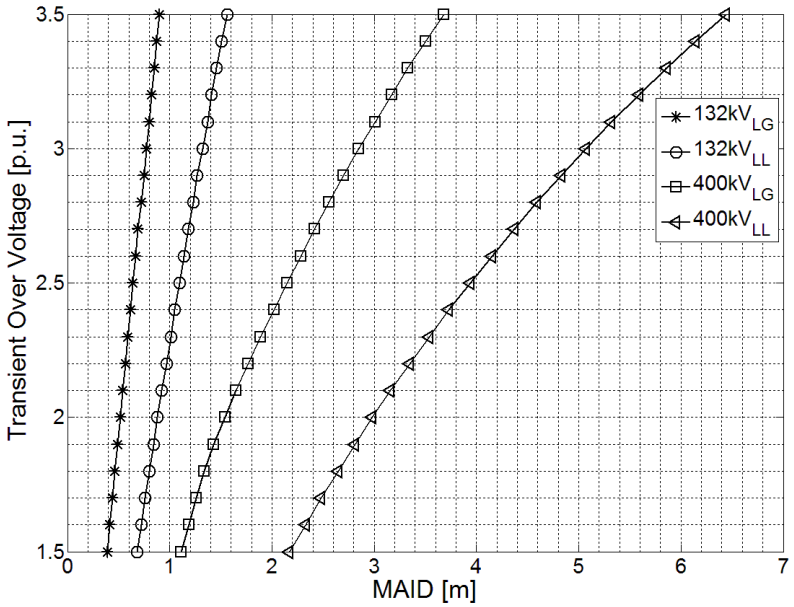

Figure 3.1: The MAIDs for a 132kV and 400kV OHTL as defined by IEEE Standard 516-2009 (after Table D.4, [2]).

The IEEE MAID in the vicinity of the OHTL can be determined from Figure 3.1. The largest possible TOV for a section of line should be known by the power utility from recorded line data. If it is not, a conservative value may be selected to which an appropriate safety factor may be added. In live-line work, the safety factor is selected by the power utility according to worker skill, training, knowledge and the difficulty of the task. Protective barriers can be used to restrict the worker's movement beyond the MAID to reduce the safety factor to zero. This is well documented by the IEC standard 61472 [5].

3.2 Air Insulation – A High Voltage Testing Strategy

The OHTL can be broken up into two separate zones due to the different gap mechanisms. These zones are the LL gap and the LG gap. The LL gap is the air gap between phase conductors. The LG gap may be between a phase conductor and a UAV (Figure 3.2) at a floating potential. The air gap between a phase conductor and the HV tower, and between a phase conductor and shield wire are also LG gaps.

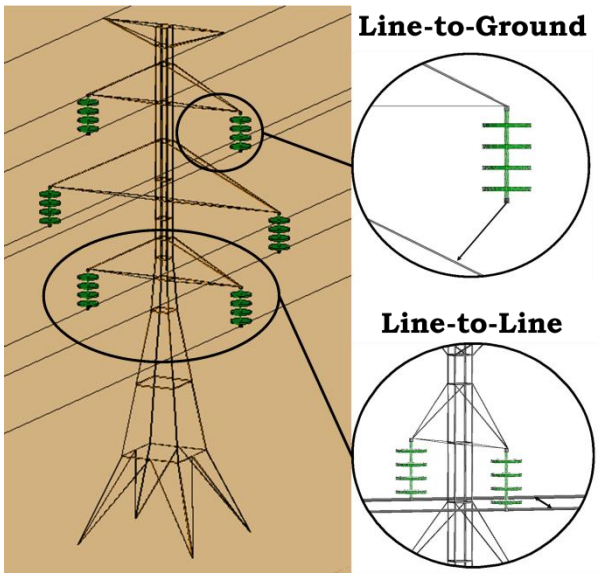

Figure 3.2: Examples of Line-to-Ground and Line-to-Line gaps referred to by the standards for air gaps. The CADFEKO tower representation was reproduced from drawings of a typical 400kV lattice tower (after, [6]).

Figure 3.2 shows an example of typical air gaps used in the empirical models in Section 2.2.

International standards have taken clearance suggestions further to ensure worker safety with the advent of "live-line" work. Although the IEEE and IEC standards make provision for floating objects in air gaps, these are general clearances and not electrode specific (dependent on UAV size and shape).

To analyse air insulation strength, full-scale measurements need to be done alongside phase conductors (Figure 3.3).

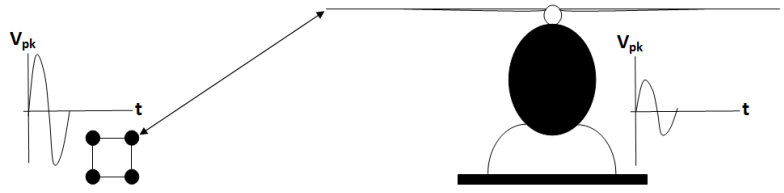

Figure 3.3: AC Coupling between a UAV and bundled phase conductor.

As the conductor potential grows and dies, the induced potential on the UAV follows suit at a lower potential. Because metallic objects rise to the potential of the space they occupy [7], the UAV can get close to the live line for AC conditions without inducing flashover. AC tests are planned to determine the UAVs MAD in the absence of impulses.

If a fault occurs on an OHTL line, the line's HV breakers are triggered. Breaker operation creates large switching impulses which propagate down the line. Clearance suggestions are usually formulated with switching impulses in mind. However, it is common in utilities to disable the automatic reclose when doing live line work. Lightning strikes are disregarded as it is assumed that inspections will not be carried out in adverse weather conditions.

MAIDs are investigated for close-up inspections. The standards cannot be used to determine electrode-specific MAIDs as they are formulated for the worst-case scenario. Gap factors could be determined to achieve this goal [8].

HV experiments are done for a LG air gap with the UAV as an electrode. When the UAV is in an HV tower window, the air gap is subjected to a larger stress. The dual air gap formed results in an increased probability of flashover between electrodes [9]. The same phenomenon occurs when the UAV occupies the gap between phase conductors or between a phase conductor and some grounded obstacle (Figure 3.4).

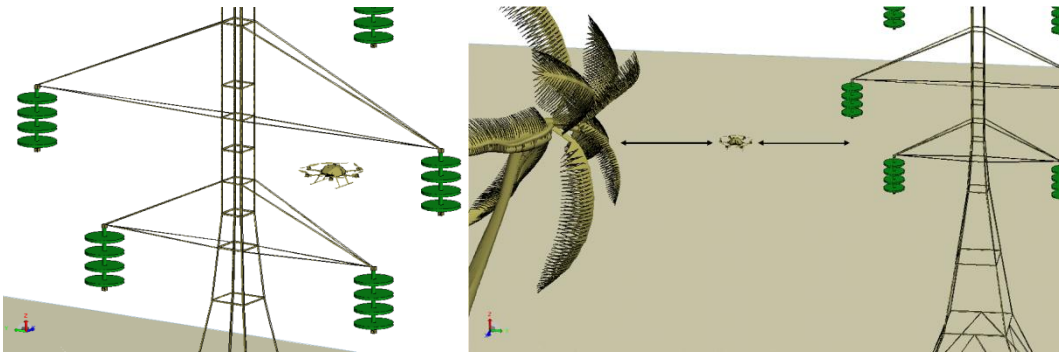

Figure 3.4: Examples of dual air gaps which are created in the vicinity of OHTLs. CADFEKO tower representation was reproduced from drawings of a typical 400kV vertical, lattice tower (after, [6]). The tree model was obtained from [10].

Full-scale testing will proceed with dual air gaps. Defining electrical clearances in terms of dual airs gaps sets an absolute limit on the safe approach distances. Assuming a dual air gap at all times adds a safety barrier for single air gaps.

3.3 The High Voltage Testing Environment

To test the safe-fly zones in the vicinity of OHTLs, a testing environment was set up in the high voltage laboratory at Stellenbosch University. Previous studies [7] have indicated that the high voltage laboratory available is not conducive to testing on such a large scale.

To circumnavigate the identified issues, a more controlled method of experiment was devised. LG tests were conducted in a dual air gap between a phase conductor and a grounded cage. This testing method addresses many practical limitations such as the limited space, budget and resource constraints. Additionally, the tests are not influenced by the external environment.

Standards on insulation co-ordination [2] are used in conjunction with other standards ([1], [3], and [4]) to determine system operating conditions of the HV line network. Table 2.1 (reproduced here as Table 3.1) lists the clearances suggested by [3], as well as the basic insulation levels (BILs) for the OHTL of interest.

Nominal System Voltage [kV]	**Phase to Earth Clearance (m)**	**Phase to Phase Clearance (m)**	**BIL/BSL (kV)**
132	1.1	1.4	550/650
400	2.8	3.6	1425/1050

Table 3.1: Electrical clearances as well as the BILs and BSLs of 132kV and 400kV OHTLs - taken from Table 5.3.5.3 in [3].

A square, metallic cage (Figure 3.5) was constructed by the Stellenbosch University workshop staff with a conductor-tower clearance of 1m for the scale model testing of the 132kV OHTL. This smaller clearance creates a higher internal average

electric field for more stringent test conditions to err on the side of caution, as each tower design differs from the next.

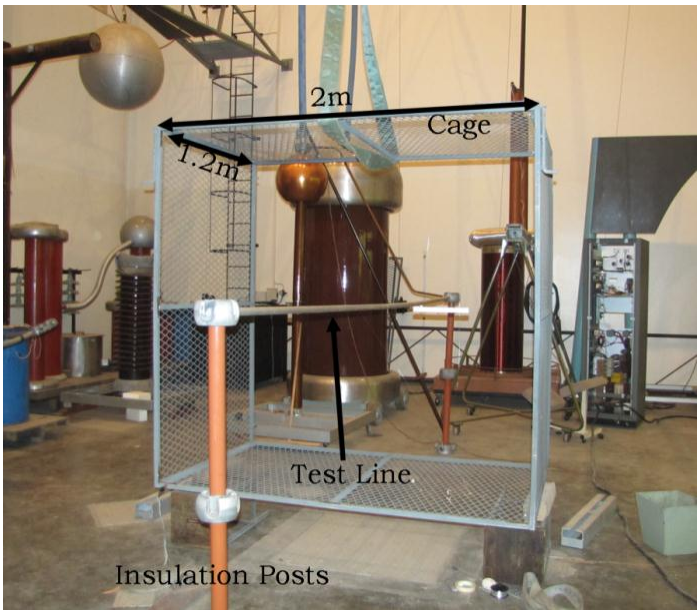

Figure 3.5: The tower window model as used in the setup for the AC and impulse testing in the high voltage laboratory.

A sample UAV (the Astec Firefly) was selected as the test model for the insulation testing. Safe-fly zones are determined for a "hardened UAV", meaning that the UAV is shielded using EMC principles. The shielded vehicle approach is chosen because, as proven later, breakdown will occur at a lower voltage as it is electrically larger – no breaks in galvanic connections.

It is assumed that shielded UAVs will be used to mitigate the risk of energy coupling into the vehicle in these harsh environments. The need for a shielded UAV in these environments is investigated in Chapter 5. Additionally, the simplified model will be faster and easier to implement in the CEM software package.

A solid metal enclosure was assumed for the shell in the UAV's shielded state. Copper brazing rods (3mm) model the wires which leave the shell of the vehicle to control the motors (Figure 3.6).

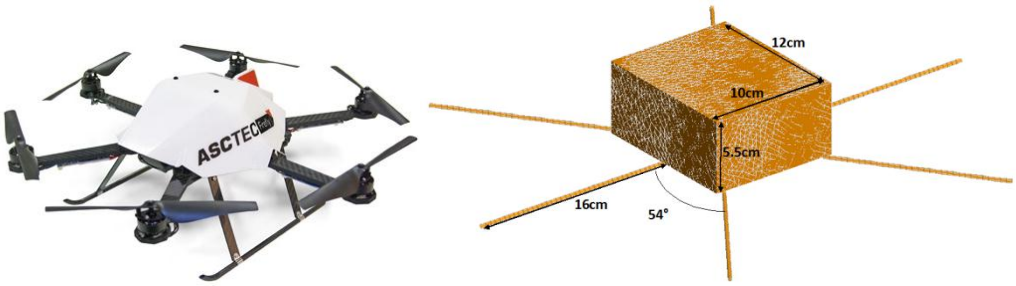

(a) (b)

Figure 3.6: The Astec Firefly, the sample UAV (a), and a CAD drawing of its electrical 1:1 scale model representation (b) used in the insulation tests.

The motors, rotors and skids were neglected as they are assumed to play a small role, as they do not add to the electrical size/shape of the UAV. The addition of these components over-complicates the model for the simulations and was found to play a negligible role in the breakdown voltage.

3.4 Steady State (50Hz) Effect on Insulation Properties

The behaviour of the air gap is first examined under steady-state conditions by supplying the test line (Figure 3.7(c)) via the transformer in Figure 3.7(a). The transformer is a model TEO 300/150 manufactured by Messwandler-Bau GMBH Bamberg [11], [12].

(a) (b) (c)

Figure 3.7: The (a) TEO 300/150 test transformer, the (b) Haefely Trench DMI 551 Digital Measuring Instrument and control panel and (c) the test line and tower window model of a 132kV line used in the measurements.

The Digital Measurement Instrument (DMI), shown in Figure 3.7(b), is used to monitor the test line voltage. The AC transformer feeds the short open-circuit test line through the centre of a grounded cage (Figure 3.8). The UAV model is placed alongside the test line on EM-invisible Styrofoam inside the grounded cage.

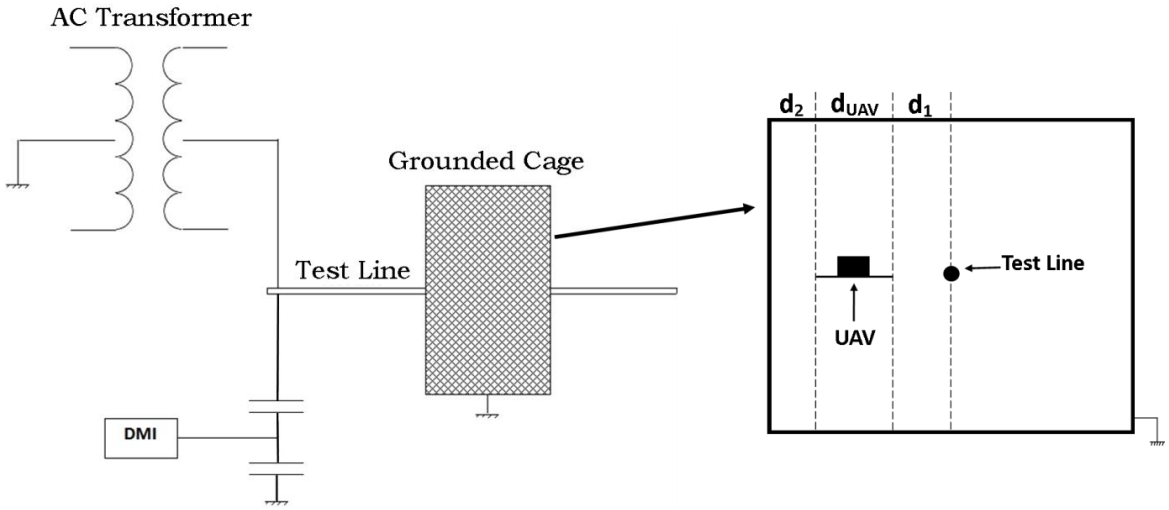

Figure 3.8: The setup for the LG steady-state insulation tests.

A corona camera was connected to a computer with video capturing software (Pinnacle Studio 10) to monitor the air gap. The corocam's sensitivity and gain were set to maximum to detect the instant of corona/streamer inception.

3.4.1 UAV Orientation Effects on Insulation

To define the danger zones of a UAV approaching a live line, the orientation which creates the largest stress between itself and the conductor must be found. Three orientations, at a distance (d), were tested (Figure 3.9).

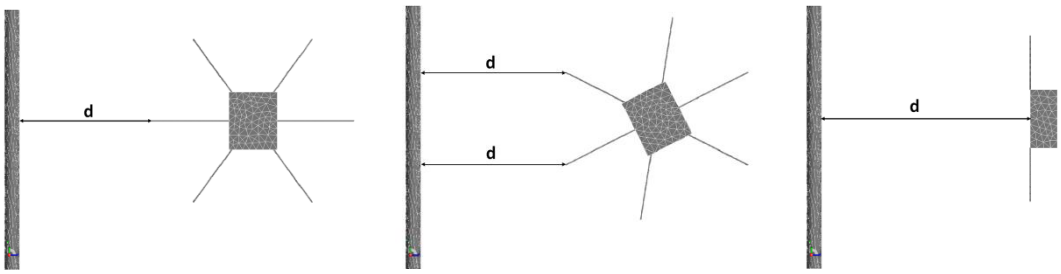

(a) (b) (c)

Figure 3.9: Top views of the different orientations of the UAV alongside a power line at a distance, d, of 4cm.

Corona inception occurs on the tips of the UAV model's rods when the model is raised to a certain potential. This potential can be determined by applying a voltage directly to the UAV and observing when corona inception occurs. Observing the test line voltages which induce corona (for the three orientations) will show which orientation has the strongest coupling. This effect, called field intensification, can be seen by experimenting with different electrode shapes [13].

The test line voltage was increased until the instant of corona inception (Figure 3.10). The UAV model was set the same distance from the test line (4cm) for all orientations.

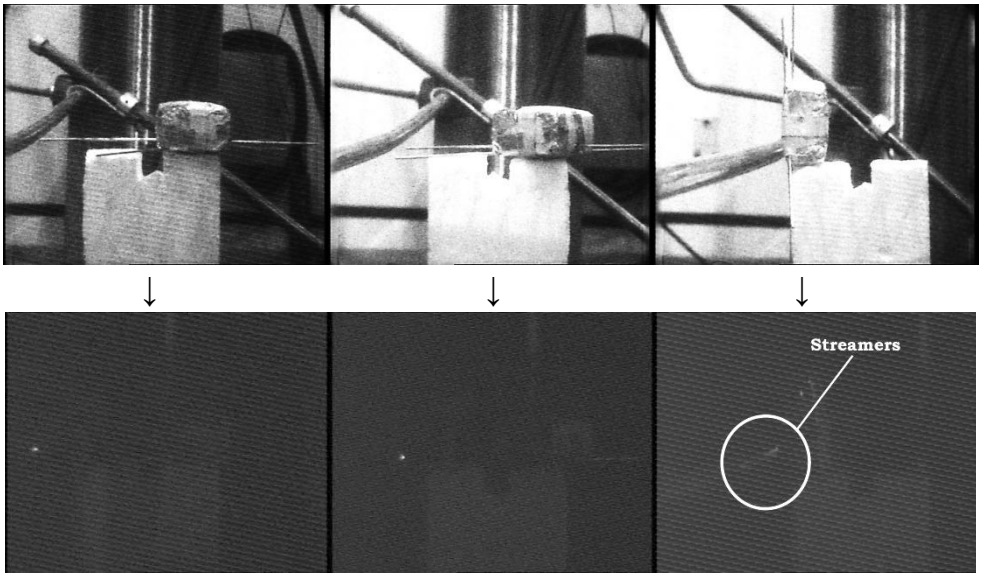

(a) (b) (c)

Figure 3.10: AC tests were done to determine the orientation which would result in the largest stress in the air gap.

Corona inception on the tip of the copper rods is seen in orientation A (Figure 3.9(a)) at 20kV and in orientation B (Figure 3.9(b)) at 25kV. Corona did not occur in orientation C (Figure 3.9(c)) – streamer development began at a much higher voltage of 64kV.

The results of the orientation tests prove that orientation A intensifies the field between the UAV model and the conductor the most. The air gap insulation is therefore weakest for orientation A.

3.4.2 Line-to-Ground Air Insulation Strength – Steady-State Conditions.

Streamers and breakdown events are of primary interest for the AC air insulation tests. Both of these phenomena allow charge equalisation across a gap - meaning there will be current flow between electrodes. Current flow on the UAV is detrimental to the operation of the on-board electronics and motors. The safe-fly zone boundary must therefore be set to just beyond the distance at which there is a possibility of either streamers or breakdown in the gap.

The air gap behaviour under steady state conditions was determined empirically as a function of distance, d, from the conductor surface (Figure 3.11).

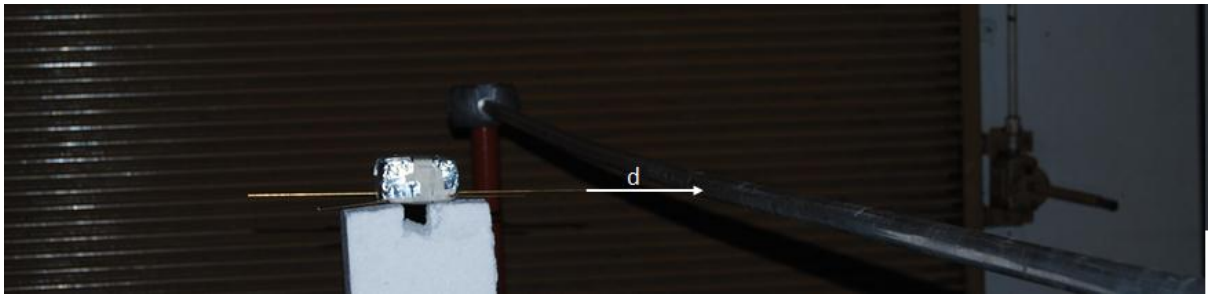

Figure 3.11: The UAV model's position in the cage was varied a distance, d, from the conductor surface.

The test line voltage, at which streamers and breakdown occurred, was recorded (Figure 3.12) along the primary gap as a function of distance, d. The results are normalised to STP. See Appendix A for details.

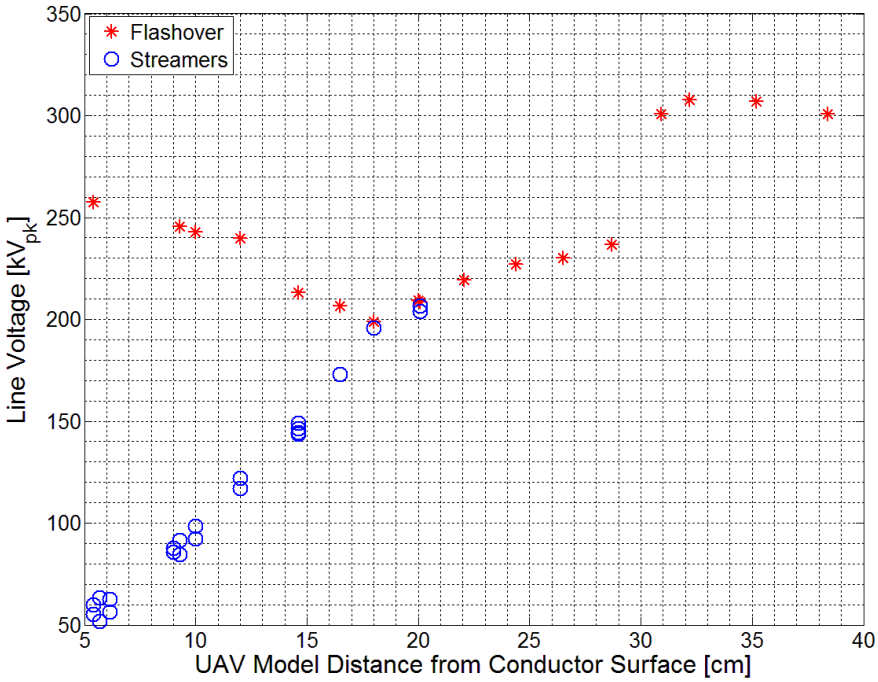

Figure 3.12: AC Results of the Streamer and Breakdown Inception Voltages in the Dual Air Gap.

The results in Figure 3.12 show a variety of mechanisms at play as the UAV moves along the air gap. The results will be analysed in three separate groupings to explain the different mechanisms. The first grouping is selected for d between 5 and 18cm. The second grouping is from 18 to 29cm and the third, for the remainder of the range, from 29 to 40cm.

For the gap spacing 5 to 18cm, streamers bridge the gap between the test line and the UAV model. These streamers form a conductive channel which mimics the addition of a wire in the place of the streamer. This changes the gap from a dual gap to a single gap (between the UAV and the grounded cage). The required line voltage to induce breakdown therefore decreases as d increases because the single air gap is (effectively) decreasing.

When the gap reaches 18cm, streamers no longer occur - or occur only for a very short time. The supply voltage and gap spacing, d, are such that streamers are initiated from the UAV towards the line. Once streamers form in such a small gap initiate, flashover occurs almost instantly. The flashover voltage increases with increasing gap spacing as more energy is required to initiate breakdown in the air gap. All of the streamers result in successful flashovers.

Once the gap spacing increases beyond 30cm, the applied line voltage (required to induce breakdown) creates a large corona spike on the surface of the conductor. The electric field distortion as a result of the corona results in a sudden increase in line voltage required for breakdown. The close proximity of the UAV model to the cage also means that the gap starts behaving more like a single air gap.

The single phase conductor from a 132kV network will reach a LG voltage of $108kV_{pk}$ under steady-state conditions. The results (Figure 3.12) show that for steady-state AC conditions, LG breakdown will never occur. Streamers will, however, begin at a gap spacing of approximately 11cm for such a clearance.

3.4.3 The Importance of Continuous Galvanic Connections

An ungrounded, conductive object in space will always rise to the potential in space which it occupies [7]. Because separated charge acts at a distance, small gaps between conductive objects of different potentials can create large electric fields and discharges between the separated groups of charge.

A solid rod and a split rod, both of the same total length, were placed alongside the test line to examine the effect of an object with an electrical gap in a high voltage environment (Figure 3.13).

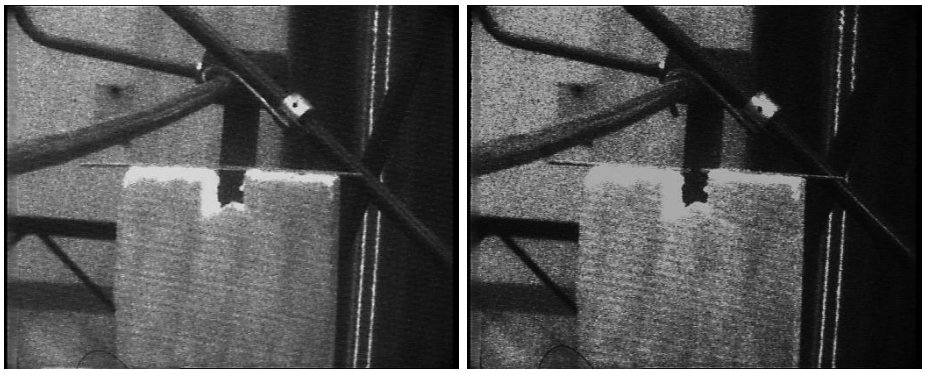

(a) (b)

Figure 3.13: The solid rod (a) and the split rod (b) used to examine the importance of complete galvanic connections in a high voltage environment. A block of EM-transparent polystyrene foam supports the respective rods.

The test line voltage was increased until corona inception occurred on both rods (Figure 3.14). Both rods are placed a distance of 6.5cm away from (and perpendicularly to) the conductor's surface.

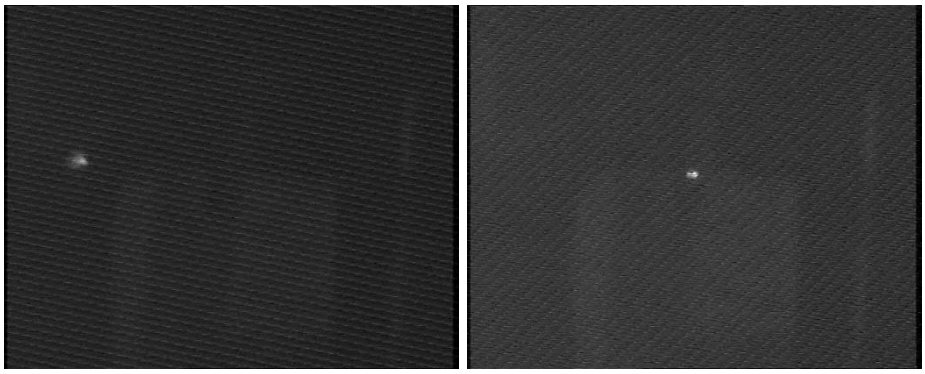

(a) (b)

Figure 3.14: Corona inception with (a) a solid rod when V_L = 50kV and with (b) a split rod when V_L is at 70kV.

The split rod (Figure 3.14(b)) drives a corona source only when subjected to a larger electric field. Individually, the split rods are electrically smaller and therefore cross a smaller range of equipotential lines. According to [7], this means that the split rods equalise to a lower potential. A larger test line voltage is therefore required to initiate corona inception on the outer ends of the split rods. Corona inception

occurs in the gap first due to its larger localised electric field. Discontinuous connections in the UAV design will create strong internal fields which are detrimental to the operation of the UAV and any on-board measurement equipment.

3.5 Line-to-Ground Air Insulation Strength – Switching Impulses.

To properly define the MAD, the air gap behaviour needs to be examined with switching surges, since there is always a risk that the line will be subjected to transients. Lightning strikes are not considered as it is assumed that UAVs will never be operated when there is a risk of lightning nearby.

A Marx bank generator was used to generate high voltage impulses which were then manipulated by a wave shaping network to adhere to standard rise and fall times.

3.5.1 Adherence to IEC Standards

One of the main factors affecting the breakdown strength of air is the rise and fall time of the impulse. The IEC standard specifies impulse rise and fall times – given in Figure 3.15 [14] and Table 3.2 [1].

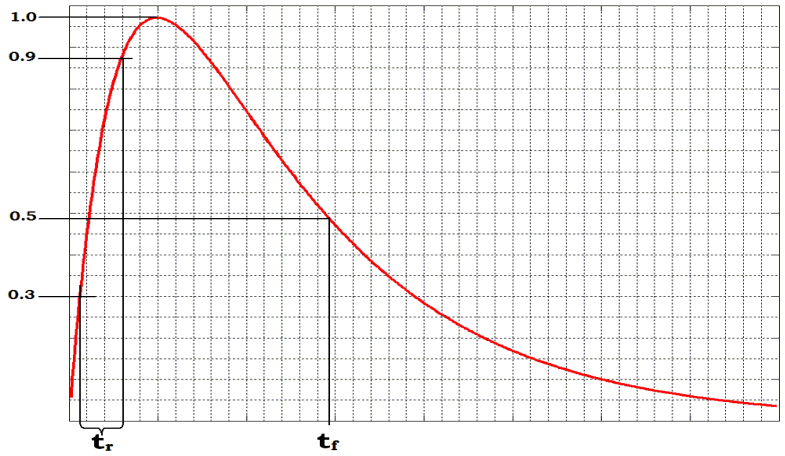

Figure 3.15: The standard impulse wave shape defined by the IEC standards (after, [14]).

The rise and fall times for impulse over voltages are defined in Table 3.2:

IEC Standard - Insulation Coordination 60071-2		
	Rise-Time (t_r)/ Fall Time (t_f) [µs]	**t_r Tolerance/tf Tolerance [%]**
Switching Impulse	250/2500	±20/±60
Lightning Impulse	1.2/50	±30/±20

Table 3.2: Standard rise and fall times, specified by the IEC, for switching and lightning impulses [1].

To comply with the required rise and fall times set out by the IEC, an external wave shaping circuit is required. The raw output pulse from the Marx bank generator was manipulated by the time constants of the external circuit.

3.5.2 Switching Impulse Test Setup

The Marx bank generator (Phillips Model PW 5922) in the high voltage laboratory at Stellenbosch University is used (Figure 3.16) to generate high voltage switching impulses.

Figure 3.16: The Marx bank generator in the high voltage laboratory at Stellenbosch University.

The impulse generator consists of a reconfigurable chain of resistors and capacitors. The capacitors are charged by a DC supply, and then discharged through a network of spark gaps as seen in Figure 3.17.

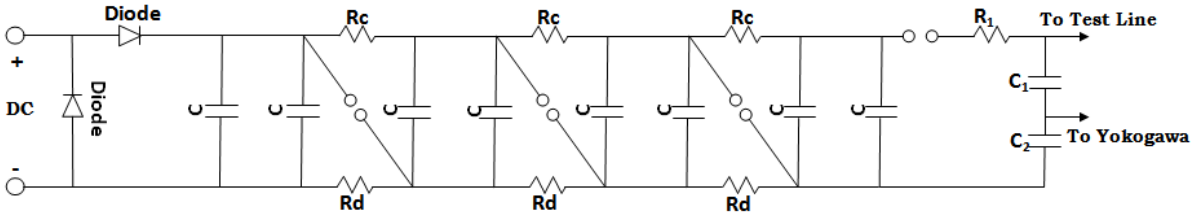

Figure 3.17: The schematic diagram of the Marx bank generator (4 stage configuration) and external wave shaping network.

The component values of the Marx bank configuration and shaping network (Figure 3.17) used to generate a 250/2500μs impulse are listed in Table 3.3.

Marx Bank Generator Component Values					
C	**R_C**	**R_d**	**R_1**	**C_1**	**C_2**
0.125µF	10kΩ	10kΩ	Variable Unknown	2.5nF	25µF

Table 3.3: The component values of the Marx bank generator and pulse shaping network seen in Figure 3.17.

Three configurations are possible (2 stage, 4 stage and an 8 stage). The number of stages refers to the number of capacitor groupings. The configuration of the machine dictates the effective circuit capacitance which influences the rise and fall times of the output pulse. The effective charging network of the 4 stage configuration is shown in Figure 3.18.

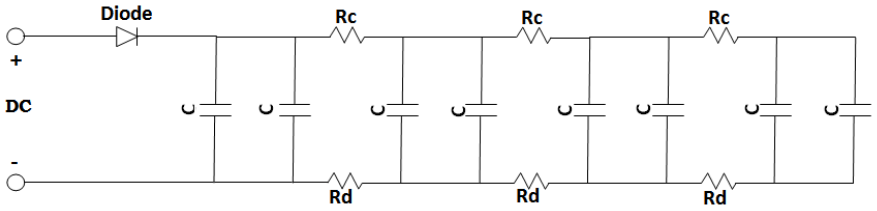

Figure 3.18: The effective charging circuit for the Mark bank generator in a four stage configuration.

Once the spark gaps fire, the energy stored in the high voltage capacitors is discharged in series (Figure 3.19) through the external wave-shaping network to the test line.

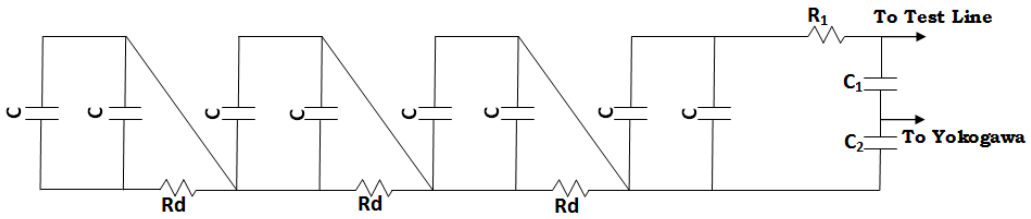

Figure 3.19: The discharging circuit of the Mark bank generator in a four stage configuration.

The output voltage is determined by multiplying the DC charging voltage ($175kV_{MAX}$) by the number of stages. The four stage circuit configuration gives a maximum output voltage of $700kV_{pk}$, but limitations are imposed by electrical clearances, component capacities and the overall efficiency of the system.

A higher output voltage is possible using an 8 stage configuration, but the reduction in capacitance would reduce the rise time appreciably.

A water resistor (approximately 9 litres) was used as the external wave shaping variable resistor (Figure 3.20), R_1.

Figure 3.20: The water resistor, R_1, suspended in the HV lab.

The water resistor was filled with tap water and the impulse parameters checked. To achieve the correct rise and fall times, sodium chloride solution was used in small quantities to increase the conductivity and decrease the resistance. The resistance was adjusted until acceptable rise and fall time were achieved.

A capacitive divider was used to measure the output pulse. The extra capacitance in the circuit controls the fall time and efficiency of the output pulse. The high voltage capacitor (Figure 3.21(a)) used in the place of C_1 has a capacitance of 2.5nF. C_2 was manufactured with a capacitance of 25µF (Figure 3.21(b)).

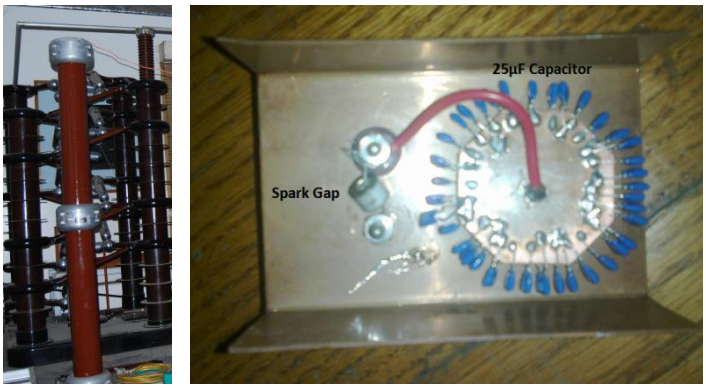

(a) (b)

Figure 3.21: Capacitive Divider C_1 (a) and C_2 (b) used to measure to pulse applied to the test line.

The capacitive divider, C_1 and C_2, reduce the peak output of the pulse by a factor of 10,000. The capacitive division ratio was increased to 100,000 using a 10 times probe.

Calibration of the capacitive divider was done against a Kilovolt meter from Haefely and the AC resistive divider used in the AC tests. The calibration is described further in Appendix A.

The switching impulse applied to the test line was measured (Figure 3.22) on the Yokogawa DLM 2032.

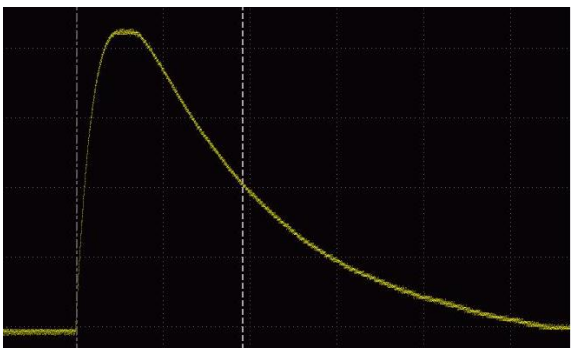

Figure 3.22: The output switching impulse measured on the Yokogawa Oscilloscope.

A set of 10 shots were fired to test repeatability (Table 3.4). This test ensures that the rise and fall times are relatively consistent and not affected by any components

heating up. Shots were spaced approximately 15 seconds apart, as will be the case when testing, to negate residual space charge effects.

The Rise-Times Recorded for 10 Consecutive Shots

Shot no.	1	2	3	4	5	6	7	8	9	10
Rise-Time [µs]	280	275.2	266.4	276	276	273.6	262.4	268	272.8	274.4

Table 3.4: The rise-times recorded for 10 consecutive shots on the Marx bank generator to determine repeatability and adherence to the tolerances.

The measured pulse meets the specifications set out in the standards. The rise-time is relatively consistent. The fall time, although not documented due to its large tolerance, is well within the acceptable range at approximately 2ms.

3.5.3 Switching Impulse Test Results

The switching impulse tests are carried out in the same environment as the AC tests. The setup is shown in Figure 3.23.

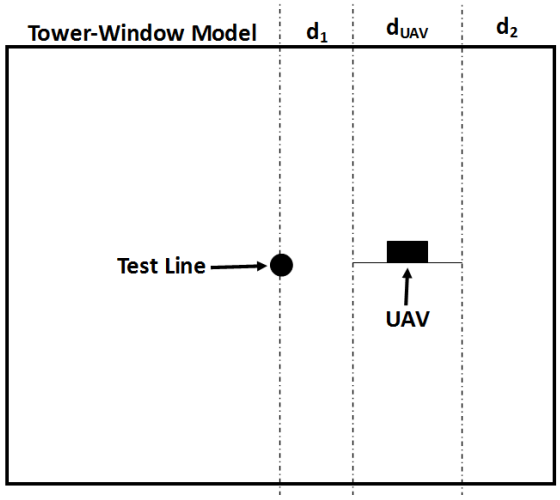

Figure 3.23: Setup for the switching impulse testing in the tower window model.

Gap d_1 and d_2 are referred to as the primary gap and secondary gap respectively.

To determine the probability of breakdown, the multilevel method (fully described in Section 2.1.4) is used. In this method, multiple shots are applied at the same peak voltage. The voltage and rise-time are checked for each withstand, whilst each breakdown event (Figure 3.24) is noted. The probability of breakdown is then the number of successful breakdown events divided by the total number of shots (Equation 2.1). At least two probabilities between 10% and 90% are required to predict a trend.

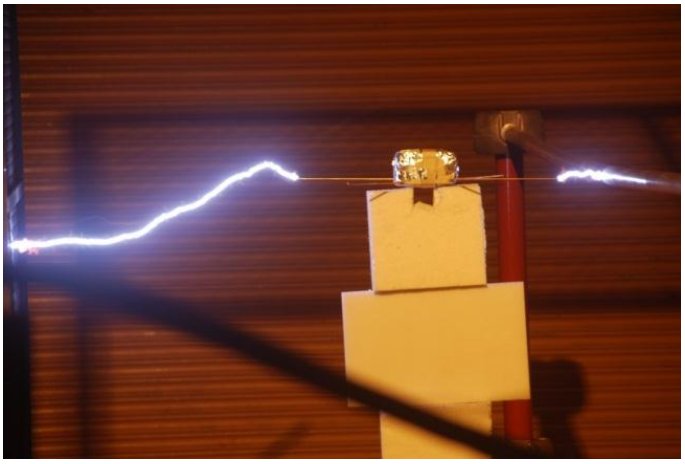

Figure 3.24: A breakdown event for a LG, dual air gap. Breakdown occurs in both air gaps.

A minimum of three probability points were plotted for each sampled primary gap to determine the 50% probability of breakdown (U_{50}).

Because the breakdown of air gaps follows a Normal distribution, probability paper can be used to simplify the testing procedure. This is discussed in more detail in Appendix A.

The U_{50} values, (normalised to STP) determined for the primary gap, d_1, are plotted in Figure 3.25. The gathered data, its processing and normalisation are documented in Appendix A.

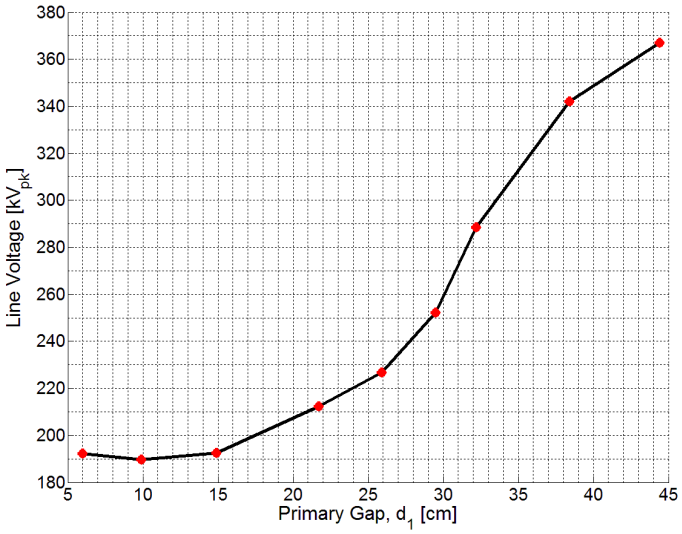

Figure 3.25: The normalised U_{50} values recorded for the impulse tests as a function of the primary gap.

Data was gathered within the bounds of the safe system voltage (approximately 600kV$_{pk}$) and clearance levels in the setup. The curve may be extrapolated to obtain data for remainder of the primary gap.

The probability plots in Appendix A can be used to determine the standard deviation, σ. The standard deviation is plotted for each primary gap, d_1 (Figure 3.26).

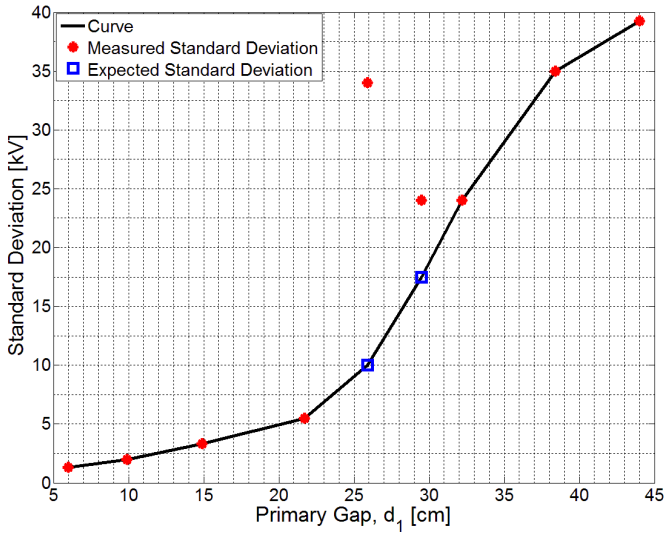

Figure 3.26: The standard deviation in the tower window model as a function of the primary gap, d_1.

Two standard deviation samples do not follow the trend in Figure 3.26. A 1kV change in the charging voltage can result in a transition from 0% to certain flashover for these small air gaps. This makes it challenging to get more than two probabilities points to improve the accuracy of the plots. It is known that the U_{50} values are accurate as probabilities near 50% were recorded for a minimum of 15 applied impulses for both primary gaps. The two inaccurate points were corrected by fitting them to the trend (Figure 3.26).

To determine the safe-fly zones, withstand voltages (U_{WS}) must be examined. The withstand voltage, U_{WS}, represents a 0.13% probability of flashover [15]. The U_{SFO} is defined as the point at which flashover is almost guaranteed (99.87% probability) [15]:

$$U_{WS} = U_{50} - 3\sigma \quad [3.1]$$

$$U_{SFO} = U_{50} + 3\sigma \quad [3.2]$$

Figure 3.25 is adapted to include the U_{WS} and U_{SFO} in Figure 3.27.

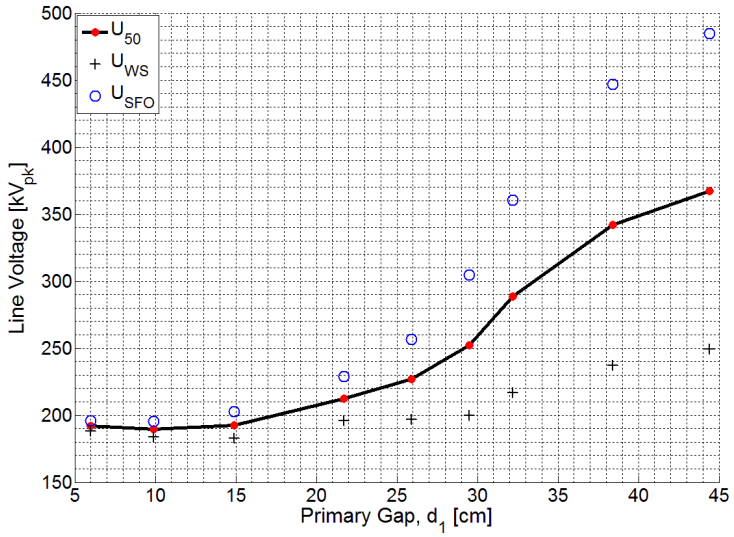

Figure 3.27: The corrected plot of the probability of flashover, withstand voltage and positive critical flashover voltage - plotted as a function primary gap, d_1.

For the dual air-gap (in this case the tower window) it can be seen (Figure 3.27) that a switching impulse (BSL of 650kV$_{pk}$) is likely to cause breakdown regardless of where the UAV is.

The plot of U_{WS} (Figure 3.27) versus distance can be used to determine the safe-fly zones alongside a phase conductor.

Because the system limits were reached in the testing, extrapolation was implemented to obtain the full range of data points in the testing environment. A MATLAB extrapolation function, interp1, was used to extend the data set (Figure 3.28).

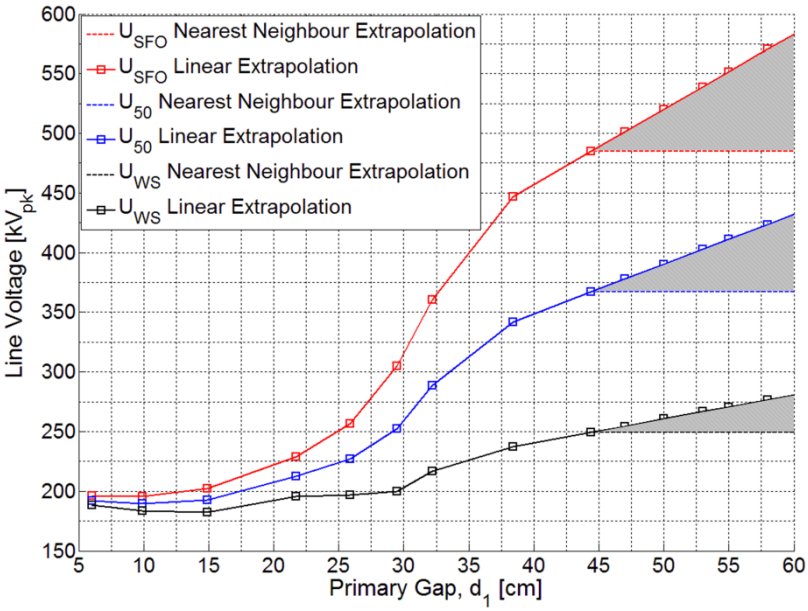

Figure 3.28: Extrapolated curves for the measured data using MATLAB's interp1 function.

The extrapolated data set was found using two methods: the nearest neighbour method and linear extrapolation. The region between the two methods of extrapolation is shaded. This is where the actual curve is expected to lie. Following the worst-case scenario methodology, the upper portion of the curve is used in the analysis.

Even with the maximum primary gap in the cage, it can be seen that the 650kV BSL of a 132kV line is not yet reached. A 650kV impulse on the line will always

induce flashover in this scenario. This indicates that at no point is it safe for the UAV to occupy the region within a tower window.

3.6 Summary and Conclusions

The AC tests showed that the UAV is not at risk of inducing breakdown at any point in the 132kV tower window. Streamers will, however, bridge the air gap within approximately 11cm from the 132kV conductor. Although corona inception is a possibility, this is not detrimental to the operation of the UAV.

The MAD must be formulated around the worst-case scenario. This is the positive polarity switching impulse. These tests could only be run for a 132kV tower window model due to equipment limitations. Tests alongside phase conductors and for a 400kV tower window (an equivalent model) require a Marx bank generator capable of delivering a higher output voltage.

The switching impulse tests were done in accordance with the IEC standards as a function of distance in the primary gap (between the conductor and the UAV). A statistical analysis of the results produced a curve of air's dielectric strength. The results were normalised to STP in Appendix A.

The results of the impulse testing showed breakdown between the line and the UAV will occur regardless of the UAVs position in the tower window. This is assuming (worst-case scenario) that an impulse at that point is equivalent to the 132kV OHTLs BSL ($650kV_{pk}$).

The switching impulse curve obtained through the HV testing is compared to an analytical prediction in Chapter 4. The equations are then used to predict the safe-fly zones for the UAV alongside power lines.

3.7 References

[1] *Insulation Co-ordination – Part 2: Application Guide*, IEC 60071-2, 1996.

[2] *IEEE Guide for Maintenance Methods on Energized Power Lines*, IEEE Standard 516, 2009.

[3] *Overhead Electrical Lines Exceeding AC 45kV – Part 3: Set of National Normative Aspects*, EN 50341-3-9, 2001.

[4] *Minimum Separation Distance to be Maintained From Energized High Voltage Electrical Equipment and Conductors, Occupational Health and Safety Act*, Guidelines Part 19, June 29, 2005.

[5] *Live Working – Minimum approach distances for a.c. systems in the voltage range 72.5kV to 800kV – A method of calculation*, IEC 61472, 2004.

[6] James Beswick, National Grid, UK Transmission (James.Beswick@nationalgrid.com), "Re: HV Tower Clearances", E-mail to M. Groch (15478602@sun.ac.za), 27/09/2012.

[7] Matthew Groch, "The Effect of Small Airborne Systems near High Voltage Lines", University of Stelenbosch, Final Year B.Eng Project, Tech. Rep., 2011.

[8] Linga R., *EPRI AC Transmission Line Reference Book – 200kV and Above*, 3rd ed., Palo Alto, CA: EPRI, 2005. 1011974.

[9] H Kirkham, "Applicability of the Gallet Equation to the Vegetation Clearances of NERC Reliability Standard FAC-003-2", US Department of Energy, April 2012.

[10] [Online]. Available: GRABCAD, http://grabcad.com/library/palm-tree--2, Last visited September 2013.

[11] Michael John Hendricks, "Acceptance Testing and Commissioning of High Voltage Test Transformer", Final Year Thesis, November 1979.

[12] *Test Transformers*, Messwandler-Bau GMBH Bamberg, Operators Manual

[13] CIGRE, 'Guidelines for the Evaluation of the Dielectric Strength of External Insulation', *Technical Brochure* no. 72, 1992.

[14] *Electromagnetic Compatibility (EMC) – Part 4-5: Testing and Measurement Techniques – Surge Immunity Test*, IEC 61000-4-5, Second Edition, 2005.

[15] J. Afa, "Statistical Evaluation of Critical Flashover and Withstand Voltage for Small Airgap," *International Journal of Emerging Technology and Advanced Engineering,* vol. 3, no. 1, pp. 36-40, 2013

Chapter 4

Simulations and Analytical Predictions of Air's Insulation Strength

In this chapter, simulations and analytical predictions are used to describe safe-fly zones for a UAV model in the proximity of OHTLs. No models exist which encompass all of the variables involved in the breakdown phenomenon. For safety reasons, a worst-case scenario approach is usually adopted.

To predict air's critical dielectric breakdown values, Rizk's analytical equations [1] [2] are used in conjunction with FEKO v6.2 [3]. A FEKO model will be calibrated to a linear instance of the measurement environment discussed in Chapter 3. FEKO simulations are used to determine a geometric factor needed as an input into the analytical equations.

4.1 FEKO – The Electromagnetic Solver Package

FEKO is a CEM software simulation package. It is based on the MOM formulation, but uses hybridisation techniques to incorporate other solvers depending on the application (Figure 4.1).

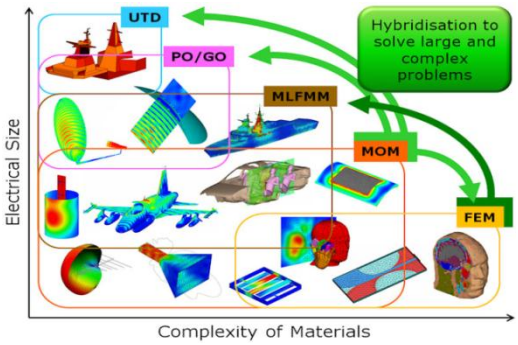

Figure 4.1: The different solvers in FEKO can be used to solve a multitude of complex problems [3].

FEKO is the ideal tool to use in the simulation of a complex structure alongside large-scale OHTLs. The Finite Element (FEM) formulation can be used in conjunction with the MOM formulation to consider a complex dielectric, or an arbitrarily shaped object in the vicinity of the line. In order to make the problem more feasible to handle in simulation software in terms of run time, model simplification is required.

4.2 Calibrating FEKO to the Measurement Environment

To calibrate the FEKO model with the measurement environment, a simple experiment was devised (Figure 4.2).

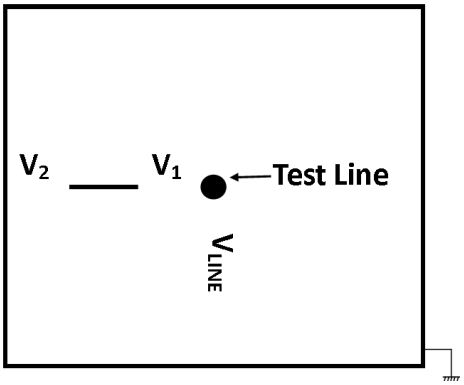

Figure 4.2: The simple linear experiment is used in to ensure correct modelling of the measurement environment. Equating the capacitive division network (V_1 and V_{LINE}) in simulation and measurement will derive confidence in both.

The capacitive division in the measurement setup is checked experimentally for a conductor-rod-plane gap for verification in FEKO. If correlation is proven, it can be concluded that the modelling and setup are verified. The experimental setup is shown in Figure 4.3.

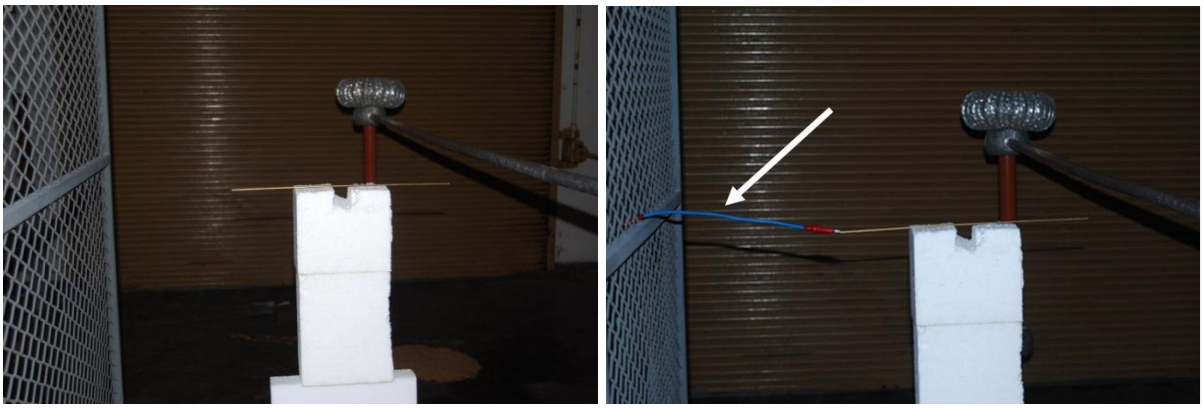

(a) (b)

Figure 4.3: The two test conditions. In the first test (a), the rod is not grounded. In the second test (b) the rod is connected to the grounded cage with the rod at the same distance, d_1.

In the first test (Figure 4.3(a)), the line voltage is increased until streamers bridge the gap between the rod and the test line (primary gap, d_1), at which point the line voltage is noted (V_{LINE} in Table 4.1). In the second test (Figure 4.3(b)), the rod is connected to ground and the same test is performed.

The second test effectively determines the voltage, V_1 required on the test line for streamers to span the primary gap, d_1 (17.8cm). The voltage, V_1, required to initiate streamers in the primary gap, d_1, remains constant whether the rod is floating or grounded.

Table 1 lists the line voltage versus the streamer bridging for V_1 which was derived from a combination of both tests. The measurements were done multiple times to check repeatability (Table 4.1).

V_{LINE} [kV_{pk}]	**210**	**210**	**210**	**210**
V_1 [kV_{pk}]	165	161	163	164

Table 4.1: Measurement results from the two test conditions shown in Figure 4.3.

The measurement environment was modelled in FEKO (Figure 4.4). The Styrofoam supports are an EM invisible medium and is neglected in the model.

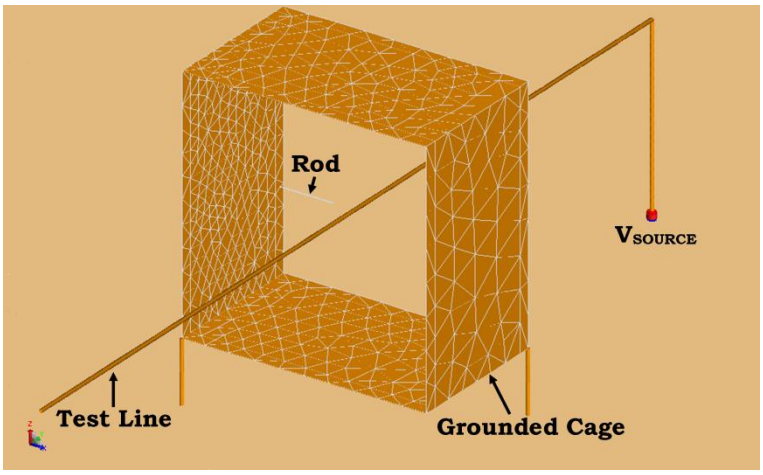

Figure 4.4: The CADFEKO model of the experimental setup used to model the linear calibration testing.

A simulation model was designed in CADFEKO to the same scale as the physical setup. An open-circuit line was fed via a voltage source at 210kV (50Hz AC).

Near field requests were used in FEKO to determine the gap voltage, V_1, given V_{LINE}. Near field requests sample electric and magnetic field values at points in space defined by the user. The potential in space is determined from electric field values, E, in a closed loop using [4]:

$$V_{ab} = -\int_{V_b}^{V_a} \overline{E} \cdot \overline{d\ell} \qquad [4.1]$$

The electric field values, spanning primary gap, returned by FEKO were converted to a potential across the gap using Equation 4.1. The measured and simulated results are compared in Table 4.2.

	Measured				**Simulated**
V_{LINE} [kV_{pk}]	210	210	210	210	210
V_1 [kV_{pk}]	165	161	163	164	162.9

Table 4.2: The comparison of the measured and simulated primary gap voltage, d_1, used for calibration.

FEKO predicts that for the test line voltage of 210kV, the primary gap voltage, V_1, is approximately 162.9kV. The simulation model has been verified against the measured results. FEKO can now be used to determine the geometric factor for comparison to Chapter 3's measured breakdown values.

4.3 Switching Impulse Breakdown for Small Air Gaps

Analytical equations are used to verify the measurement of breakdown voltages for a conductor-tower clearance with a floating object in the gap (Figure 4.5). The floating object (electrode) is the UAV model used in Chapter 3.

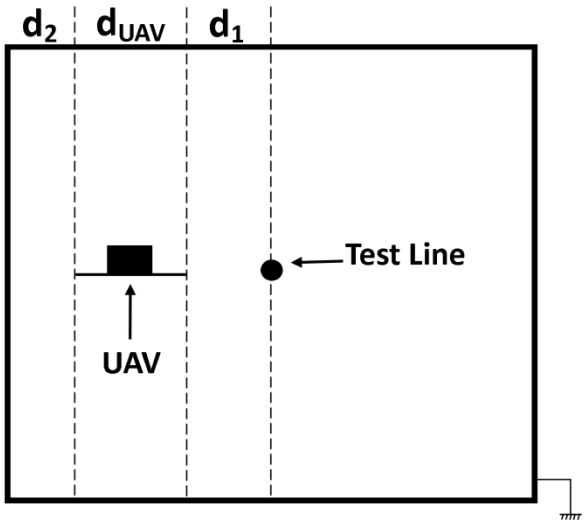

Figure 4.5: The UAV divides the gap into a primary gap, d_1, and secondary gap, d_2. Analytical equations are used to describe breakdown in this environment.

The impulse tests in Chapter 3 are done for a positive switching impulse according to IEC Standards (250/2500μs) [5]. The analytical equations determine the minimum CFO, assuming a positive switching impulse with a critical front time across the entire primary gap. The analytical procedure is set out below and is adapted from work done by F. Rizk ([1] and [2]).

Both streamer and leader breakdown were considered. The leader breakdown mechanism will be disregarded for now, as streamer breakdown was found to be

dominant for both gaps. The streamer breakdown voltage, U_{S1}, is determined for the primary gap, d_1, using Equation 4.2 [1].

$$U_{s_1} = (E_{s1} \cdot d_1)/(1 - k_0) \quad [4.2]$$

The streamer breakdown voltage (Equation 4.2) makes use of a critical electric field gradient. The suggested value for a conductor-rod gap is 500kV/m, and 400kV/m for a rod-plane gap [1]. The variable k_0 [2] is a geometric factor which can be determined through a charge simulation technique (the calibrated FEKO model is used). The variable k_0 is used to relate the floating object's potential to the test line potential as a function of distance (Figure 4.6).

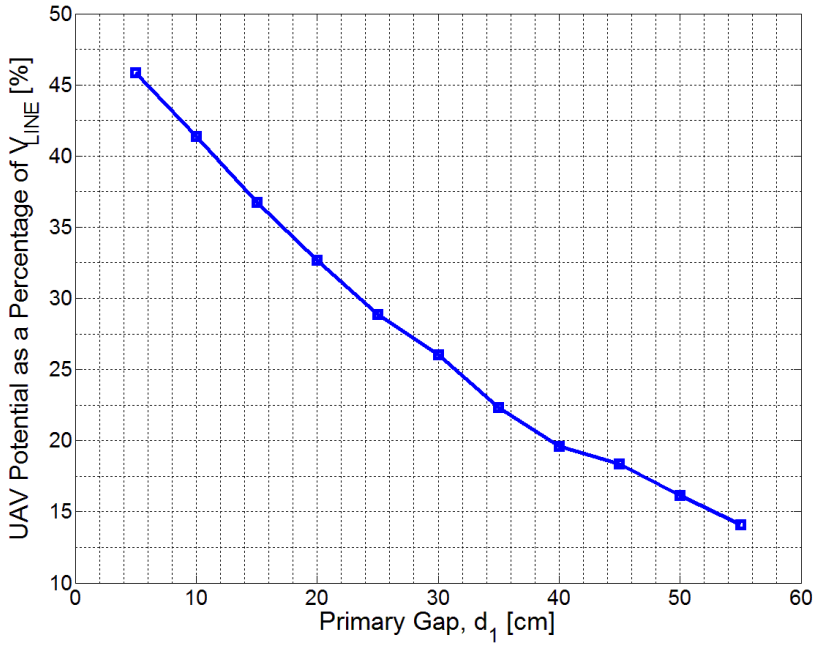

Figure 4.6: The coupling factor, k_0, of the UAV relative to the excited test line. This is derived in FEKO from the setup in Figure 4.5

The secondary gap (d_2) breakdown occurs according to Equation 4.3 [1].

$$U_{s_2} = (E_{s2} \cdot d_2)/(1 - k_0) \quad [4.3]$$

The minimum required breakdown voltage, U_b, is selected as the dominant gap (the one in which streamer breakdown occurs first). The CFO voltage is determined from:

$$CFO = U_b/(1 - 3\sigma) \qquad [4.4]$$

The standard deviation varies for different gap configurations. Rizk suggests that σ be taken between 3% and 5% for a positive switching impulse [1]. To get a more accurate representation of the measurements, the measured standard deviation (Appendix A) in Figure 4.7 was compared to the Rizk's suggested value.

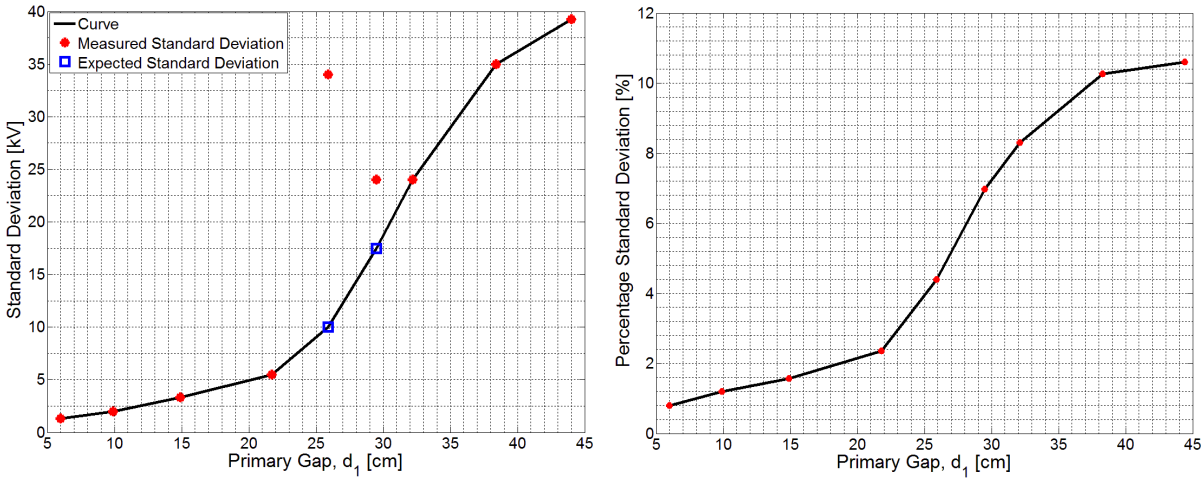

(a) (b)

Figure 4.7: The measured standard deviation for the air insulation breakdown tests in Chapter 3.

The measured and the suggested (5%) standard deviations are used in the analytical comparison to the measured switching impulse CFO voltages (Figure 4.8) from Chapter 3.

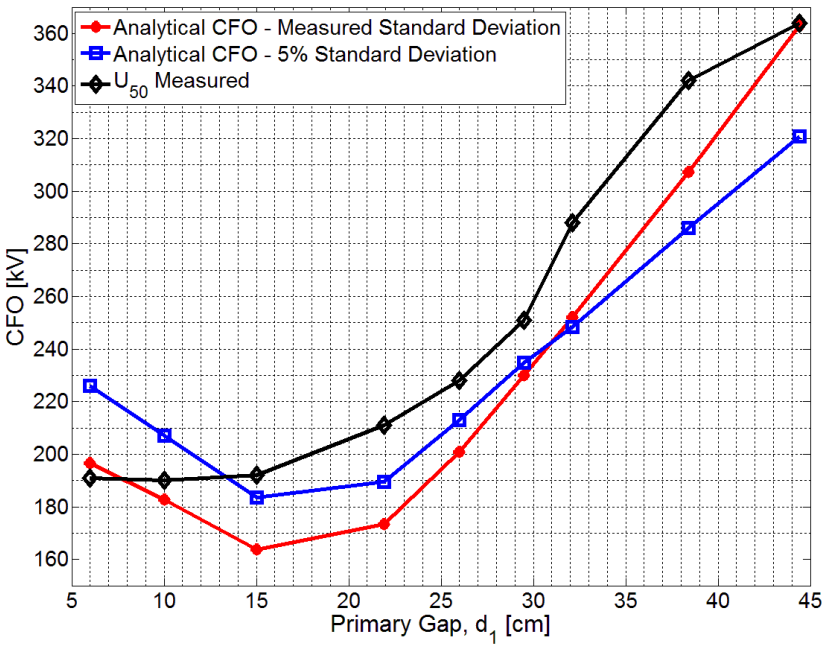

Figure 4.8: A comparison of the analytical predictions of the CFO and the measured CFO.

A good match is achieved between the measured and simulated predictions. The incorporation of the measured standard deviation does not influence the result substantially. Figure 4.7(b) shows that the measured standard deviation is close to the suggested 5% [1].

Apart from the inaccuracies inherent in Rizk's model (due to the complexity of the problem), a portion of the discrepancy is because of the different impulse rise times used in the simulation and model. This effect is described in Chapter 2. The switching impulse rise time used in the measurements adheres to the IEC wave-shape specifications [5]. A 250/2500μs impulse is used regardless of applied voltage, electrode configuration or gap spacing. The simulation assumes a critical front time which changes with gap spacing.

Another possible reason for the discrepancy stems from the critical electric field gradient used in the analytical expressions. The suggested field gradients are applicable to conductor-rod and rod-plane gaps for the primary and secondary gaps respectively. A rod approximation for the UAV model may not be entirely accurate.

Optimisation of the suggested electric field gradients gives the curve in Figure 4.9, where E_{S1} = 550kV/m and E_{S2} = 430kV/m. The original electric field gradients were 500kV/m and 400kV/m respectively.

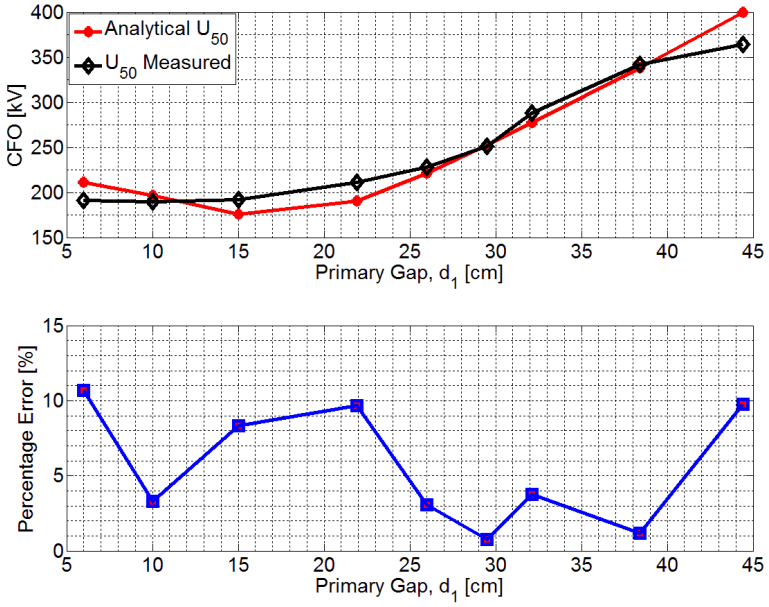

Figure 4.9: The measured and analytical (optimised critical field gradient) CFO predictions as a function of the primary gap, d_1.

A better fit is achieved for the analytical curve by modifying the critical field strength. This optimisation of the critical electric field values is done for streamer breakdown calculations for a UAV alongside OHTLs.

4.4 Switching Impulse Breakdown for Large Air Gaps

To determine the insulation strength with the UAV alongside a phase conductor, as in Figure 4.10, the Rizk equations are used.

Rizk's model is used to predict the safe distances for both a 132kV and 400kV OHTLs. A geometric factor of the electrode configuration (conductor-UAV) is once again determined using CADFEKO.

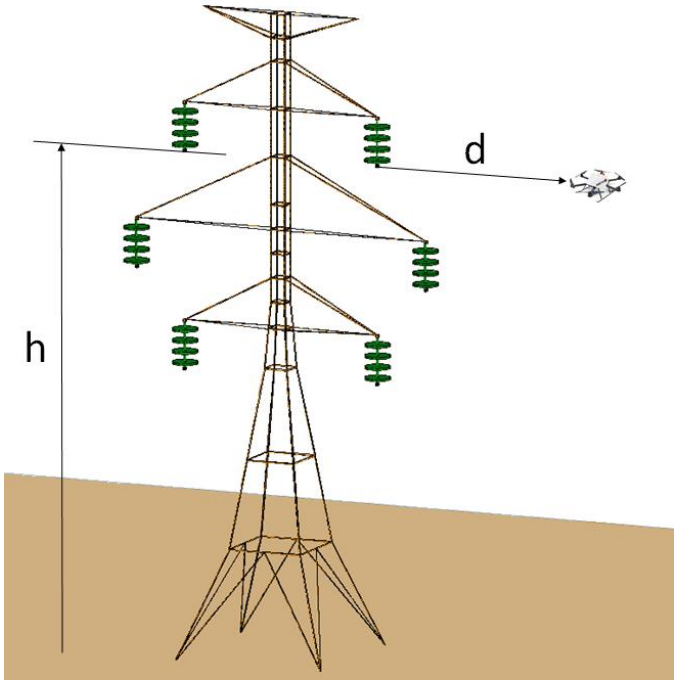

Figure 4.10: The analytical equations can be used to determine the minimum approach distances alongside phase conductors (after, [6]).

The approach to determine the MADs for a floating object alongside a phase conductor (single air gap) is different to that of the dual air gap. Leader and streamer breakdown inception voltages only need to be compared for a single air gap to determine which is dominant. Streamer breakdown will occur for small gaps, whereas large air gaps will break down according to Equation 4.5.

The analytical equations describing leader breakdown are used for the conductor-rod configuration [1]:

$$U_{lc} = 2247/\left(1 + ((5.15 - 5.49 \cdot \ln a)/(d \cdot \ln(2d/a)))\right) \qquad [4.5]$$

The leader breakdown, U_{lc}, is the breakdown voltage in the gap of length d, and a is the conductor radius. An example of the minimum leader breakdown voltage and CFO voltage are plotted in Figure 4.11 for the UAV alongside 400kV OHTL conductor.

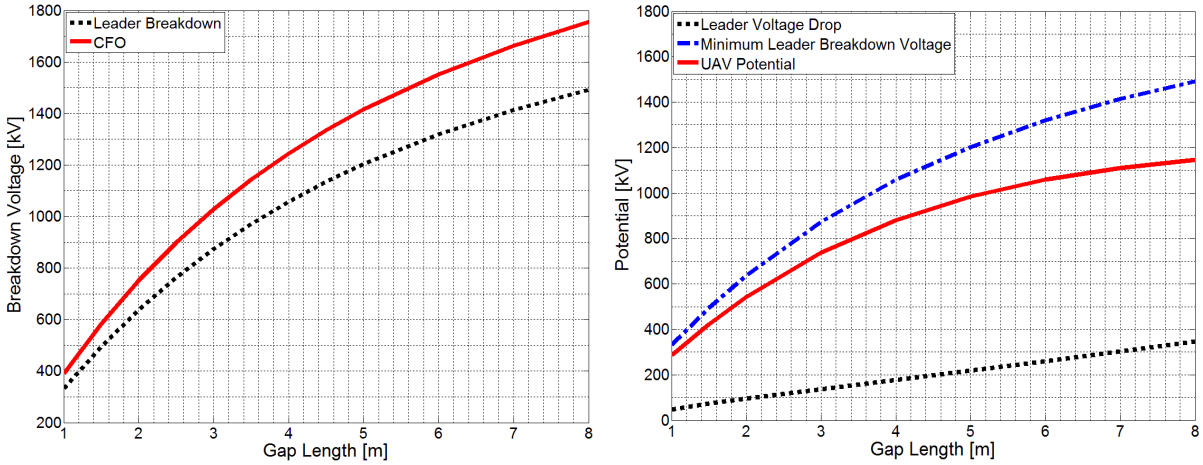

(a) (b)

Figure 4.11: Analytical equations are used to determine breakdown effects such as (a) the CFO voltage and (b) the potential on the floating object.

Once the breakdown voltage is determined as a function of the gap length, the BSL of the line can be used to determine the minimum breakdown strength. For a 400kV line, the BSL is 1050kV [7]. Figure 4.11(b) shows the MAID (from the minimum leader breakdown voltage) to be approximately 3.8m. This is in a similar range to the predicted values in section 2.2 by the standards.

Using this method, a table of MAIDs is determined for the OHTLs of interest. The table is formulated according to the range of possible TOVs for each respective OHTL. The OHTLs examined are the 132kV and 400kV line networks.

MAIDs are determined (Table 4.3) using base values pertinent to the respective system voltages. For all calculations, a standard deviation of 5% was used.

T [p.u.]	132kV	400kV
1	0.45 m	1.2 m
1.5	0.65 m	1.85 m
2	0.85 m	2.7 m
2.5	0.97 m	3.7 m
3	1.22 m	5 m
3.5	1.4 m	7 m

Table 4.3: The predicted MAIDs for the Astec Firefly alongside phase conductors of OHTLs.

The analytically determined values in Table 4.3 are plotted against the standards in Figure 4.12 for comparison.

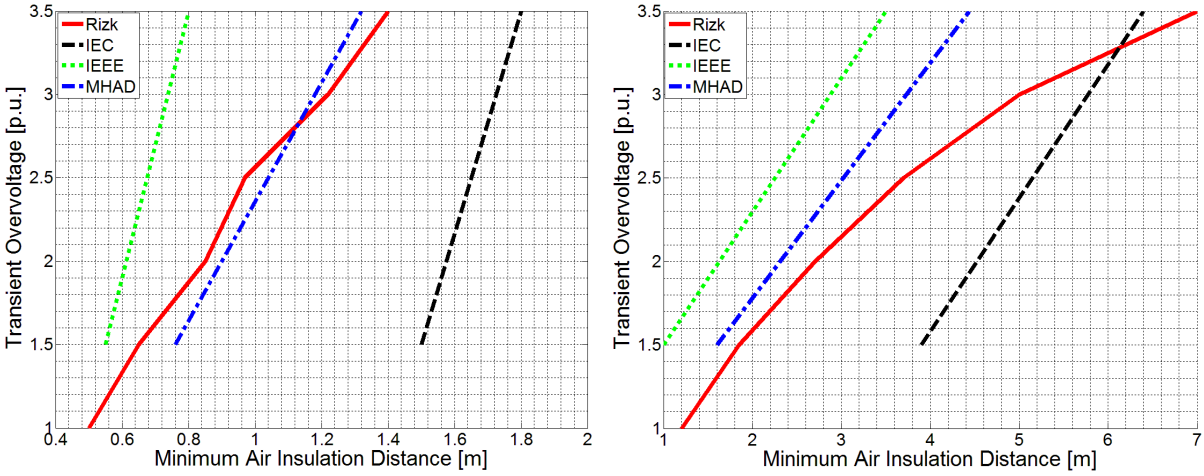

Figure 4.12: The comparison between the standards suggested MAIDs and Rizk's predictions specific to the Astec Firefly.

As discussed in Chapter 2, the standards adopt a worst-case scenario approach which is built on empirical data. The Rizk equations used in this chapter are specific to conductor-UAV air gap breakdown.

4.5 Summary and Conclusions

To determine MAIDs for a UAV in the proximity of OHTLs, analytical equations are used to confirm the experimental work in Chapter 3. The analytical method is then used to derive safe-fly zones alongside OHTLs.

FEKO, a CEM package, is calibrated to the measurement environment used for switching impulse testing in Chapter 3. Linear tests are used to derive confidence in both the setup of the measurement and the simulation model. FEKO is then used to determine a geometric factor as an input into the analytical expressions developed by F. Rizk.

Rizk's equations were successfully compared to measured breakdown values in Chapter 3. Suggested critical electric field values for streamer breakdown were

optimised to fit the measured curve. These values are specific to the conductor-UAV and UAV-cage configurations. These critical electric field values are derived for use in determining the risk for a UAV alongside OHTLs.

To specify MADs for UAVs alongside OHTLs, Rizk's equations were once again used in conjunction with FEKO (to determine the geometric factor for a UAV-specific solution). The MAIDs were determined for a 132kV and a 400kV OHTL and compared to the standard's (worst-case scenario) predictions.

Confidence in the predicted values is derived from the comparisons with IEC and IEEE standards for live-line work.

Historical line data can be used to ascertain the highest TOV expected on the OHTL. To determine the MADs from the MAIDs, an appropriate safety factor must be added to the predicted breakdown distances.

4.6 References

[1] F.A.M. Rizk, 'Switching Impulse Strength of Air Insulation: Leader Inception Criterion", *IEEE Trans. Power Del.*, Vol. 4, No. 4, pp. 2187-2195, Oct. 1989.

[2] F. Rizk, "Effect of Floating Conducting Objects on Critical Switching Impulse Breakdown of Air Insulation", *IEEE Trans. Power Del.*, Vol. 10, No. 3, pp. 1360-1370, July, 1995.

[3] [Online]. Available: EMSS, http://www.feko.info/, Last visited September 2013.

[4] Matthew Groch, "The Effect of Small Airborne Systems near High Voltage Lines", University of Stelenbosch, Final Year B.Eng Project, Tech. Rep., 2011.

[5] *Insulation Co-ordination – Part 2: Application Guide*, IEC 60071-2, 1996.

[6] James Beswick – National Grid, UK Transmission (James.Beswick@nationalgrid.com), "Re: HV Tower Clearances", E-mail to M. Groch (15478602@sun.ac.za), 27/09/2012.

[7] *Overhead Electrical Lines Exceeding AC 45kV – Part 3: Set of National Normative Aspects*, Standard EN 50341-3-9, 2001.

Chapter 5

Aerial Measurements and Simulations of Power Line Sparking Radiation Characteristics

Knowledge of power line radiation characteristics can be used in the design and layout of OHTLs to mitigate the noise radiating into "radio-quite areas".

Previous work has been done on the topic by P Kibet-Langat [1]. In his work, Kibet-Langat compared ground-based measurements (with a spark gap connected to a phase conductor of a three phase line) to measurements made in the laboratory, small-scale measurements and a CEM solution.

In this Chapter, aerial sparking measurements are compared to a MOM CEM solution.

5.1 Aerial Sparking Measurement Strategy

The available line at the SKA site is a 22 kV generator-run line extending approximately 1135m to supply farm houses (Figure 5.1).

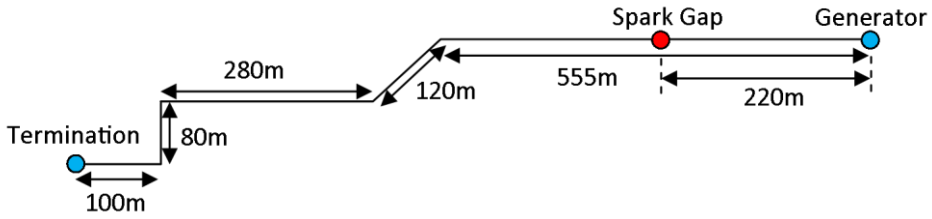

Figure 5.1: The Klerefontein power line layout depicting the spark gap generator's position on the line.

The most favourable spark gap position was determined primarily by the surrounding terrain (proximity of trees to the intended flight path) and working

length of the line. Ten wavelengths are required at the measurement frequency to induce travelling wave radiation characteristics for the line [1].

Figure 5.2: The trees close to the transformer as seen from the spark gap position.

Ideally, a transmission line without bends would be studied to determine a general line pattern; thereafter, the effects of bends could be determined.

To get the line to spark, a mobile spark gap was used (Figure 5.3 [1]). This device consists of a clamp which is attached to the line, an adjustable rod-rod spark gap, and a sphere which reduces the lower rod's potential to promote sparking.

(a) (b)

Figure 5.3: The spark gap connected to the Kelerefontein power line in the position shown in Figure 5.1 (a). The spark gap with a 2mm gap setting is shown on in (b) [1].

A set of flight paths were planned to determine the near-field radiation characteristics of the spark induced currents (Figure 5.4).

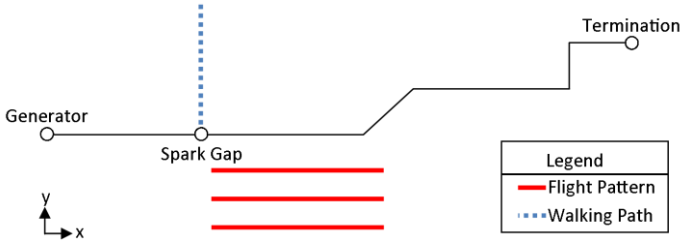

Figure 5.4: Top view of the measurement paths at the Klerefontein power line.

Additional tests were planned, but were not carried out owing to time constraints. To carry out the measurement campaign, specialised instruments are required. The UAV and on-board measurement equipment are briefly described in Section 5.2.

5.2 Aerial Measurement Instrumentation

The aerial measurements were conducted with the help of Ls Telcom[1] of South Africa. A Y-6 copter (Figure 5.5) with on-board measurement instrumentation was used.

Figure 5.5: Ls of SA's Y6 copter used for the aerial measurements.

[1] With thanks to Ls of South Africa (http://www.lsofsa.co.za/index.html) for lending their equipment and assisting in measurement campaign.

The Y-6 copter's ability to carry a relatively large payload enables the user to fit measurement-appropriate equipment. The fitted measurement system is shown schematically in Figure 5.6.

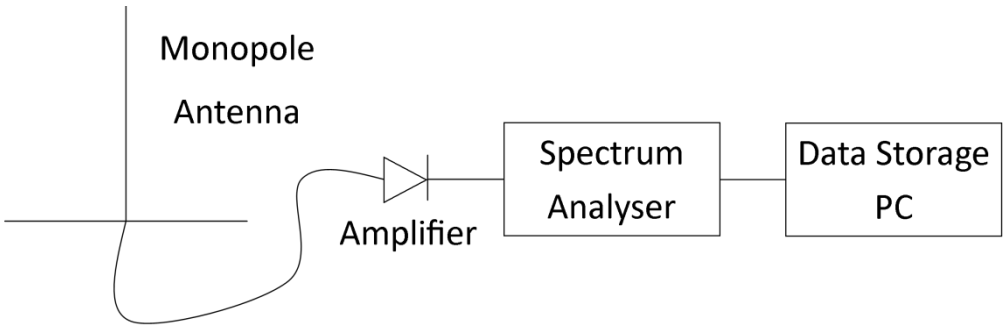

Figure 5.6: The on-board measurement system used for the sparking measurements.

An antenna receives the radiated sparking signal which is then amplified and sampled by a lightweight commercially-available Spectrum Analyser (SA). A high-speed, USB 3 connection to an i_7 computer allows real time data recording.

To sample the near-field with an adequate resolution, the sparking needs to be sampled at the lowest frequency possible. Designing a small, durable, lightweight antenna which is practical to mount on a UAV is challenging for a low frequency range. Typical low frequency antennas are in the order of metres in length.

Two methods were considered to decrease the antenna length – these are namely, active antennas or resistively-loaded antennas. Active antennas are risky in such an uncontrolled environment as strong signals can damage the on-board equipment.

A resistively-loaded monopole antenna was therefore designed and constructed (Figure 5.7). The monopole offers a 360°, broad 3dB beam width pattern (typically 90° before beam-elevation begins to take effect) which ensures that the radiation is detected regardless of the UAV's position. The antenna design is described in Appendix D.

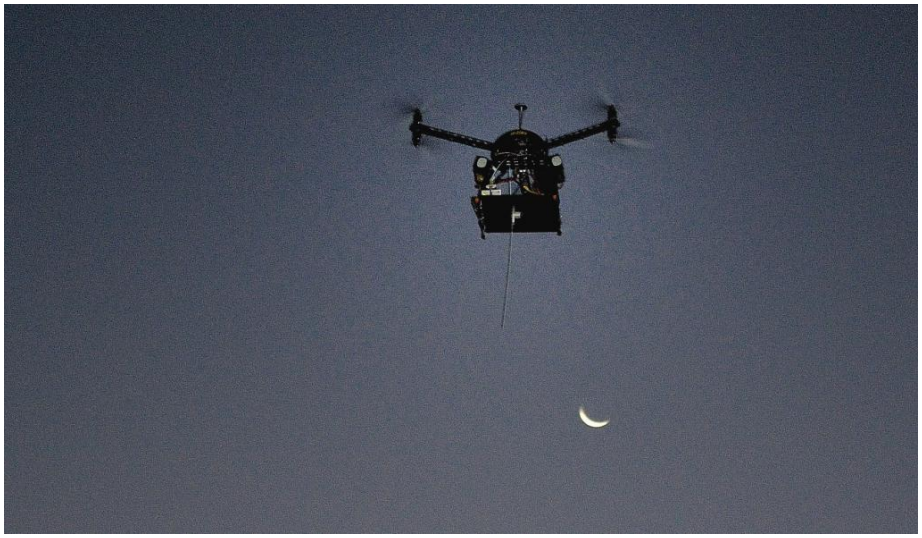

Figure 5.7: A 30-300MHz resistively-loaded monopole antenna mounted under the Y6 copter.

The resistively-loaded antennas were used in the first measurement campaign. Due to time constraints and technical issues during the second campaign, a narrow-band stub antenna was used in the measurements. For future measurement campaigns, it is strongly suggested that loaded-monopoles be revisited due to their broadband nature.

The specifications of the SA are listed as:

- RF Frequency Range 9kHz to 6GHz
- Dynamic Range -151dBm to 10dBm
- Resolution Bandwidth 10Hz to 10MHz
- Digitization of IF Data 80MSPS
- Instantaneous Bandwidth 20MHz
- Sweep Speed Maximum of 24GHz per second

The fast sampling speed opens up a few options. Sampling can be done at one or multiple discrete frequencies, or even over a defined frequency band. Experimenting with the resolution bandwidth (RBW), gain and attenuation settings showed that the claimed -151dB dynamic range was not attainable. Preferred measurement settings which picked the sparking energy up most clearly were:

- RBW = 100kHz
- Attenuation = 0dB
- Gain = 3 (Maximum)

The settings resulted in a noise floor at approximately -83dBm which is adequate for near-field measurements. Collected data from the SA was flushed to an i_7 computer for storage.

5.3 Building on Previous Studies

Ground-based measurements of power line radiation characteristics were studied in [1].

In [1] field measurements were compared to measurements made in the laboratory, small-scale measurements and a CEM solution.

This showed that:

- Sparking energy content was evident to above 3.5GHz.
- The power line acts as an end-fire antenna.
- The power line acts as a low pass filter and therefore attenuates conducted high frequency signals faster than low frequency signals.

Sparking propagation characteristics were investigated for longitudinal, lateral and height profiles.

5.4 Aerial Sparking Measurements – First Round

The data from the first measurement campaign was unusable, principally realted to EMI issues. Additionally, the SA was not set to its maximum sensitivity for the measurements. In the SA's playback files (in Figure 5.8) it can be seen that the

noise floor is in the vicinity of -70dBm. A sensitivity of -120dBm can be achieved when the SA is correctly set up.

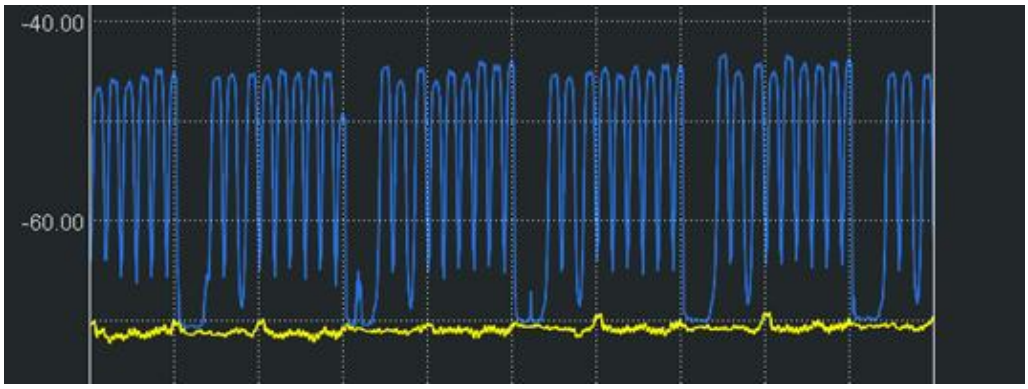

Figure 5.8: A playback of the measured signal with maximum hold activated shows the spurious interference introduced by the ADC's clipping.

Strong signals are present at the same level across the band. This, as discussed in the Section 5.5, is due to the SA's susceptability to frequencies between 2.1GHz to 2.4GHz. Strong signals in this band saturate the ADCs, which in turn, induces clipping.

For this first round of measurements, the SA had averaging activated. The transient events were not visable as they were averaged with the noise floor.

The flight log files showed that the GPS data of the flight paths was not recorded. Interference from the i_7 computer cables prevented the GPS from locking in the majority of the measurements. This problem was later solved by adding multiple ferrite cores at the ends of the cables.

Another problem encountered was the resulting erratic flight paths (Figure 5.9). Due to local EMI preventing the GPS from locking, as well as time pressures, the UAV was flown manually in a stiff breeze.

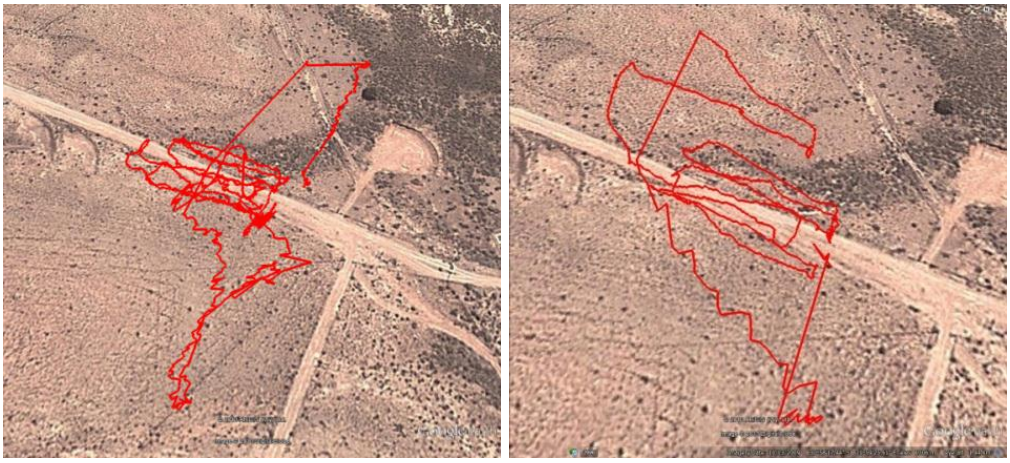

Figure 5.9: The manual flight paths for the flights in which the GPS locked. Heavy wind made flying good flight paths difficult.

With the GPS-lock problem solved, and the implementation of differential GPS, more accurate, automated flight paths can be flown.

The lack of usable data prompted another measurement campaign after the issues encountered in the first campaign were resolved. The EMC issues are dealt with in 5.5.

5.5 EMC Mitigation Measures

To further investigate, and solve the issues encountered in the first measurement campaign, a visit to Ls of SA's offices in Johannesburg was planned along with a colleague, Hardie Pienaar. The goals of the visit were to:

- Get better acquainted with the system
- Examine the EMC issues
- Investigate the sensitivity of the SA
- Determine the autopilot's reliability and accuracy through test flights.

To investigate the source of the spurious content, the SA was connected to a laptop for real-time monitoring. With the UAV in the same state as in the measurements,

the real-time sampling was observed (Figure 5.10). Maximum hold was activated and the input was terminated in a 50Ω load instead of an antenna. The goal of this test was to isolate the system to determine the source of the spurious content in the spectrum (blue signals in Figure 5.10).

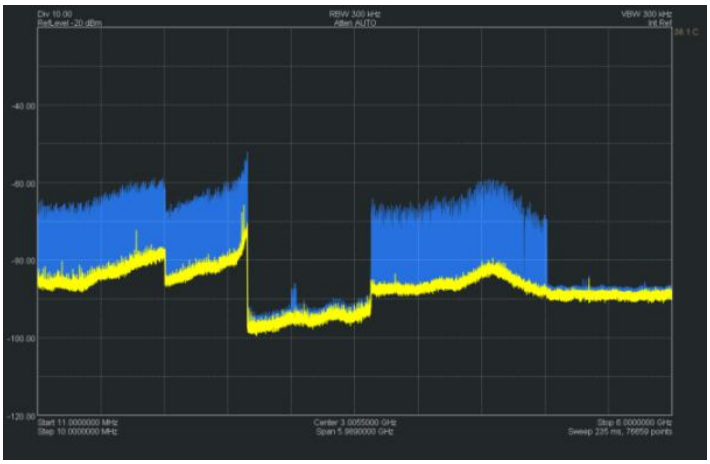

Figure 5.10: The measured broadband spurious content detected in the measurements.

To investigate the cause of the spurious content, a current probe was used to track the cable currents with the system in all of its possible states (Figure 5.11).

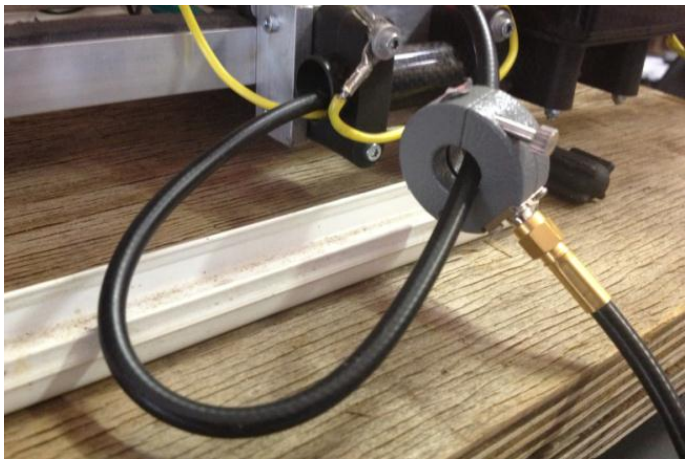

Figure 5.11: The current probe measuring the cable currents in the measurement equipment chain.

The current probe was connected to a Rohde and Schwarz FSH SA to monitor the susceptible SA in its operable band. This would show the relative signal strength coupling onto the cables and into the system.

Of particular interest is the USB 3 cable connecting the i_7 to the SA. The relative signals measured on the i_7's USB cable are plotted in Figure 5.12 with the UAV in all possible states of operation.

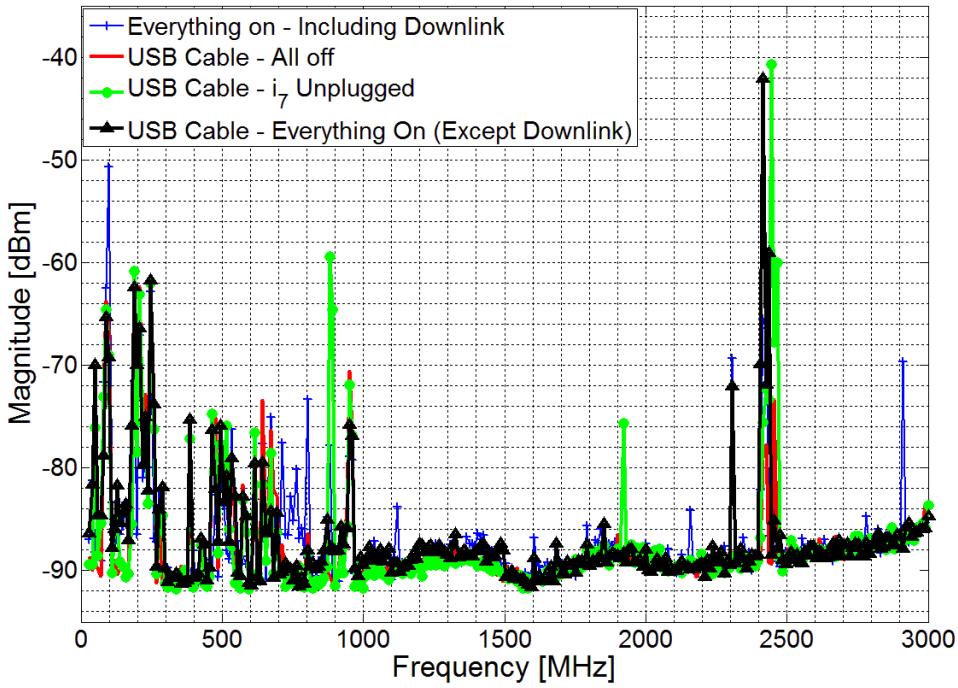

Figure 5.12: The interference on the USB 3 cable measured by the current probe.

The interference signals being carried by the USB 3 cable, while strong, are all narrow band. It was therefore suspected that the interference was generated in the SA itself – possibly as a result of the strong signals being carried through the USB cable.

To determine the source of the interference, the SA was isolated from the UAV system. It was connected to a laptop via a USB 3 cable and the antenna input port was once again terminated.

Figure 5.13: The SA was isolated from the system to determine if the interference was generated internally or carried through the long cables in the UAV system.

With the transmitter in Figure 5.13 off, no interference is detected. Radiating a signal at 2.4GHz via a stub antenna produces the same interference displayed in Figure 5.10. This proves that the broadband spurious content is generated within the SA, and not carried through the UAV system.

Opening the enclosure reveals a possible reason for the SA's susceptibility (Figure 5.14).

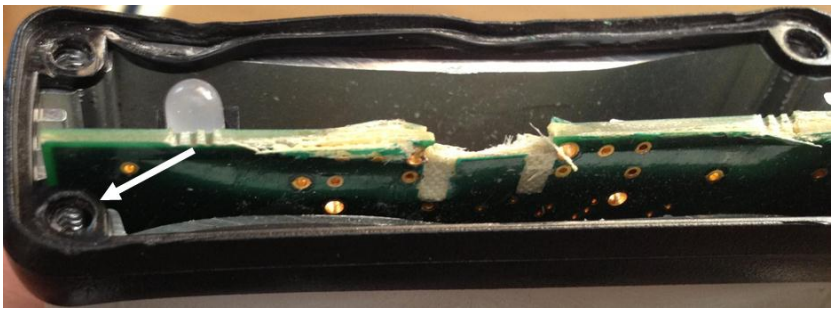

Figure 5.14: The lightweight, commercially-available, SA with the faceplate (USB side) removed. The arrow shows the plastic rim creating a gap between the faceplate and enclosure's body.

With the faceplate removed it is evident that the enclosure has no shielding properties. Contact is only made between the face-plate and the body of the enclosure by four screws. A small gap is created by the plastic rim surrounding the

enclosure entrance. Any (high frequency) conducted currents travelling over the shield can move through the gap and into the enclosure. These high frequency currents could couple inductively onto the board.

A close look at the faceplate and the board reveal that the USB port is not connected to the enclosure, but rather to the board's ground. EMI can couple onto the USB cable's shield and be carried into the SA which may then induce clipping in the ADCs.

To correct the SA's shielding susceptibility to RFI, a mock enclosure was designed (Figure 5.15) as a concept-shield to prevent external signals from clipping the ADCs. Care was taken to ensure that the foil made contact with the grounds of the SA's input and output connectors.

Figure 5.15: A foil shield was used to demonstrate the need to properly shield sensitive measurement equipment in noisy environments.

The strongest source in the proximity of the SA during measurements is the UAV's downlink (telemetry link). To test the enclosures effectiveness, a radio transmitter was placed very near to the shield to create a harsher environment than normal. If the enclosure passes this test, it will be deemed satisfactory for the next measurement campaign.

The foil enclosure reduced the EMI to the point where clipping of the ADCs no longer occurred. This shows that the interference is generated by induced current flowing over the USB shield and onto the board. It is also possible that current moves through the seams of the enclosure.

For more comprehensive testing, a shielded box was designed with the aim of determining the effectiveness of shielding only the SA (Figure 5.16). The effect of turning the enclosure into an EMC cabinet and a U-plate was also investigated by removing sides of the enclosure.

Figure 5.16: The designed SA enclosure, with good contact at both connectors.

The SA was placed in a cardboard box and covered with multiple, overlapping layers of foil. The antenna's input SMA connector was secured to the foil with a washer and nut. The USB cable's braiding was exposed by removing the plastic covering close to the connector. Contact between the USB braiding and foil was ensured by tightening a cable tie around the foil covering the exposed braiding.

The effectiveness of the enclosure was tested by placing the 2.4GHz frequency hopping radio transmitter alongside the enclosure (Figure 5.17). The antenna was placed in both the horizontal and vertical polarisation to induce currents travelling both length and width-ways over the enclosure.

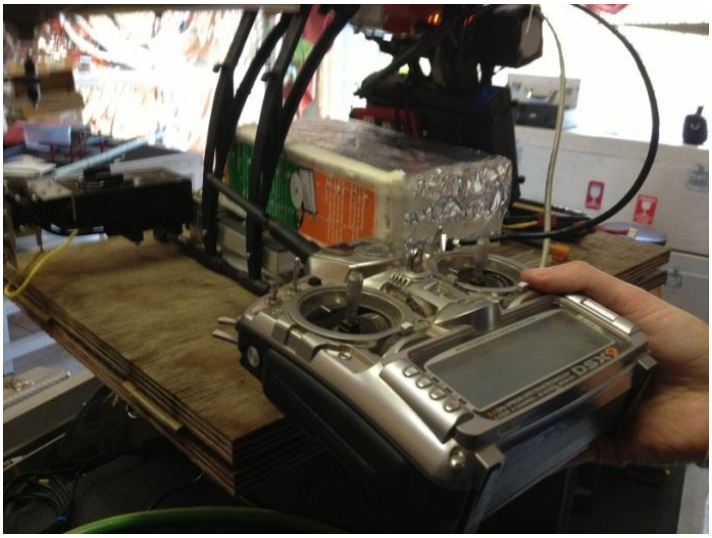

Figure 5.17: The enclosure housing the SA was tested by placing the 2.4GHz radio transmitter alongside the enclosure.

Removing a side of the enclosure facing away from the telemetry link as (shown in Figure 5.17) yielded poor results. This is because currents induced on the enclosure surface (or USB cable) by the telemetry link travel into the enclosure. It was determined that the best solution would be to design a meshed enclosure which would allow for heat dissipation.

The enclosure's shielding effect can be seen in Figure 5.18.

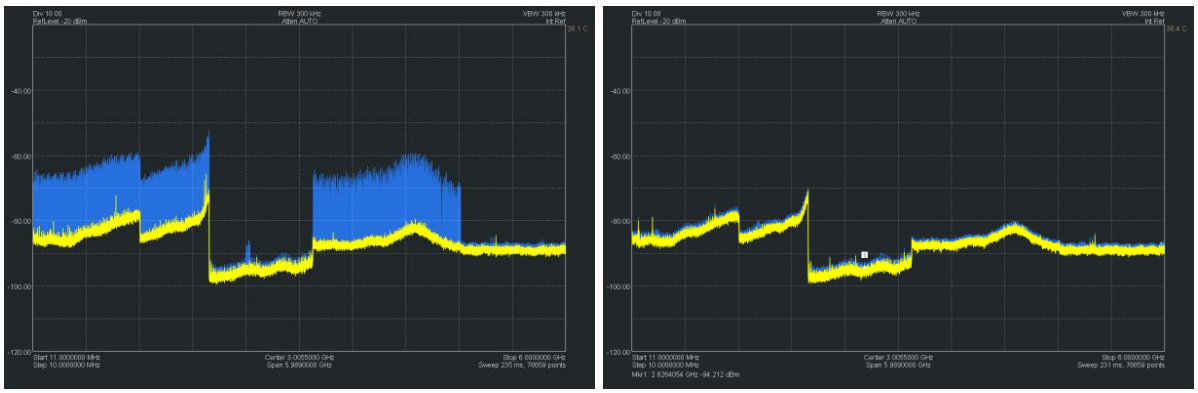

(a) (b)

Figure 5.18: The before (a) and after (b) spectrum plots demonstrating the effectiveness of placing the SA in an EMC enclosure.

As seen by Figure 5.18, EMI has been reduced to the point that the ADCs no longer clip. Through the course of the investigation, important findings were made regarding good EMC practices for UAVs. These are documented in Appendix B.

5.6 Aerial Sparking Measurements – Second Round

With the issues encountered in the first round of measurements resolved, another measurement campaign was launched. The spark gap was placed in the same position on the line and the same flight paths were planned.

5.6.1 Ground-Based Sensitivity Measurement

To determine the sensitivity of the SA, a walking test was done. The SA was connected to the 12.5cm resistively-loaded monopole antenna and a GPS module logged the path (Figure 5.19).

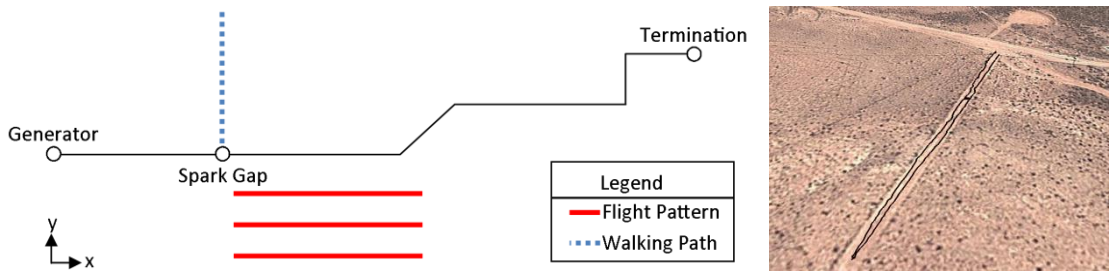

Figure 5.19: The path of the walking test to determine the signal levels for the measurement configuration.

By creating a KML file [2] using MATLAB R2009a, the relative signal strength along the GPS coordinates was plotted in Google Maps (Figure 5.20).

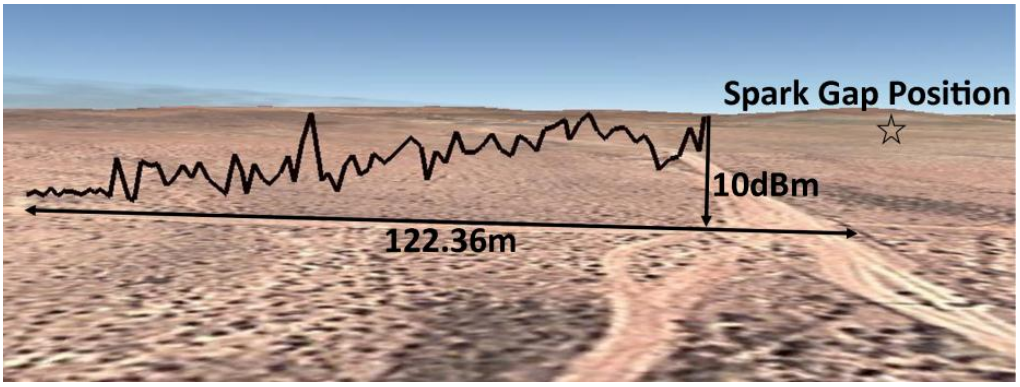

Figure 5.20: The relative signal strength plotted at the measured GPS coordinates.

The walking test shows that at approximately a height of 1.5m, the measurement system can detect the sparking energy up to approximately 120m away from the power line. A preamplifier can be inserted into the measurement chain to improve the sensitivity of the system.

5.6.2 Aerial Sparking Measurements

The aerial measurements were once again done in strong winds - as shown in Figure 5.21. Wind-speeds at the time of testing reached in excess of 20kmh^{-1} (or 6ms^{-1}) at ground level.

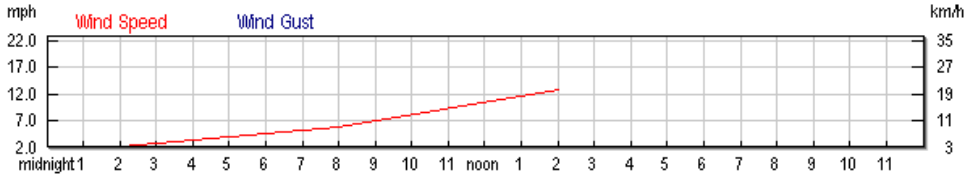

Figure 5.21: The wind speed at the time of measuring was extracted from an online source [3] – measured at Vanwyksvlei (close to the testing site).

The strong winds made it difficult for the UAV to fly accurate paths. Two grids were flown at different heights alongside the power line (Figure 5.22).

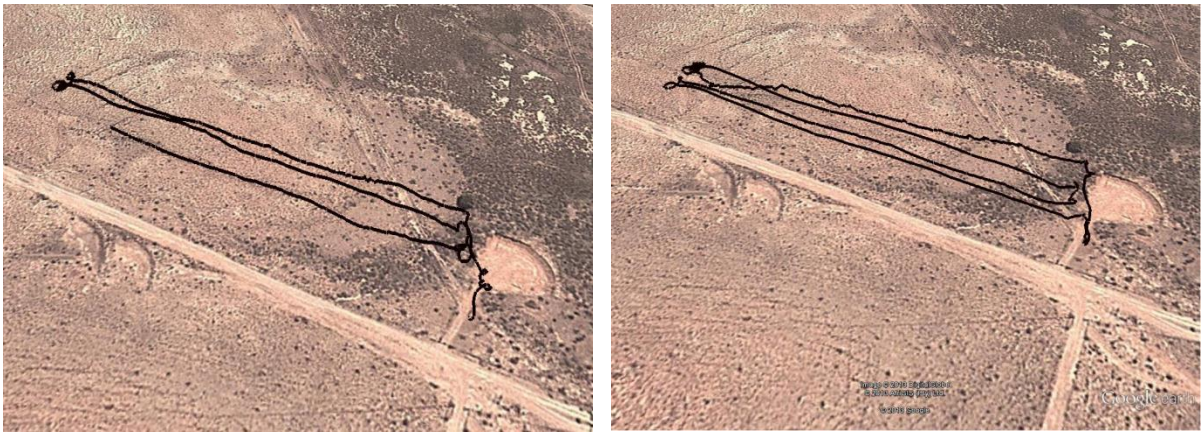

(a) (b)

Figure 5.22: The two flight paths flown are displayed in Google Maps. Flight 1 (a) was flown at a height of 20m and Flight 2 (b) at 14m.

To process the results, the flight paths are broken up into straight grid lines. Figure 5.23 shows the grid lines marked number 1 to 4. All grid lines are approximately 212m in length.

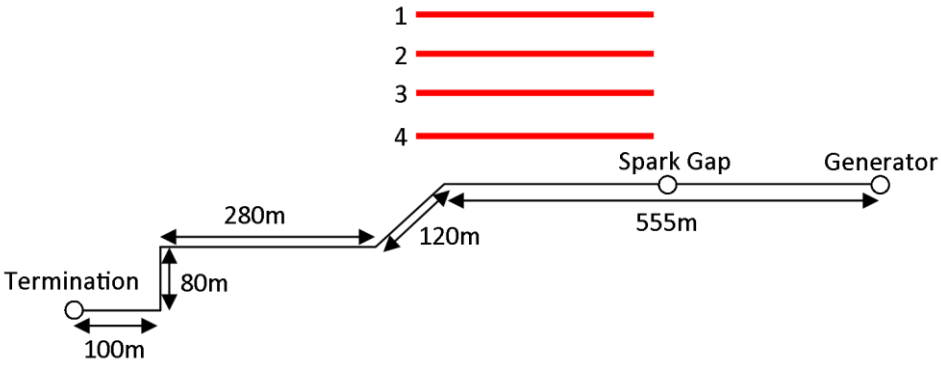

Figure 5.23: The flight paths are separated into the straight flight paths and numbered for processing.

The SA settings for flight 1 were as follows:

- Frequency Range = 229MHz – 249MHz
- RBW = 100kHz
- Attenuation = 0dB

- Gain = 3 (Maximum)
- Sweep Time ≈ 16ms

For the first flight, Grid line 4 was not measured as the SA reached its maximum recordable file size.

It is known that sparking occurs 2 or 3 times per half cycle for a 2mm spark gap on a 22kV line [1]. This means that sparking is initiated approximately every 5ms. Setting the SA's sweep time to 16ms ensures that sparking is always detected – albeit at different points on the wave for each frequency point. A recording of a typical sparking event is shown in Figure 5.24. The persistence feature shows a heat map of multiple frames which highlights the different levels of sparking sampled as the UAV moves through different field levels.

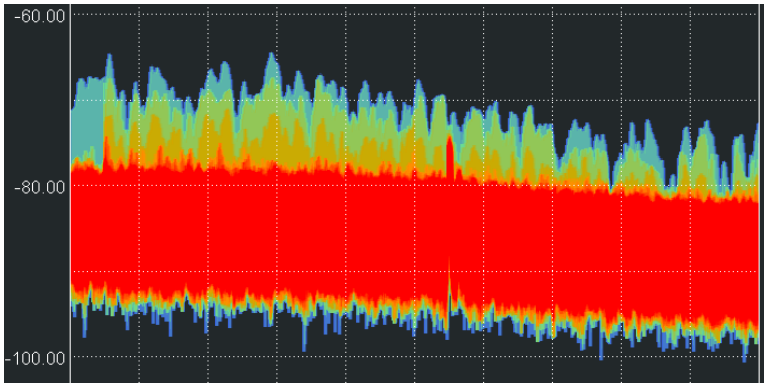

Figure 5.24: The frequency sweep persistence recording of a typical sparking event captured by the SA. The y-axis units are in dBm.

The recorded flies were played back to determine the regularity with which the SA detected the sparking events. In the processing stages, a single frequency is extracted from the recorded file. For this single frequency, it is sometimes possible that the sparking event is either missed, or only a portion of the signal is captured. It is therefore necessary to envelope the resulting measured signal to obtain the general sparking profile for the grid lines.

The flight path was broken up into separate grid lines, defined in Figure 5.23, and plotted in Figure 5.25 by creating a KML file in MATLAB. The KML toolbox is

available at [2]. The estimated average distances for the grid lines from the power line are displayed in Figure 5.25.

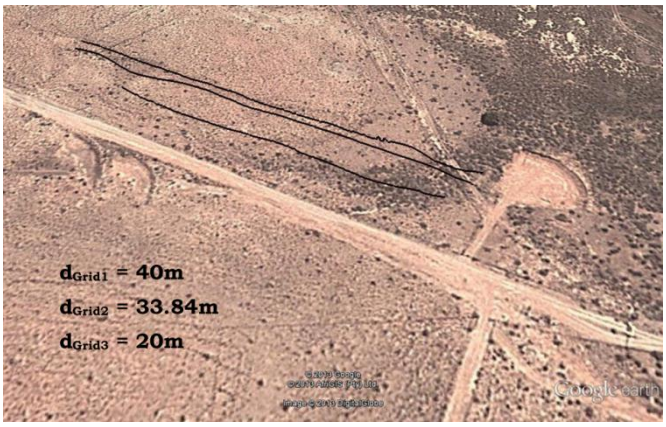

Figure 5.25: The grid lines for flight 1. The grid lines were plotted in Google Maps using R.F. de Oliveira's KML toolbox v2.6 [2].

To observe the UAV's horizontal drift from the intended flight path, x-y coordinates of the flight relative to the spark gap are required. The GPS coordinates were converted to Cartesian coordinates by selecting two reference points (Figure 5.26).

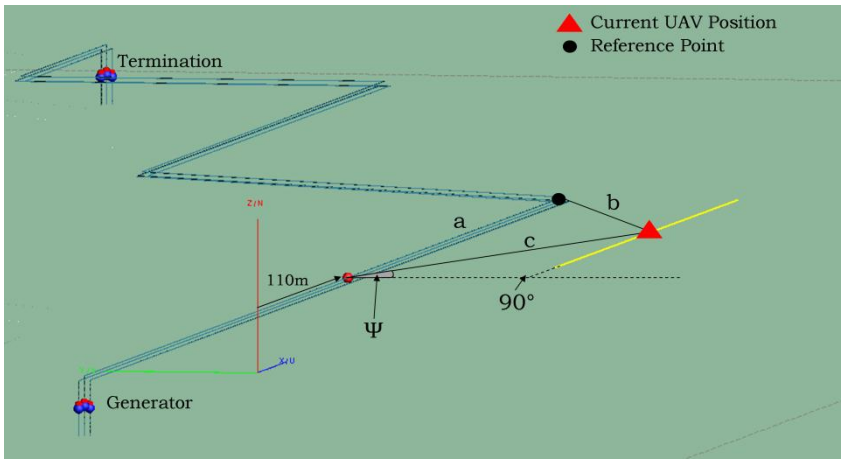

Figure 5.26: The information required to transform the GPS coordinates to Cartesian coordinates.

The spark gap (0m; 0m) and the power line bend (264.64m; 0m) are selected as the reference points. The GPS coordinates of these points were determined using

Google Maps. Distances a, b and c (at each UAV position along the grid line) are calculated using the greater circle formulation described in Appendix C. The relative UAV position can then be determined from the angle, Ψ, and distance c using basic trigonometry.

The processed data (discussed in Appendix C) is plotted in Figures 5.27 to 5.29 for the three grid lines of flight 1.

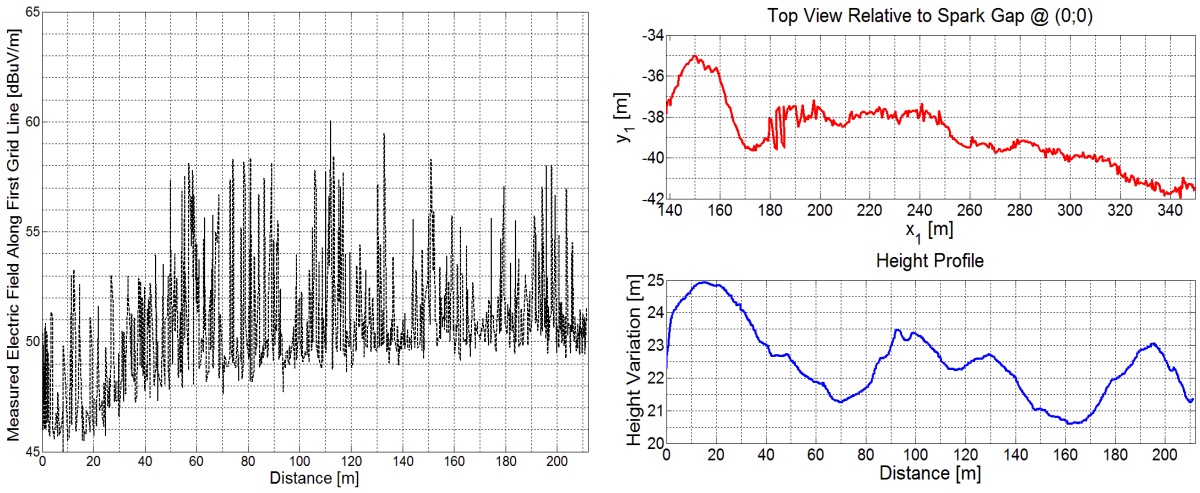

(a) (b)

Figure 5.27: The electric field profile (a) and the relative position and height (b) are plotted for flight 1, grid line 1.

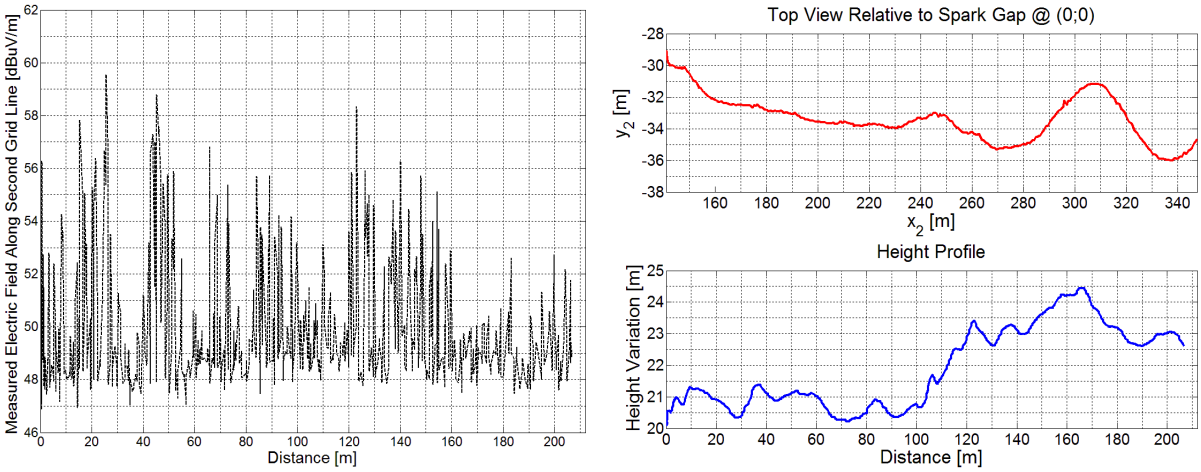

(a) (b)

Figure 5.28: The electric field profile (a) and the relative position and height (b) are plotted for flight 1, grid line 2.

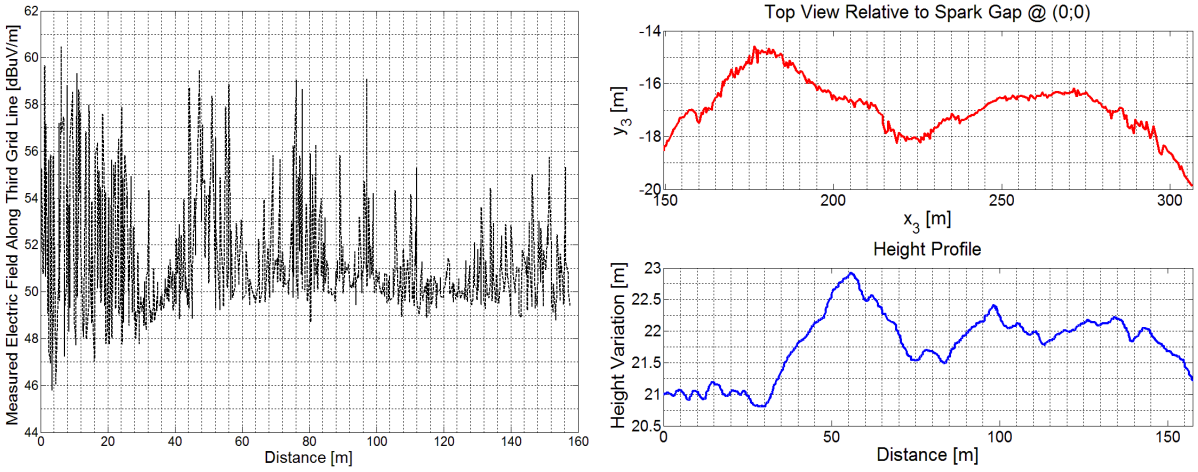

(a) (b)

Figure 5.29: The electric field profile (a) and the relative position and height (b) are plotted for flight 1, grid line 3.

A few observations can be made from the grid line plots:

- The measured signal level is very high - in the region of 60dBµV/m.
- Peaks and nulls are measured along the line – no pattern between the individual grid lines is discernible.
- The radiated power does not seem to attenuate down the line at this frequency.
- The height variation (4m) and positional drift require that special attention be paid to the simulation electric field sample positions for an adequate comparison.
- The SA does not always catch the peak of the sparking events. An envelope must therefore be taken of each electric field profile.

The same procedure was followed for flight 2. The estimated average distances for the grid lines from the power line are displayed in Figure 5.30.

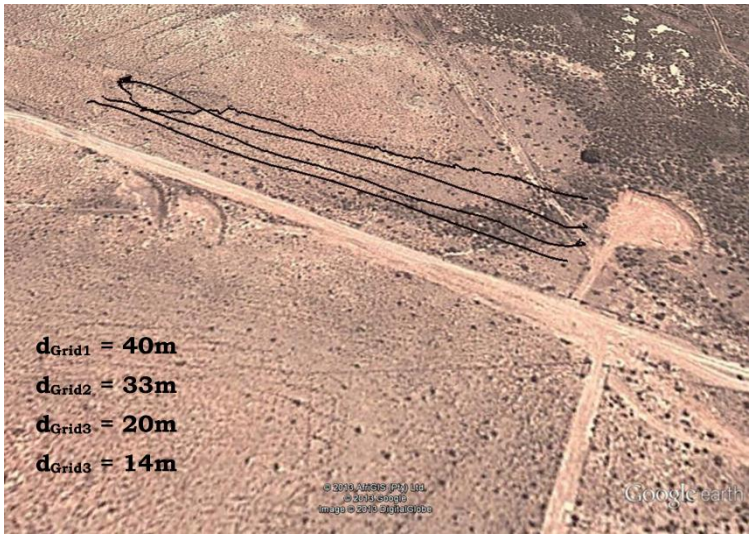

Figure 5.30: Flight 2 grid lines. The grid lines were plotted in Google Maps using a KML toolbox v2.6 [2].

The SA settings for flight 2 were as follows:

- Frequency Range = 234MHz – 244MHz
- RBW = 100kHz
- Attenuation = 0dB
- Gain = 3 (Maximum)

The frequency band of the SA sweep was reduced from 20MHz to 10MHz to increase the recording time for a longer flight. The processed data (discussed in Appendix C) is plotted in Figures 5.31 to 5.34 for the four grid lines of flight 2.

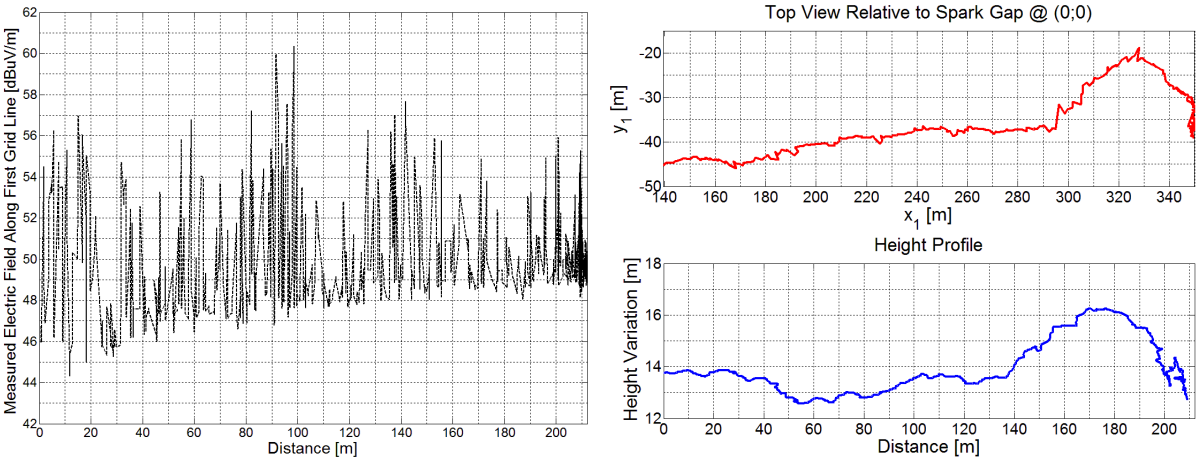

(a) (b)

Figure 5.31: The electric field profile (a) and the relative position and height (b) are plotted for flight 2, grid line 1.

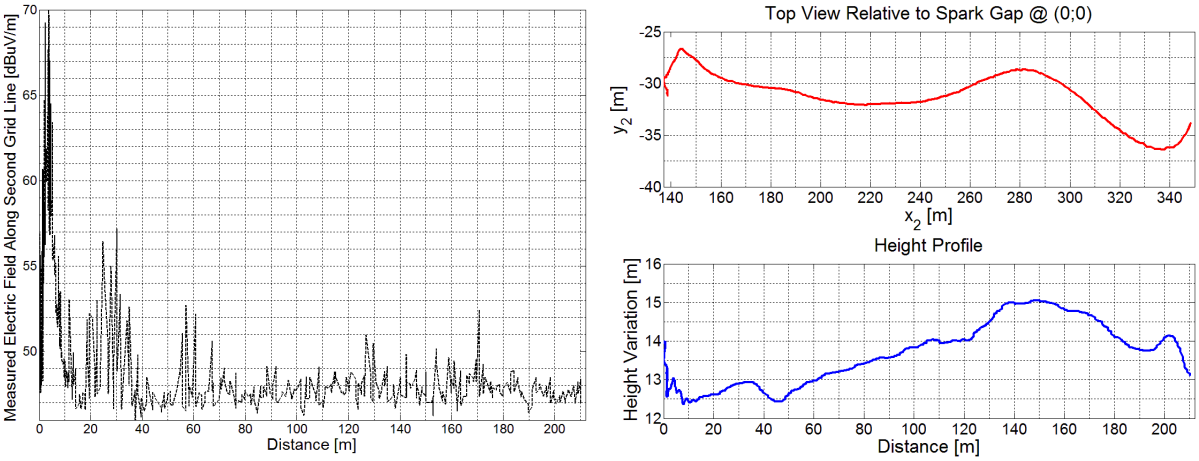

(a) (b)

Figure 5.32: The electric field profile (a) and the relative position and height (b) are plotted for flight 2, grid line 2.

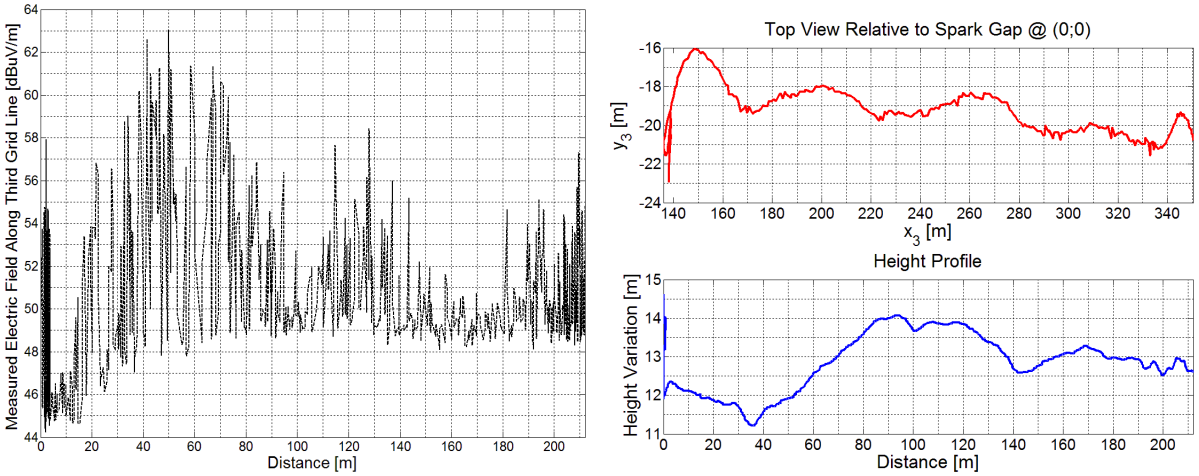

(a) (b)

Figure 5.33: The electric field profile (a) and the relative position and height (b) are plotted for flight 2, grid line 3.

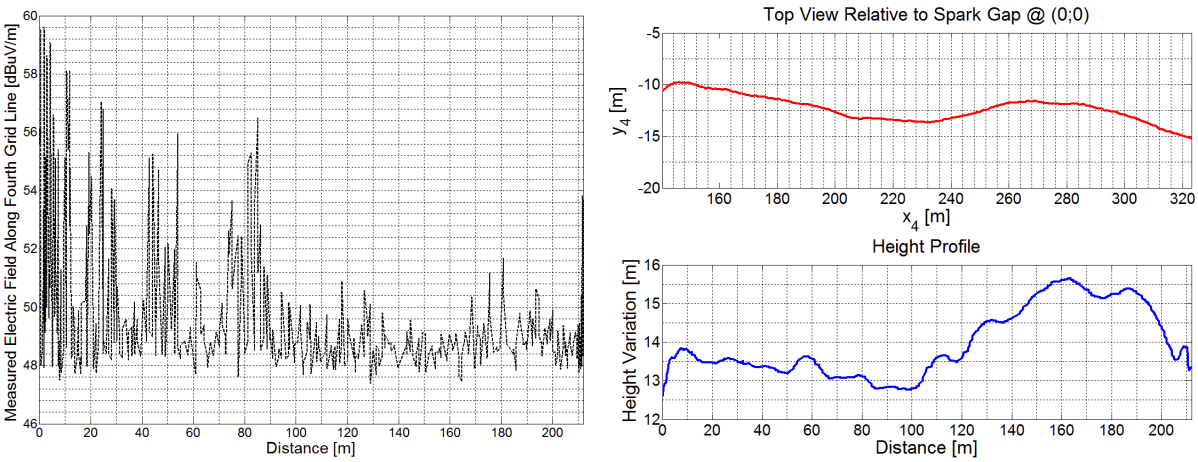

(a) (b)

Figure 5.34: The electric field profile (a) and the relative position and height (b) are plotted for flight 2, grid line 4.

The measured electric field profiles for grid lines 2 (Figure 5.32) and 4 (Figure 5.34) are in the noise floor. The grid lines from both flights can now be compared to a CEM solution. The measured electric field profiles are compared to FEKO simulations in Section 5.7.

5.7 FEKO Sparking Profile Predictions

FEKO is used to determine the near-field radiation of the power line sparking. Once determined, the simulation results can be compared to the aerial measurements.

To model the Klerefontein power line, a few simplifications need to be made:

- The wooden poles are neglected. FEKO cannot handle their inclusion with such a large-scale problem.
- The line is modelled at a height of 12.5m in a delta configuration. The conductor sag is not considered.

- The soil properties are modelled using a Sommerfield ground plane with a relative permittivity, ε_r = 3.8 and a dielectric loss tangent = 0.076 [1].
- The power line surge impedance is assumed to be between 300Ω and 500Ω [1] at the measured Frequency – 239MHz. This was checked in the simulations and found to be non-influential on the power line's radiation pattern.

The CADFEKO model (Figure 5.35) is designed to scale with a spark gap positioned at the same point as in the measurements. The sparking source is represented by a 1V wire port as a current injection point to represent the current waves induced by sparking activity.

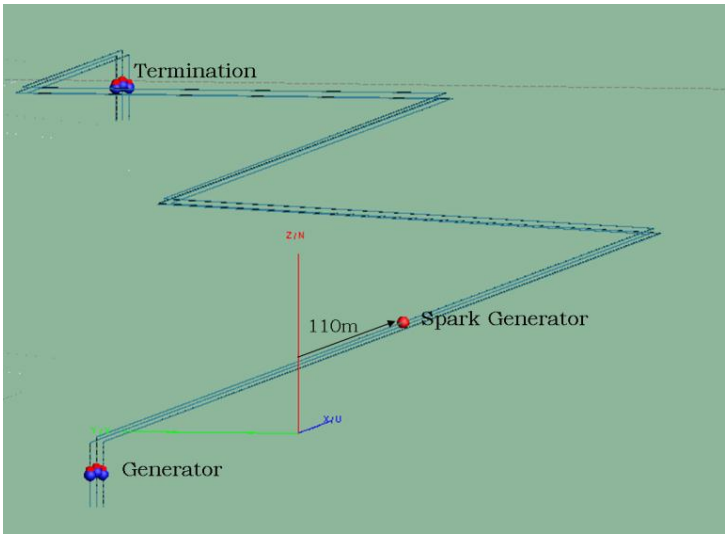

Figure 5.35: The 1.5km transmission line modelled to scale in CADFEKO.

To handle such a large-scale model, the simulations were run on Babbage – Stellenbosch University's Electronic Engineering Department's cluster computer.

The flight paths were inserted into the simulation model environment to check the correlation between the measurement and simulations. Near-field requests were used to sample the electric field at these discrete points. At the measured frequency of 239MHz, a resolution of 12.55cm (1/10th of a wavelength) was selected to ensure good resolution of the sampled near-field. The requested near-fields are shown in Figure 5.36 in yellow.

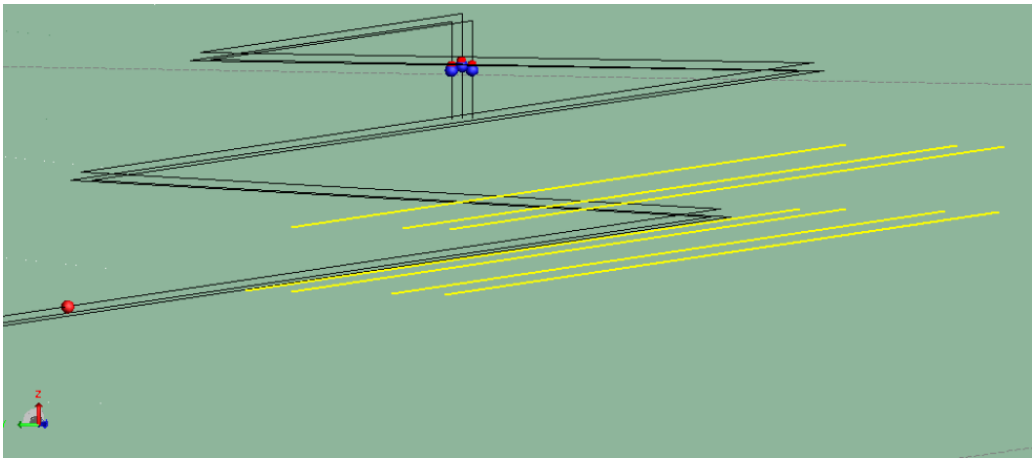

Figure 5.36: The requests of the sampled electric field (representing the grid lines for both flights) paths.

The electric field requests in Figure 5.36 did not account for the wind-induced drift of the UAV. The near-field request paths were set up according to Figures 5.25 and 5.30, where an estimated average distance from the line was selected.

Electric field components in the direction of the line (E_X) were neglected. The antenna could not detect these components as it was slanted at a 45° angle in the y-z plane.

The second grid line of flight 2 is not reported as the measured values were in the noise floor. The resulting electric field values were converted to dBμV/m. To compare features in the near-field pattern, the simulated values were fitted to measured values by scaling the plots in the same way normalising is done (by adding a constant value to fit the maximum). The FEKO predictions were also shifted slightly in the x-direction to line up with the measured values as the near-field requests were marginally inaccurate. The resulting measured and simulated profiles are shown in Figure 5.37.

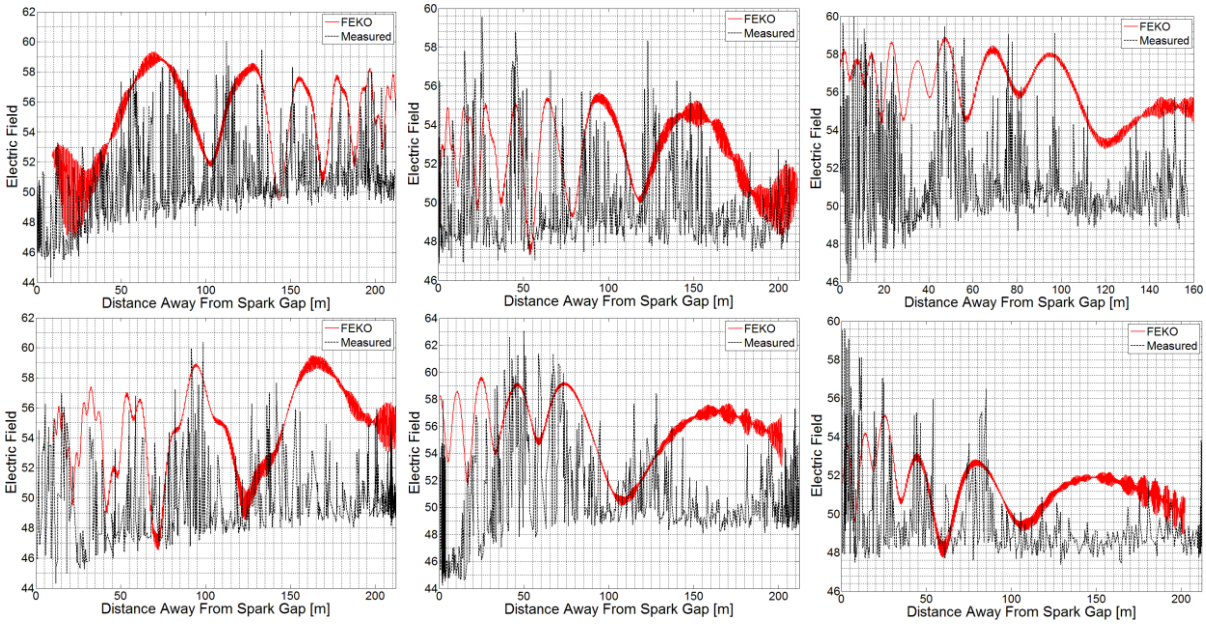

Figure 5.37: The electric field comparisons between the measured and simulated values. Flight 1, grids 1, 2 and 3 are shown at the top - Flight 2, grids 1, 3 and 4 are at the bottom.

The measured and simulated values show good correlation. The complexity of the real-world environment and measurement uncertainties (GPS accuracy of 1.5m) render the problem difficult to simulate exactly. Additionally, features such as the terrain, power line poles and insulators cannot be modelled in FEKO.

In an attempt to improve the correlation between measured and simulated field profiles, the actual flight paths were imported into FEKO. This was done in an attempt to reduce the measurement uncertainties such as the horizontal and vertical (height) positional drift. These factors, as seen in Figures 5.27-5.29 and 5.31-5.34, were excessive due to high wind-speeds at the time the measurements were carried out.

Importing a list of points as a near-field request is not an available feature in CADFEKO. To import the actual flight path grid lines, an EDITFEKO script was written to read the flight path data from text files. To accomplish this, x-y coordinates and GPS height data of the flight paths were written to text files.

For a better representation of the sparking profile, the measured electric field was enveloped for comparison with the simulated sparking profile. Flight 1 comparisons are made in Figure 5.38.

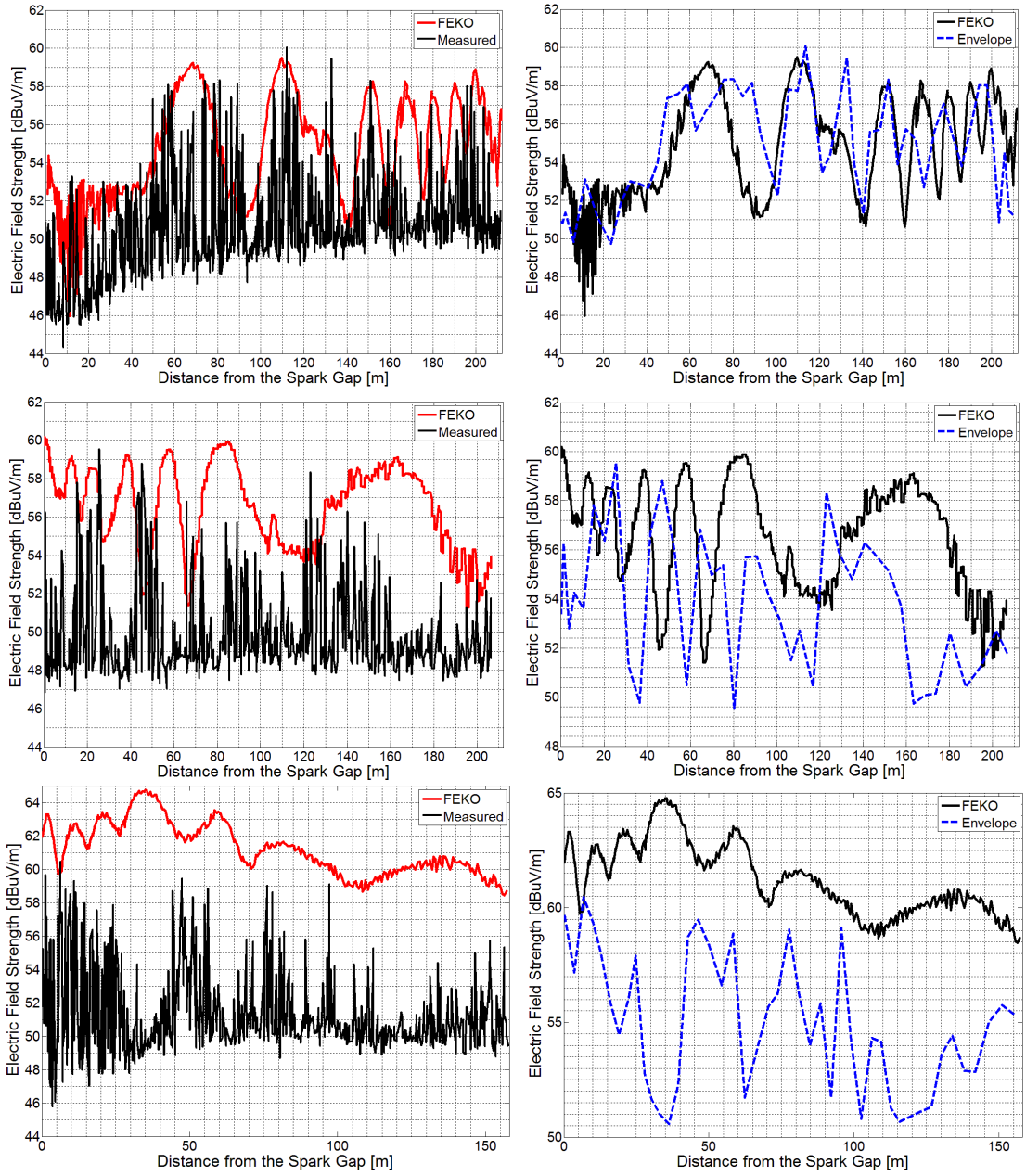

Figure 5.38: The measured and simulated sparking profiles are compared for flight 1: grid line 1 (top), grid line 2 (middle) and grid line 3 (bottom).

The comparisons for Flight 2 are displayed in Figure 5.39.

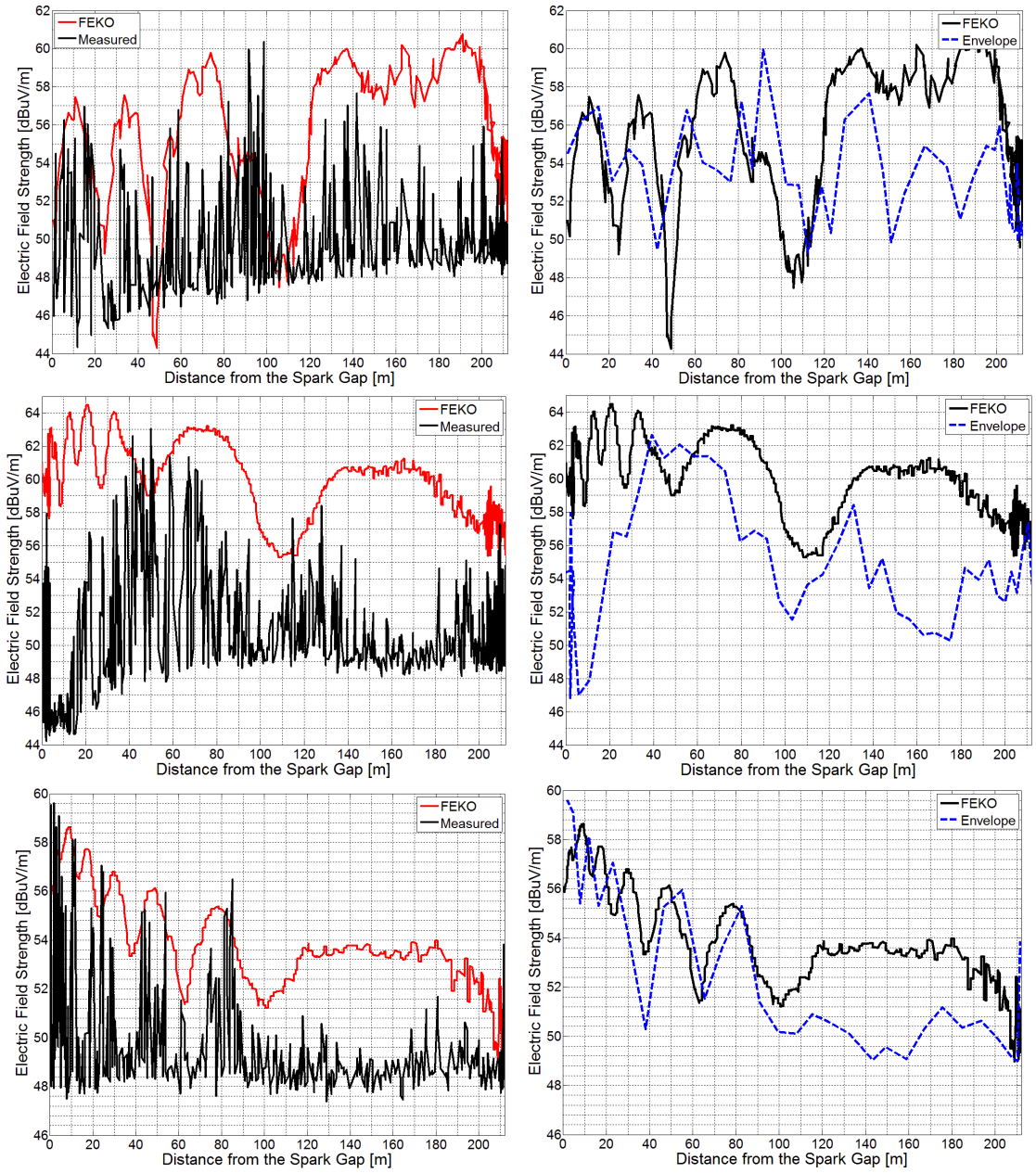

Figure 5.39: The measured and simulated sparking profiles are compared for flight 2: grid line 1 (top), grid line 3 (middle) and grid line 4 (bottom).

Better correlation was achieved with the imported flight paths without needing to shift the data along the power line's axis. Although the model cannot provide precise predictions of the sparking profile, the features are mostly similar. Flight 1, grid line 3, was the only measurement which did not show good correlation with the simulated electric field profile predictions.

The radiation pattern and filtering action of the line are of particular interest for OHTLs. The radiation action of the 22kV line is examined in FEKO in the next section.

5.8 Investigation of Power Line Radiation Characteristics

With the FEKO model offering good correlation with the aerial measurements, the simulations can be used to examine other effects. It was reported in [1] that power lines radiate as end-fire antennas.

The end-fire radiation pattern was checked in FEKO. Near-field requests were once again used to sample electric field values. The fields were sampled at the same height as the line (12.5m) with the spark gap generator as the centre of a radius equal to 1km (Figure 5.40).

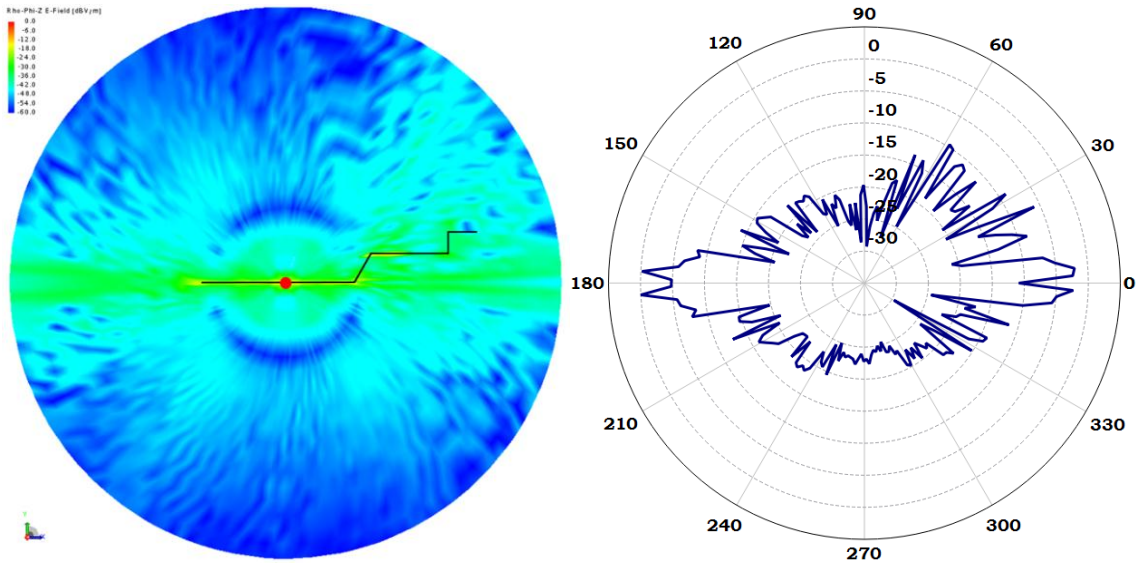

(a) (b)

Figure 5.40: (a) A visual grid of the near-field values of the OHTL radiation and (b) the polar plot of the field values sampled at a radius of 1km from the spark gap.

The bends in the line introduce a scattered effect in their direction. The sparking source was moved to examine the same effect (Figure 5.41).

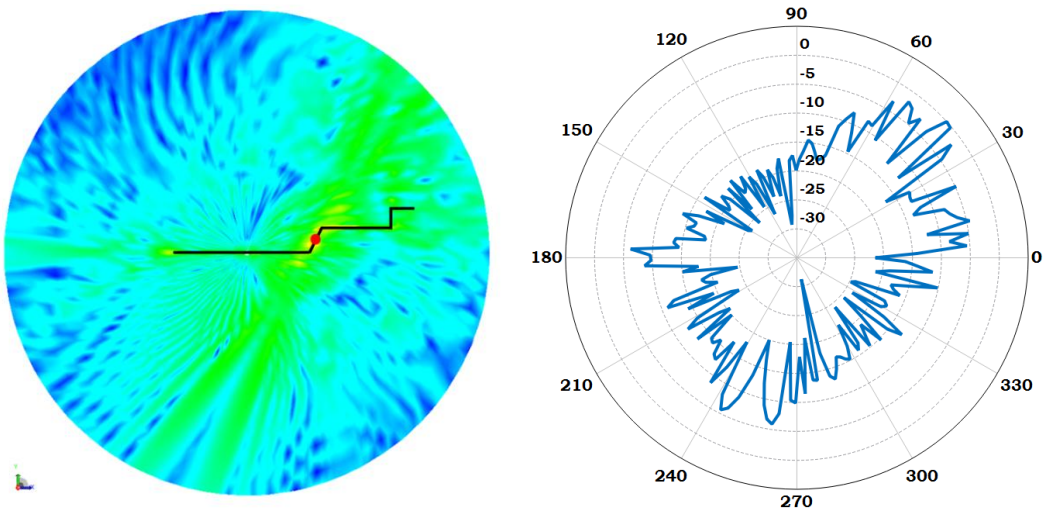

(a) (b)

Figure 5.41: The (a) polar near-field plot at a height of 12.5m, and (b) its corresponding polar plot 1km from the original sparking source at 239MHz. Both plots are normalised on a dB scale.

The radiation is once again in the direction of the line segment (120m in length) where the sparking has initiated. At this frequency, only 12.55m is required to radiate in the lines axis. Figures 5.40 and 5.41 prove that the line radiates in end-fire mode.

Normalised far field plots are shown in Figure 5.42 for the spark gap in the same position as in Figure 5.40 at 30MHz and 239MHz.

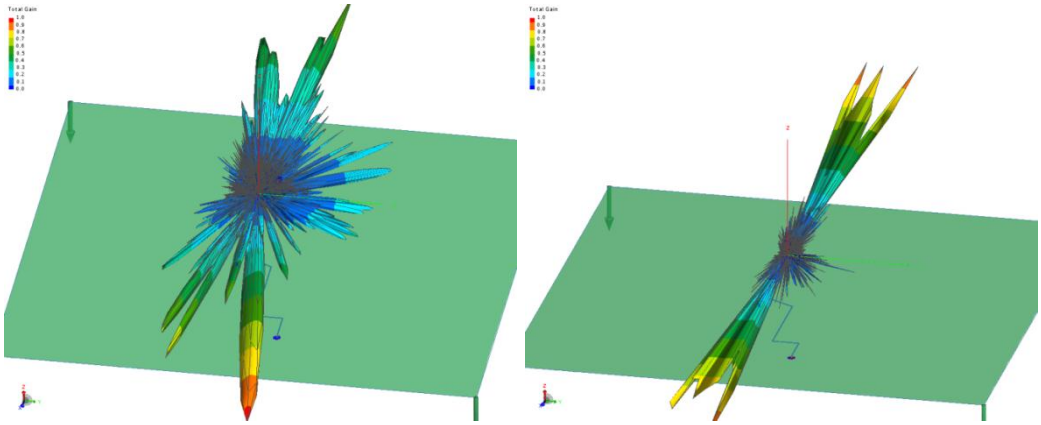

(a) (b)

Figure 5.42: Normalised far field plots of OHTL radiation at (a) 30MHz and (b) 239MHz.

Figure 5.42 shows how the lines radiate at different frequencies. The end-fire pattern is more directive in Figure 5.42(b) as energy radiates off of the line faster. The energy requires a longer length of line to radiate at 30MHz. The result is that the end-fire pattern is steered with the bends in the line.

5.9 Conclusions and Recommendations

In this Chapter, aerial sparking measurements were described. The challenges facing such a measurement were investigated and important findings are documented.

The first attempt at the measurements failed because of various factors. EMC issues, the measurement systems sensitivity, and the optimal SA settings were investigated and solved before the next measurement campaign. This lead to the comments made in Appendix B regarding good EMC practices for UAVs.

It is recommended that a broadband antenna be used for measurements of this kind. Resistively-loaded antennas (Appendix D) are suggested for these measurements for their small size, broad bandwidth and wide beam width. The SA should sample discrete points of interest instead of sweeping. Not only will this gather more information at the frequencies of interest, the individual narrow bands being sampled will result in more dynamic range. A good low-noise amplifier can be used in instances when sensitivity is an issue.

The second, successful measurement series yielded usable data which was corrected for the antenna factor as a function of position. The resulting electric field profile was compared to a MOM CEM solution. FEKO was used to predict the near-field sparking profile for these comparisons. The large-scale CEM solution was possible by making use of Babbage, Stellenbosch University's computer cluster.

Although the CEM solution cannot be used to derive an exact field profile (due to the complexity of the environment), it was shown to be relatively accurate. The CEM model can be used to examine the radiation action of the Klerefontein power

line. The end-fire radiation claim [1] was examined through simulations with the sparking source at various positions and the same conclusion was drawn.

5.10 References

[1] P Kibet-Langat, "Power line Sparking noise Characterisation in the SKA Environment", Ph.D dissertation, Dept. Elect. Eng., Stellenbosch University, Stellenbosch, December 2011.

[2] [Online]. Available: Rafael Fernandes de Oliveira, KML Toolbox v2.7, http://www.mathworks.com/matlabcentral/fileexchange/34694-kml-toolbox-v2-7/content/kmltoolbox%20v2.71/@kml/kml.m, Last visited September 2013.

[3] [Online]. Available: Weather Almanac for Vanwyksvlei, http://www.wunderground.com/history/wmo/68524/2013/ 8/15/Daily History.html, Last visited September 2013.

Chapter 6

Conclusions and Recommendations for Future Work

The focus of this thesis was to consider MADs and to study the radiation characteristics of OHTLs.

In Chapter 2, a theoretical study of the aspects affecting the MADs was done. These principles were instrumental in formulating a measurement strategy, and in the analysis of the results, in Chapter 3.

The empirical models (Gallet, CRIEPI and Rizk) predict the dielectric strength of air at STP for a rod-plane electrode configuration. These formulas are the basis for the IEC, IEEE and MHADs which are formulated for general scenarios described in Chapter 2.

International standards were examined to determine the existing methods used to determine safe approach distances for live-line work. The IEC (with no defective insulators) and IEEE predictions (Table 6.1) of safe approach distances were compared to analytical predictions and measurements.

OHTL [kV]	IEC LG	IEEE LG	IEEE MHAD	IEEE LL
132	1.4	0.8	1.32	1.4
400	4	3.5	4.44	7.1

Table 6.1: A comparison of the worst-case MAID predictions from international standards.

These vales give an idea of air's insulation strength for worst-case scenarios. To determine UAV-specific MAIDs, HV experiments and Rizk's equations are used.

In Chapter 3, HV tests were done to determine the MADs. Full-scale model testing is required to determine air's insulation strength for the UAV-conductor air gap. Constraints on equipment resulted in the focus of the tests being solely on the UAV in a HV tower window. Further HV testing requires a Marx bank generator capable of producing higher output voltages, a wide range of HV resistors and capacitors for wave shaping, as well as sufficient clearances in which to do the experiments.

The tests were done for both AC and switching impulses in accordance with the IEC standards for a 132kV tower window. The tests showed that, at AC, the line will never flash over to the UAV. Streamers will, however bridge the air gap within approximately 11cm. A switching impulse, however, will induce flashover for the test-model UAV at any position in the cage.

The HV test results were compared to analytical predictions in Chapter 4. The capability of FEKO in determining a geometric factor was verified, and appropriate critical electric field values were determined. Good correlation between the results allowed for extension of the model to other cases.

Rizk's equations are based on empirical data. Accurate predictions of air's insulation strength can therefore be made with the knowledge of the critical electric field gradient and the electrode configuration gap factor. The conductor-UAV geometric factor was determined using FEKO.

Rizk's analytical predictions are used to determine MAIDs for the UAV model alongside OHTLs in Table 6.2.

T [p.u.]	**132kV**	**400kV**
1	0.45 m	1.2 m
1.5	0.65 m	1.85 m
2	0.85 m	2.7 m
2.5	0.97 m	3.7 m
3	1.22 m	5 m
3.5	1.4 m	7 m

Table 6.2: The MAIDs for the Astec Firefly alongside OHTLs phase conductors using Rizk's equations.

OHTL phase-to-phase clearances for 132kV and 400kV lines are in the proximity of 1.4m and 3.6m respectively (Table 2.1). It is clear from Table 6.2 that a UAV will always be at risk between phase conductors of an OHTL.

The analytical predictions in Table 6.2 are compared to the standards in a graphical form in Figure 6.1.

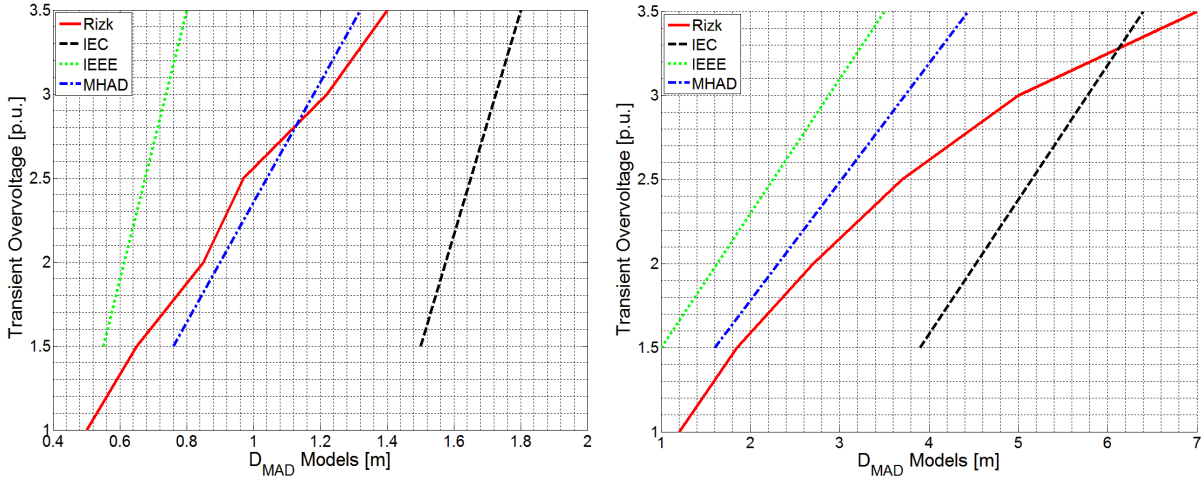

Figure 6.1: The comparison between the standards suggested MAIDs and the analytical predictions specific to the Astec Firefly for a (a) 132kV OHTL and (b) 400kV OHTL.

The IEEE MHAD predictions are very similar to Rizk's predictions for the UAV model. The IEC prediction for 50% defective insulators is plotted.

The form of the data in Figure 6.1 allows the utility to select safe-fly zones according to existing line data. For example, if the maximum recorded T = 1.6p.u. for a 132kV transmission line, it is safe to assume that 0.8m is the MAID for the UAV (according to Rizk's predictions).

It is left to the user to determine an appropriate safety factor based on weather conditions, ability of the UAV to stick to flight paths and so on. There is scope to test these equations and standards for the specific geometry (UAV size) with full-scale HV experiments.

In Chapter 5, the sparking-induced radiation of a 22kV, 1.5km transmission line was measured with a UAV system. The sparking measurements were taken with a narrow band stub antenna and a SA sweeping over the antenna's operating band.

It is suggested that, in future tests, a resistively-loaded antenna (designed in Appendix D) be used with a SA which jumps to pre-defined narrow band sample frequencies. This would result in multiple frequency points with more dynamic range at each frequency point of interest. The resistively-loaded antennas are broadband and have a broad 3dB beam-width, which allows the sparking to be easily detected in any position.

The near-field sparking profile was compared to a MOM CEM solution in FEKO. The simulated results show good correlation with the measured sparking profile. The proven FEKO model is used to examine the radiation characteristics of the Klerefontein OHTL. It is evident that the OHTL radiates in end-fire mode, and becomes more directive with an increase in frequency.

EMC considerations and improved sensitivity of the measurement system (can be improved by adding an LNA) are imperative if polar measurements at distances greater than approximately 120m are planned for a 22kV line. EMC principles were discussed in Appendix B.

It is recommended that sparking measurements on longer, higher voltage lines be done to determine the general radiation characteristic, as well as the effect of bends in the power line. Radiation from OHTLs with metallic towers will look different to the measured 22kV line with wooden pole supports. Areas still needing to be investigated through aerial measurements include: confirmation of the end–fire radiation pattern; the elevation angle of the radiated power.

Appendix A

Switching Impulse Testing - Data Collection and Interpretation.

Breakdown events, as explained in Chapter 2, are statistical phenomena. To adequately describe the behaviour of air dielectric breakdown, it must be described in terms of probabilities.

This Appendix deals with the measurement approach, the gathering procedures, the analysis and the correction of the data.

A.1 Impulse Test Results – Data Gathering.

Flashes are recorded as ticks as breakdown occurs mostly on the rising edge of the impulse and this is not a true reflection of the injected voltage. No flashes are recorded as the impulse peak values to check the injected pulse is in the proximity of the intended peak value. The test points are sampled for the entire primary gap, d_1 (Figure A1).

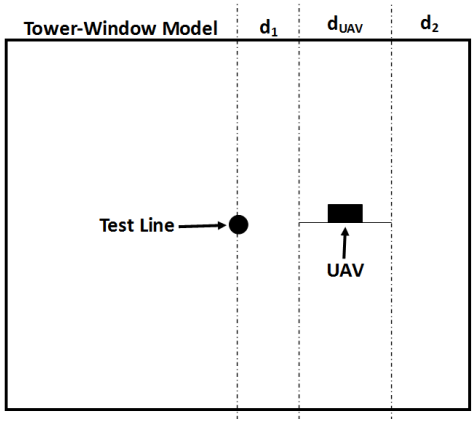

Figure A1: The UAV position relative to the test line in the grounded cage (tower window model) as a function of the primary gap, d_1.

The data gathered in the testing is separated into the different test days to isolate the temperature and pressure of the day.

A.1.1 Test day 1 – 03/04/2013

The temperatures recorded at the time of testing were:

- T = 21.5°C
- P = 758mmHg
- RAD = 0.9923 (from Equation A.2).

The primary gap, d_1, was selected as 21.7 cm. The test data is recorded in Table A1.

212kV$_{pk}$ (89)		**217.5kV$_{pk}$ (91)**		**223kV$_{pk}$ (90)**		**195kV$_{pk}$ (85)**		**202kV$_{pk}$ (87.5)**	
Flash	**No Flash**	**Flash**	**No Flash**	**Flash**	**No Flash**	**Flash**	**No Flash**	**Flash**	**No Flash**
✓	✓*	✓	218	✓			197		203
✓	✓*	✓	217	✓			194		202
✓	✓*	✓	212	✓			195		201
✓	✓*	✓	223	✓			196		204
✓	211	✓	222	✓			192		203
✓	209	✓	217	✓			194		207
✓	212	✓	213.5	✓			195		203
✓	220	✓					197		204
	213	✓					194		202
	209	✓					195		206
	212	✓					197		202
		✓					192		201
		✓					194		201
		✓					196		
		✓					193		
		✓							
		✓							
		✓							
		✓							

Table A1: The switching impulse data gathered for the primary gap equal to 21.7cm. The charging voltage is indicated in brackets alongside the average injected impulse peak.* - *Missed the reading – Oscilloscope didn't trigger.*

The probabilities of breakdown for the impulse testing - with a primary gap of 21.7cm - was determined as:

- P(Breakdown @ 212kV$_{pk}$) = 42%
- P(Breakdown @ 217.5kV$_{pk}$) = 73%
- P(Breakdown @ 223kV$_{pk}$) = 100% Suspect…
- P(Breakdown @ 195kV$_{pk}$) = 0%
- P(Breakdown @ 202kV$_{pk}$) = 0%

Plotting these values on normal probability paper yields a V_{50} of 214kV and a standard deviation of 5.5kV.

The next primary gap, d_1, was selected as 14.9 cm. The test data is recorded in Table A2.

194kV$_{pk}$ (85)		**199kV$_{pk}$ (87)**		**194kV$_{pk}$ (86)**	
Flash	**No Flash**	**Flash**	**No Flash**	**Flash**	**No Flash**
✓	197	✓	199	✓	189
✓	193	✓		✓	190
✓	196	✓		✓	196
✓	193	✓		✓	196
✓	194	✓		✓	195
✓	190	✓		✓	194
✓	190	✓		✓	195
	195	✓		✓	195
	196	✓		✓	196
	194	✓		✓	195
	195	✓			
	194	✓			
	191				

Table A2: The switching impulse data gathered for the primary gap equal to 14.9cm. The charging voltage is indicated in brackets alongside the average injected impulse peak.

The probabilities of breakdown for the impulse testing - with a primary gap of 21.7cm - were determined as:

- P(Breakdown @ 194kV$_{pk}$) = 35%
- P(Breakdown @ 199kV$_{pk}$) = 90%
- P(Breakdown @ 194kV$_{pk}$) = 50%

It can be seen that a small variation in the injected impulse peak results in a large variation in the probability of flashover. There is a very small transition region where the probability of breakdown changes from a definite insulation withstand to a definite flashover for small gaps. This means that the standard deviation for small gaps is very small. The insensitivity of the testing method (1kV change in charging voltage translates to a 5kV difference in impulse peak) and variability of the peak voltage due to the spark gaps in the machine makes it challenging to obtain a fine resolution for the testing voltages.

Plotting these values on normal probability paper yields a V_{50} of 214kV and a standard deviation of 4.15kV.

The next primary gap, d_1, was selected as 9.9 cm. The test data is recorded in Table A3.

194kV$_{pk}$ (85)		**182kV$_{pk}$ (82)**		**187kV$_{pk}$ (83)**		**191kV$_{pk}$ (84)**	
Flash	**No Flash**	**Flash**	**No Flash**	**Flash**	**No Flash**	**Flash**	**No Flash**
✓	185*		180		186	✓	190
✓			181		186	✓	192
✓			182		187	✓	191
✓			182		187	✓	194
✓			181		186	✓	190
✓			183		186	✓	190
✓			182		186	✓	191
✓			182		188	✓	
✓			182		186	✓	
✓			181		188	✓	
✓			182		188	✓	
✓			184		187		
✓					186		
✓					184		

Table A3: The switching impulse data gathered for the primary gap equal to 9.9cm. The charging voltage is indicated in brackets alongside the average injected impulse peak. * - *Same static charging voltage as previously – Know it should be 194kV$_{pk}$*

The probabilities of breakdown for the impulse testing - with a primary gap of 9.9cm - were determined as:

- P(Breakdown @ 194kV$_{pk}$) = 93%
- P(Breakdown @ 182kV$_{pk}$) = 0%
- P(Breakdown @ 187kV$_{pk}$) = 0%
- P(Breakdown @ 191kV$_{pk}$) = 61.11%

Plotting these values on normal probability paper yields a V_{50} of 191kV and a standard deviation of 1.3kV.

A.1.2 Test day 2 – 04/04/2013

The temperatures recorded at the time of testing were:

- T = 19°C
- P = 758mmHg
- RAD = 1 (from Equation A.2)

The primary gap, d_1, was selected as 6 cm. The test data is recorded in Table A4.

188kV$_{pk}$ (87)		**217kV$_{pk}$ (90)**		**192kV$_{pk}$ (88)**	
Flash	**No Flash**	**Flash**	**No Flash**	**Flash**	**No Flash**
	187	✓		✓	188
	186	✓		✓	191
	186	✓		✓	193
	186	✓		✓	194
	192	✓		✓	196
	190	✓		✓	196
	190	✓		✓	183

	188	✓		✓	186
		✓		✓	190
		✓		✓	202
				✓	185
				✓	190
				✓	

Table A4: The switching impulse data gathered for the primary gap equal to 6cm. The charging voltage is indicated in brackets alongside the average injected impulse peak.

The probabilities of breakdown for the impulse testing - with a primary gap of 6cm - were determined as:

- P(Breakdown @ 188kV$_{pk}$) = 0%
- P(Breakdown @ 217kV$_{pk}$) = 100%
- P(Breakdown @ 192kV$_{pk}$) = 52%

Plotting these values on normal probability paper yields a V_{50} of 192kV and a standard deviation of 1.3kV.

The next primary gap, d_1, was selected as 25.9 cm. The test data is recorded in Table A5.

218kV$_{pk}$ (95)		**213kV$_{pk}$ (93)**		**230kV$_{pk}$ (97)**	
Flash	**No Flash**	**Flash**	**No Flash**	**Flash**	**No Flash**
✓	216	✓	224	✓	232
✓	224	✓	213	✓	227
✓	216	✓	212	✓	226
✓	216	✓	210	✓	231
✓	218	✓	212	✓	225
✓	216	✓	210	✓	248
	218	✓	210	✓	224
	217		215	✓	
	218		212	✓	
			212		
			220		
			207		
			210		

Table A5: The switching impulse data gathered for the primary gap equal to 25.9cm. The charging voltage is indicated in brackets alongside the average injected impulse peak.

The probabilities of breakdown for the impulse testing - with a primary gap of 25.9cm - were determined as:

- P(Breakdown @ 218kV$_{pk}$) = 40%
- P(Breakdown @ 213kV$_{pk}$) = 35%
- P(Breakdown @ 230kV$_{pk}$) = 56.25%

Plotting these values on normal probability paper yields a V_{50} of 226.6kV and a standard deviation of 34kV.

A.1.3 Test day 3 – 15/04/2013

The temperatures recorded at the time of testing were:

- T = 20°C
- P = 750mmHg
- RAD = 0.987 (from Equation A.2)

The primary gap, d_1, was selected as 32.2 cm. The test data is recorded in Table A6.

337kV$_{pk}$ (105)		**300kV$_{pk}$ (100)**		**263kV$_{pk}$ (95)**		**281kV$_{pk}$ (98)**	
Flash	**No Flash**	**Flash**	**No Flash**	**Flash**	**No Flash**	**Flash**	**No Flash**
✓	330	✓	291		265	✓	289
✓	338	✓	297		263	✓	281
✓	340	✓	300		259	✓	279
✓	337	✓	303		263	✓	281
✓		✓	308		270	✓	280
✓		✓	306		266	✓	282

✓		✓			264		284
✓		✓			263		281
✓		✓			263		285
✓		✓			267		
✓							

Table A6: The switching impulse data gathered for the primary gap equal to 32.2cm. The charging voltage is indicated in brackets alongside the average injected impulse peak.

The probabilities of breakdown for the impulse testing - with a primary gap of 6cm - were determined as:

- P(Breakdown @ 337kV$_{pk}$) = 73.3%
- P(Breakdown @ 300kV$_{pk}$) = 62.5%
- P(Breakdown @ 263kV$_{pk}$) = 0%
- P(Breakdown @ 281kV$_{pk}$) = 40%

Plotting these values on normal probability paper yields a V_{50} of 292.4kV and a standard deviation of 23.94kV.

A.1.4 Test day 4 – 17/04/2013

The temperatures recorded at the time of testing were:

- T = 18°C
- P = 746.5mmHg
- RAD = 0.989 (from Equation A.2)

The primary gap, d_1, was selected as 29.5 cm. The test data is recorded in Table A7.

250kV$_{pk}$ (95)		**290kV$_{pk}$ (100)**		**265kV$_{pk}$ (97)**	
Flash	**No Flash**	**Flash**	**No Flash**	**Flash**	**No Flash**
✓	248	✓	288	✓	254
✓	262	✓		✓	252
✓	252	✓		✓	252
✓	247	✓		✓	256

✓	254	✓		✓	265
✓	244	✓		✓	
	248	✓		✓	
	247	✓		✓	
		✓		✓	
				✓	

Table A7: The switching impulse data gathered for the primary gap equal to 29.5cm. The charging voltage is indicated in brackets alongside the average injected impulse peak.

The probabilities of breakdown for the impulse testing - with a primary gap of 6cm - were determined as:

- P(Breakdown @ 250kV$_{pk}$) = 43%
- P(Breakdown @ 290kV$_{pk}$) = 90%
- P(Breakdown @ 265kV$_{pk}$) = 67%

Plotting these values on normal probability paper yields a V_{50} of 254kV and a standard deviation of 24kV.

The next primary gap, d_1, was selected as 38.4 cm. The test data is recorded in Table A8.

330kV$_{pk}$ (107.5)		**358kV$_{pk}$ (110)**	
Flash	**No Flash**	**Flash**	**No Flash**
✓	321	✓	349
✓	347	✓	366
✓	331	✓	358
✓	335	✓	349
✓	326	✓	359
✓	326	✓	355
✓	331	✓	353
	320	✓	374
	320	✓	
	320	✓	
	325	✓	
	320	✓	
	318		

Table A8: The switching impulse data gathered for the primary gap equal to 38.4cm. The charging voltage is indicated in brackets alongside the average injected impulse peak.

The probabilities of breakdown for the impulse testing - with a primary gap of 38.4cm - were determined as:

- P(Breakdown @ 330kV$_{pk}$) = 30%
- P(Breakdown @ 358kV$_{pk}$) = 60%

Plotting these values on normal probability paper yields a V_{50} of 349kV and a standard deviation of 35kV.

A.1.5 Test day 5 – 18/04/2013

The temperatures recorded at the time of testing were:

- T = 17°C
- P = 756.5mmHg
- RAD = 1 (from Equation C.2)

The primary gap, d_1, was selected as 44.4 cm. The test data is recorded in Table A9.

320kV$_{pk}$ (106)		**340kV$_{pk}$ (110)**		**365kV$_{pk}$ (112.5)**		**390kV$_{pk}$ (115)**	
Flash	**No Flash**	**Flash**	**No Flash**	**Flash**	**No Flash**	**Flash**	**No Flash**
✓	321	✓	333	✓	381	✓	385
✓	316	✓	331	✓	362	✓	391
	309	✓	329	✓	362	✓	388
	322	✓	344	✓	360	✓	381
	322	✓	344	✓	371	✓	
	325		347	✓	366	✓	
	320		347		377	✓	
	316		337		377	✓	
	312		346			✓	
	308		350			✓	
	311					✓	
	311						
	311						

Table A9: The switching impulse data gathered for the primary gap equal to 44.4cm. The charging voltage is indicated in brackets alongside the average injected impulse peak.

The probabilities of breakdown for the impulse testing - with a primary gap of 44.4cm - were determined as:

- P(Breakdown @ 320kV$_{pk}$) = 13%
- P(Breakdown @ 340kV$_{pk}$) = 33%
- P(Breakdown @ 365kV$_{pk}$) = 43%
- P(Breakdown @ 390kV$_{pk}$) = 73%

Plotting these values on normal probability paper yields a V_{50} of 367kV and a standard deviation of 39.27kV.

A.2 System Efficiency

The system efficiency is vastly changed in the wave shaping process. This is due to the resistive losses incurred and the additional capacitance/inductance. The efficiency of the system configuration used in the testing in Chapter 3 can be found using Equation A.1 [3].

$$\eta = \frac{C_S}{C_S + C_B} \qquad [A.1]$$

The four-stage configuration used in the testing is displayed in Figure A2.

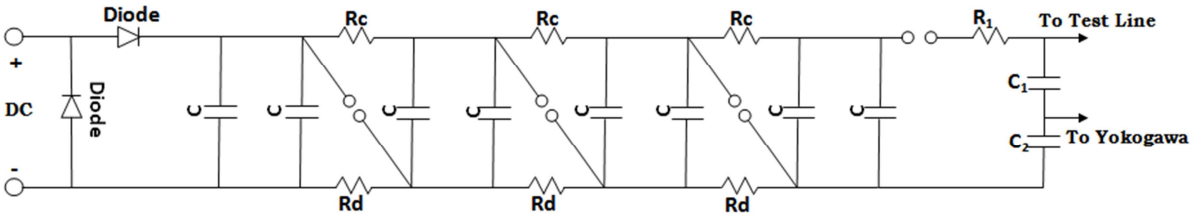

Figure A2: The system configuration used in the switching impulse testing to generate a 250/2500 μs wave.

The efficiency of the system during the measurements is plotted in Figure A3.

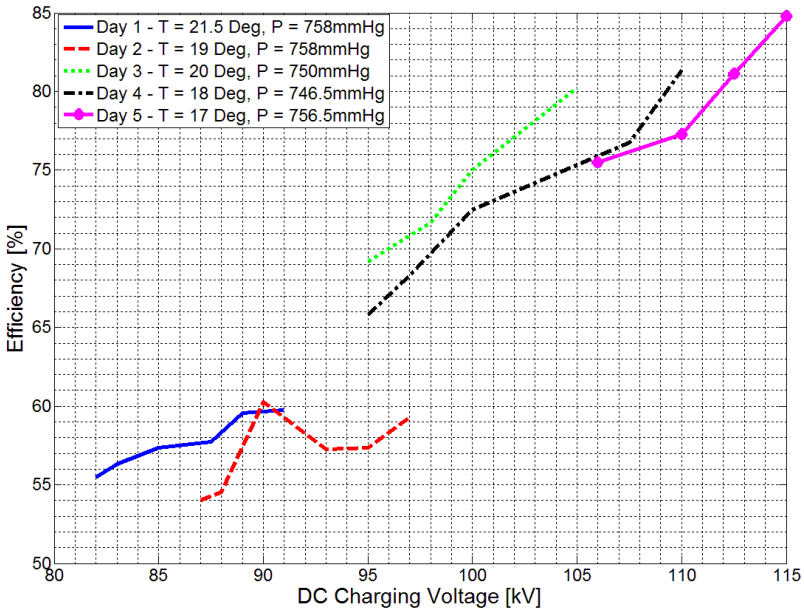

Figure A3: The efficiency of the system as a function of the charging voltage.

It can be seen from Figure A3 that the efficiency of the system is increasing with an increasing charging voltage. This does not affect the results – the only way it could is if this is the effect of the capacitive divider heating up. If this were the case, the efficiency would not be linear. Additionally, the charging voltages were not applied in increasing values, they were random. A lot of time passed between tests - used to set up the new distance d. This does not affect the results as the peak values were read off of the Yokogawa directly taken from the capacitive divider. The measurements also tied up with the analytical expressions. At some point (possibly

after day 2), the HV resistors in the Marx bank generator broke and were replace with bifilar winding resistors. They could also have different characteristics.

A.3 Normalising Data to Standard Temperature and Pressure

Results are normalised to standard temperature and pressure (STP) to standardise the results. The temperature and pressure were measured using a thermometer and barometer in the HV lab (Figure A4).

(a) (b)

Figure A4: The Thermometer (a) and Barometer (b) in the Stellenbosch University's High Voltage Laboratory to measure the temperature and pressure at the time of testing.

The correction factor is called the relative air density (RAD):

$$RAD = {}^{P}/_{760} \cdot {}^{293}/_{T} \qquad [A.2]$$

The measured temperature, T, and pressure, P, are inserted into A.2 to give the RAD correction factor. The corrected plot is shown in Figure A5.

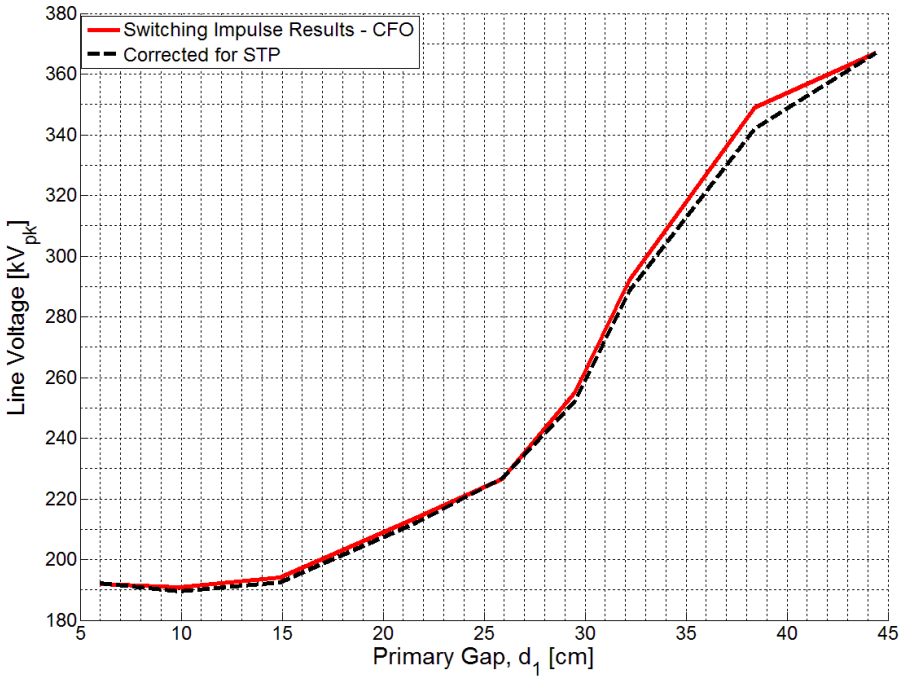

Figure A5: The switching impulse test results corrected for temperature and pressure.

The correction makes a small difference as most testing was done under conditions similar to STP.

A.4 Calibration of the Capacitive Dividers

In order to have confidence in the accuracy of the measurement equipment and setup, a comparison is made between the applied voltage and the capacitive dividers used in both the AC and impulse testing. The calibration setup is shown in Figure A6.

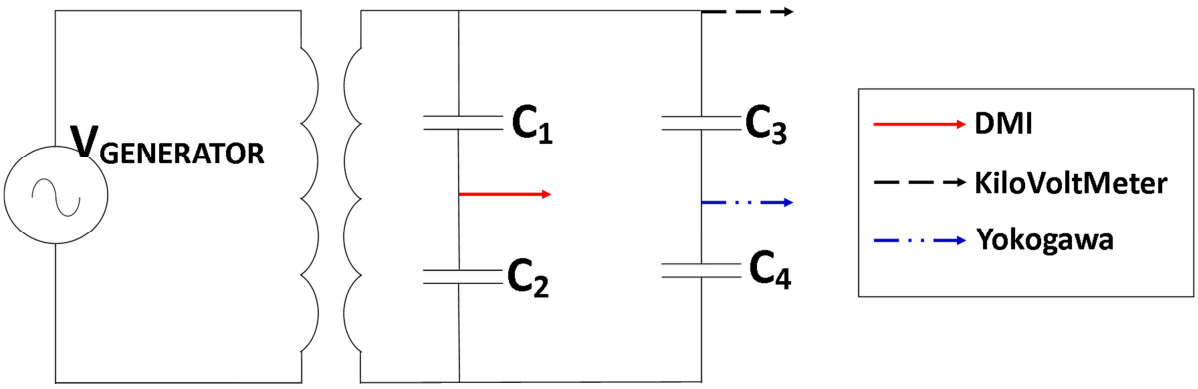

Figure A6: A schematic diagram showing the calibration setup.

The applied AC voltage is measured by the Digital Measurement Instrument (DMI) from Hipotronics through the AC capacitive divider (C_1, C_2). This applied voltage is compared to the capacitive divider (C_3, C_4) used for the impulse testing and the KiloVoltMeter reading of the applied voltage. The measurement instruments are depicted in Figure A7.

(a) (b) (c)

Figure A7: The DMI (a), KiloVoltMeter (b) and Yokogawa (c) measurement instruments used to compare divider networks.

To make up the impulse capacitive divider (C_3), a 2.5nF high voltage capacitor was connected in series with a 25µF (C_4) which was designed (Figure A8) by Petrus Pieterse.

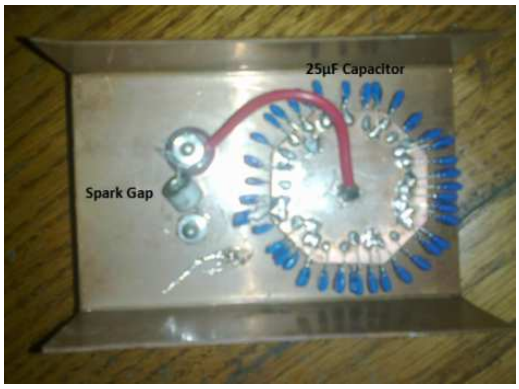

Figure A8: The 25µF low-inductance capacitor used as C_4 in Figure B1 – designed by Petrus Pieterse.

The calibration results are plotted as a comparative ratio against the DMI reading in Figure A9.

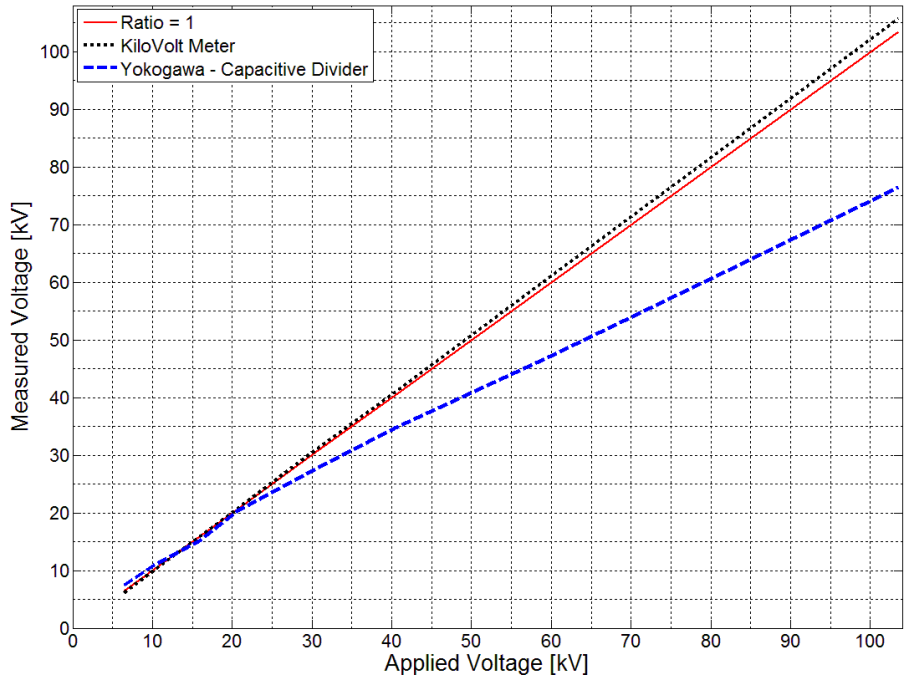

Figure A9: The calibration results plotted as a ratio against the DMI readings.

The AC capacitive divider aligns very well with the KiloVoltMeter readings, whereas the capacitive divider deviates with increasing AC voltage. The reason for the deviation is the fact that the designed capacitor, C_4, heats up with a sustained AC voltage. As the divider was used for impulse testing, no heat build-up will affect the

capacitance. Additionally, the impulse divider concurs well with the AC divider until 20kV. As the divider must be linear, the capacitive ratio (10,000:1) is taken to be constant with applied voltage.

A.5 References

[1] H Kirkham, "Applicability of the Gallet Equation to the Vegetation Clearances of NERC Reliability Standard FAC-003-2", US Department of Energy, April 2012.

[2] EPRI AC Transmission Line Reference Book – 200kV and Above, Third Edition. EPRI, Palo Alto, CA: 2005. 1011974.

[3] [Online]: Fachgebiet Hochspannungstechnik, Available: http://www.hst.tu-darmstadt.de/uploads/media/hvt1_v_04.pdf, Last visited September 2013.

Appendix B

Good EMC Practices for UAV Operation in Noisy Environments.

With the advent of UAVs and the improvements made in their control system architecture, UAV deployment is being considered in a wide array of industrial applications. Due to their typical make-up, UAVs are very susceptible to external interference. UAV operation in the proximity of HF sources is of particular concern for this project.

The reason for EMC shielding of a UAV is two-fold:

- High-powered, HF sources can potentially damage the on-board equipment and cause the UAV to crash.
- To make sensitive measurements without external interference, a well-shielded system is required to remove external influences.

In this Appendix, good EMC practices for UAV shielding will be discussed.

B.1 EMC Tools Required for UAV Shielding

To understand the principles surrounding effective EMC applications, fundamental EMC experiments are described.

The level of required shielding depends on the intended measurement environment. If the purpose is to shield for UAV activity in high-power environments where UAV malfunction is a worry, the entire system must be shielded. If the intention is to shield for sensitive measurements, everything barring the power distribution board, its power cables and motors needs to be shielded. The latter would save a lot of weight.

B.1.1 Twisted Pairs – The Three Wire Experiment to Demonstrate Resistive and Inductive Coupling of Loops

In a typical UAV, many wires are run through the heart of the vehicle in close proximity to one another and control, measurement and sensor boards. Long wires form loops which act as an antenna and receive any radiated signals in the environment. Additionally, components such as PWM (Pulse Width Modulators) induce spurious noise into the system. These noisy cables couple inductively to any unshielded cables in the vicinity, carrying the undesired spurious noise into the boards.

The inductive coupling between wires is shown in Figure B1.

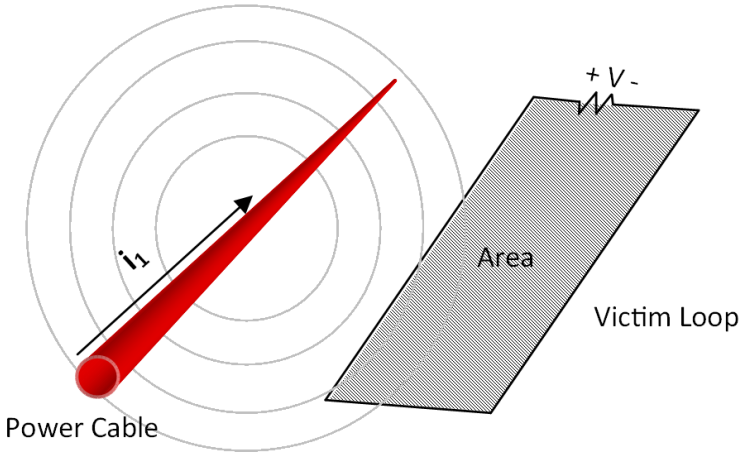

Figure B1: Inductive coupling between loops is dependent on the proximity, the area, and the impedance of the loops.

Figure B1 represents a noisy power cable coupling inductively to a large closed loop. The experiment was conducted with 2m long twin flex wire over a range of 1 – 100kHz. Coupling to the victim loop is presented as a function of increasing frequency in Figure B2.

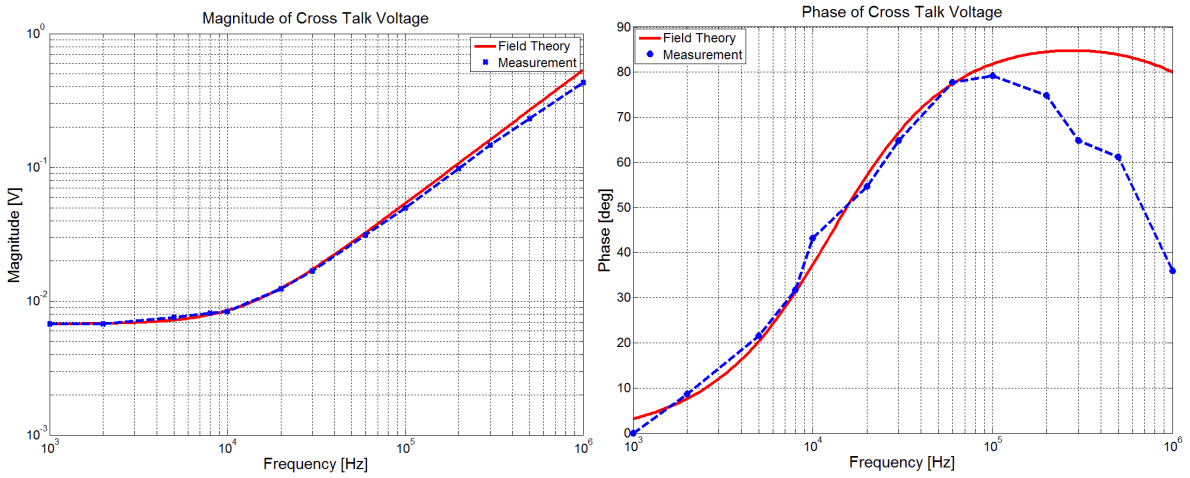

(a) (b)

Figure B2: The magnitude and phase of the coupling between loops in Figure D1 [2].

Figure B2 shows that resistive coupling is present until approximately 10kHz. Above 10kHz, coupling to the victim loop increases linearly.

To decrease inductive coupling to loops, the coupling area must be reduced. This can be done by keeping loop wires close together and near to the defined ground plane (Figure B3).

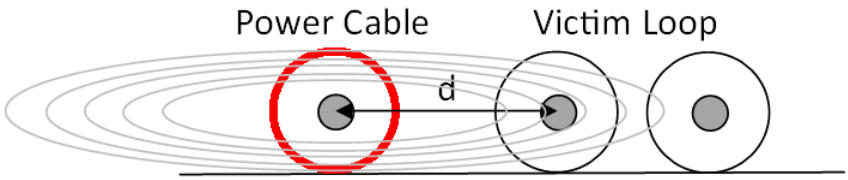

Figure B3: Keeping wires close to the ground plane reduces the coupling between loops.

Keeping wires close to the ground plane distorts magnetic field lines (B-Fields) such that the coupling field is weakened. A combination of twisting wires [3], and keeping loops small and close to a system ground plane will mitigate the majority of the coupling. This phenomenon is described in more detail by [2].

B.1.2 Using Cable Trays to Shield Wires and Electronics

Cable trays can be used to prevent inductive coupling to cables. Cable trays can be useful when a UAV makes use of external PCBs (Figure B4).

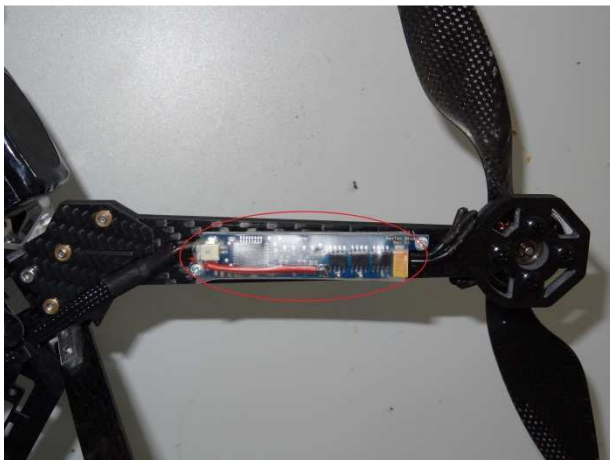

Figure B4: The positioning of external ESCs (Electronic Speed Controllers) can result in faulty operation in the proximity of high-powered, HF exposure.

In the event of high-powered HF radiation, unprotected components are at risk. Good examples of such events are switching surges on power-lines, nearby lightning strikes, and high powered transmitters – such as cell and broadcasting towers.

External boards as in Figure B4 can be difficult to shield as is external to the hull of the UAV and shielding can add unnecessary weight. It is a good idea to keep all electronics central in the body of the UAV.

An enclosure could be used to shield the external board with appropriate interface connections for the shielded wires to the motors. If payload capacity is an issue, the lighter cable tray could be used to shield the board and the cables to the UAV and motor.

Special care must be taken in the positioning of the cables in the cable tray. As magnetic fields bend around the end of the tray, “shadows” are created in the corners (Figure B5) [1]. The shadowed areas are particularly well-shielded EM regions.

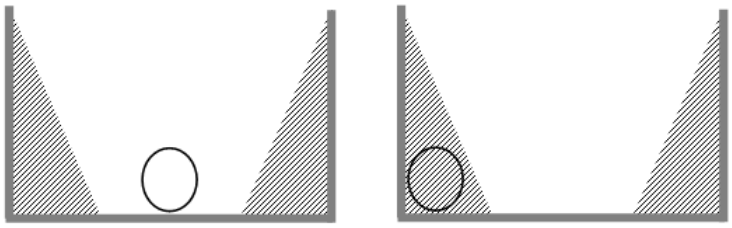

(a) (b)

Figure B5: The “shadow” created by the cable tray (b) is the best place to position cables for more effective shielding (after, [1]).

Because B-Fields form closed loops, a taller, thinner cable tray will result in lower coupling to victim loops. All cable trays should be well connected to the system ground [1]. Coax cable braiding should also be terminated at the ends of the cable tray.

B.1.3 Coaxial Cables – The Protective Braid’s Shielding Effect

Coaxial cables can be used for their shielding properties to reduce the amount of interference coupling into the system. Coaxial cables are surrounded by braiding for rigidity and shielding purposes.

Coaxial cables enable the designer to make use L-plates (described in B.1.4) and good terminations at enclosure interfaces. Additionally, coaxial cable braiding can be exposed and grounded at various points for long cables to reduce the size/area of pickup loops (Figure B6). Grounding the shield at multiple points reduces porpoising effects. Good connections are discussed briefly in section B.1.5.

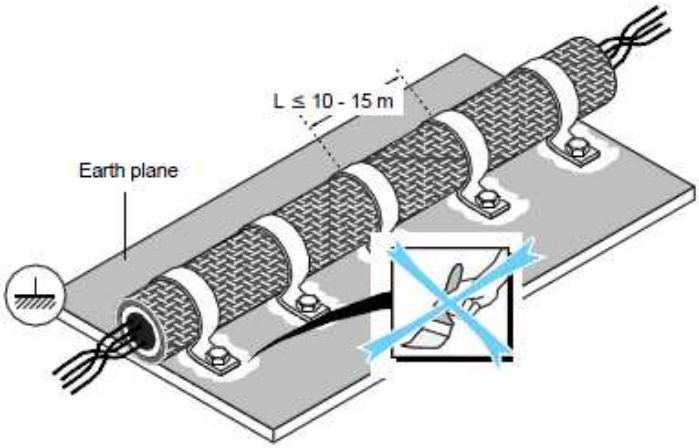

Figure B6: Equipotential bonding of coaxial cables ensures a common shield potential and reduces pickup area [1].

Various braiding schemes exist with different metallic conductors. The different braids exhibit different levels of shielding effectiveness. A few cables with different shields are shown in Figure B7 to demonstrate the effectiveness of various braiding methods and metals.

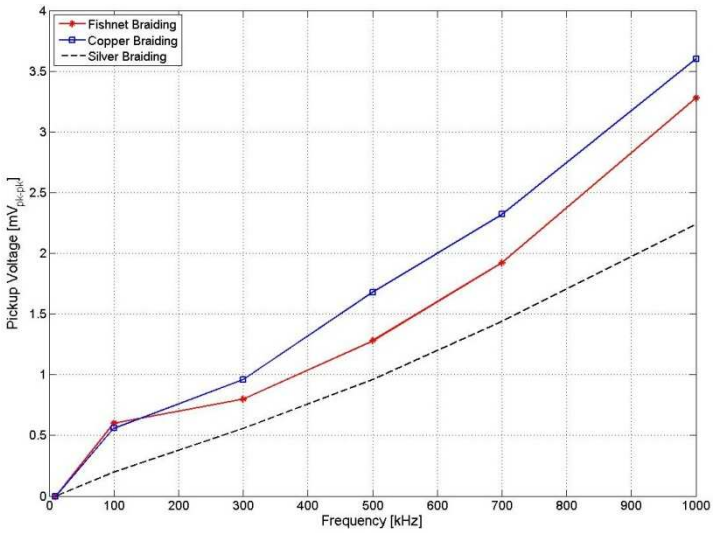

Figure B7: The transfer impedance of different coaxial cables [4].

This test shows the effective shielding (as a function of increasing frequency) of the different types of braiding with a $10V_{pk\text{-}pk}$ signal applied at the feed. Double braiding offers more shielding than single-braided cables.

Because shielded cables are not perfect, cables must be only as long as is required and deliberately routed in such a way as to pick up the least amount of coupling. This can be achieved by ensuring wires are never run parallel to one another.

Important cables can be replaced with semi-rigid or formable coaxial cables. Solid sheaths offer more protection than braided cables.

B.1.4 Interfaces – Using L-Plates to Divert Induced Currents

Coaxial cables have braided exteriors to shield the signal-carrying center conductor. Currents are induced on the surface of the braiding are then carried into connecting systems. To avert such a scenario, L-plates are used to divert the current by providing an easy return path back to ground (Figure B8).

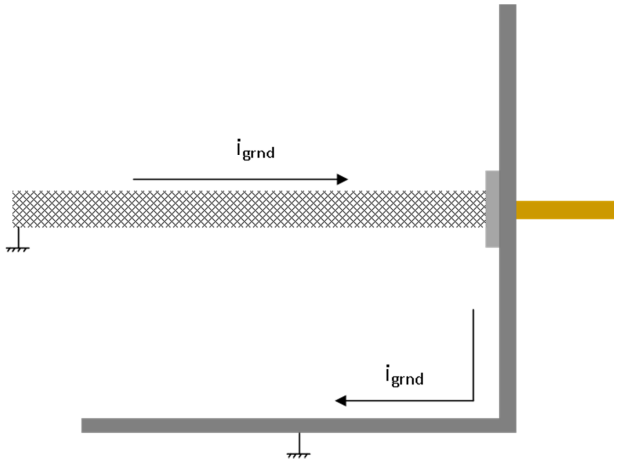

Figure B8: External currents travelling on a coaxial cable's braided exterior are diverted to ground by the L-plate interface.

Interface connections can be made through SMA barrels properly bolted to the earth plate. Feed-through capacitors and EMI filters can be used at the interconnections to remove out of band (unwanted) interference which has coupled to the center conductor.

B.1.5 Compartmentalising System Components

One of the most important considerations is that of a common ground. Keeping the UAV ground at a common potential with a well-defined system ground will reduce the necessary amount of ground wires. This will save weight and reduce the size of pickup loops thereby reducing coupling to the wires. A common ground will also make it possible to run wires close to the ground plane to reduce pickup areas.

Special attention must be paid to connection schemes. Braided straps should be used as an alternative to soldering wires for connections. The braided strap's length should be as short and wide as possible (Figure B9).

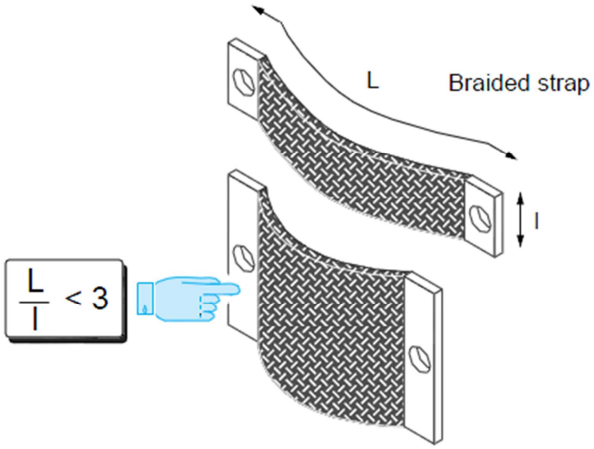

Figure B9: Short and wide braided straps should be used in all instances when making connections [1].

The architecture of a UAV allows a common ground to be used as a shield. System circuits can be divided into separate levels (compartmentalised) to isolate PCBs from one another.

Noisy boards and cables can be separated from sensitive components (the importance of this can be seen in section B.2.1). The noisy power distribution board and power cables must be isolated from control, sensor and measurement related cables and boards.

B.2 UAV Shielding Considerations for the Astec Firefly

A sample UAV from Ascending Technologies (Figure B10) was used to demonstrate EMC principles in the hardening of a typical UAV.

Figure B10: The Asctec Firefly was used as a sample UAV in the shielding investigation.

The Firefly supplied was in a simplified state with only the power distribution board and ESC circuitry. Dealing with the power cabling system and motors is, however, a good starting point.

Ideally, a UAV should be built with proper EMC practices in mind. This is however seldom the case and the systematic shielding procedure of an already-built system will be discussed. The shielding strategy is noted in bullet point form:

- Measure each cable's interference with a current probe and spectrum analyser with the UAV on and off.
- Measure the far-field radiation in an anechoic chamber – this is not essential.
- Measure the near-field emissions with the help of sniffer probes.
- Compartmentalise different electronic stages. Keep the power cables separate from the sensor boards and their cables through effective shielding techniques.
- A system ground must be well defined throughout the UAV.

- Take special care when making connections. Use short, wide, braided copper straps rather than cables.
- Important cables (measurements and sensor cables) can be shielded using coaxial or semi-rigid cables. L-plates can divert induced common mode currents on the shielding to the system ground to protect PCBs.
- Meshed enclosures can be used to protect boards, measurement systems and the GPS sensor from external interference.
- All wires must be kept as short as possible. All loops should form twisted pairs close to the system ground.
- Repeat steps to check shielding effectiveness until the system is well shielded.

The power cables were measured using a current probe and a spectrum analyser to determine the interference cause by the cables. In a typical UAV setup, the switching from the ESCs produces pulses which translate into a high level of interference.

B.2.1 Cable Interference Investigation

The power and control cables to the motor were measured using a current probe and a spectrum analyser, as in Figure B11.

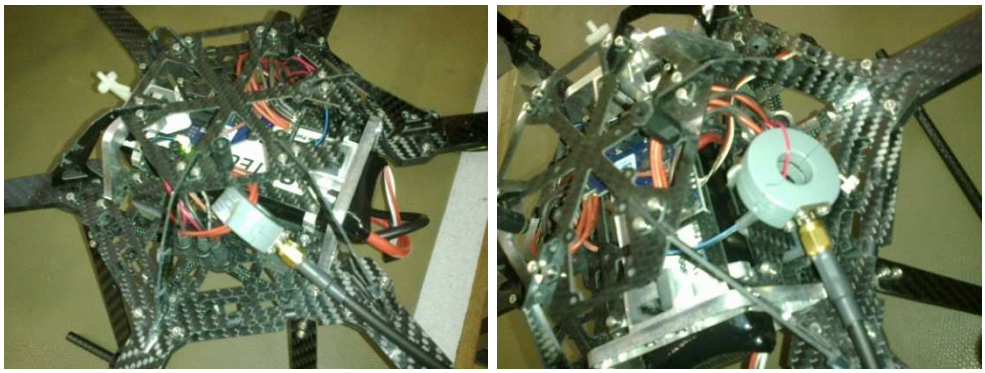

(a) (b)

Figure B11: A power cable (a) running from the power distribution board to an ESC and its corresponding control cable (b) were measured.

The power cables are of particular importance due to their close proximity to the sensor boards and high emission levels. Emitted interference could easily couple into the boards and cables to distort readings and affect their operation (GPS, gyroscope, etc.).

With the UAV on, the current probe measured the current spectrum as in Figure B12.

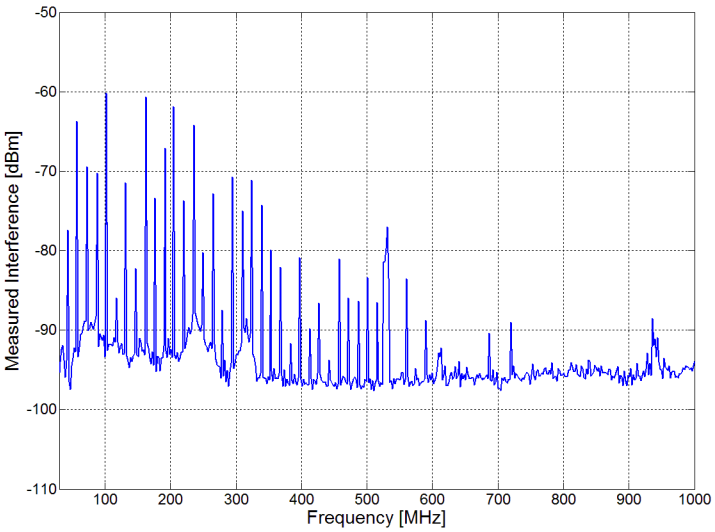

Figure B12: The measured interference on the power cable in Figure B11.

The measured power cable is carrying a very high level of interference. There is a clear need to separate the power cables from the rest of the cables and boards.

The control cable (Figure B11(b)) was measured with the UAV in an on and off state (Figure B13). This shows that the interference is self-generated.

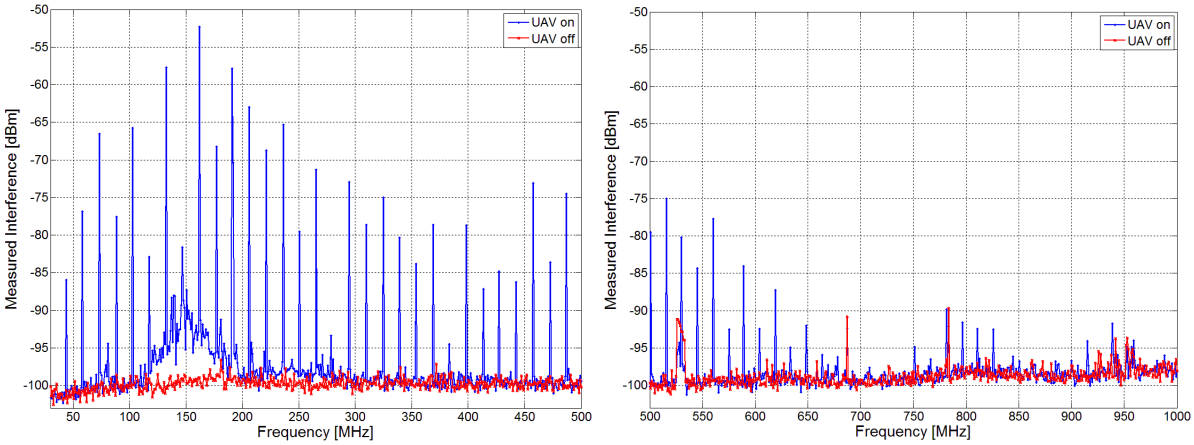

Figure B13: The measured control cable interference with the UAV in an on and off state.

A very similar characteristic can be seen when comparing the control and power cable measurements (Figure B14).

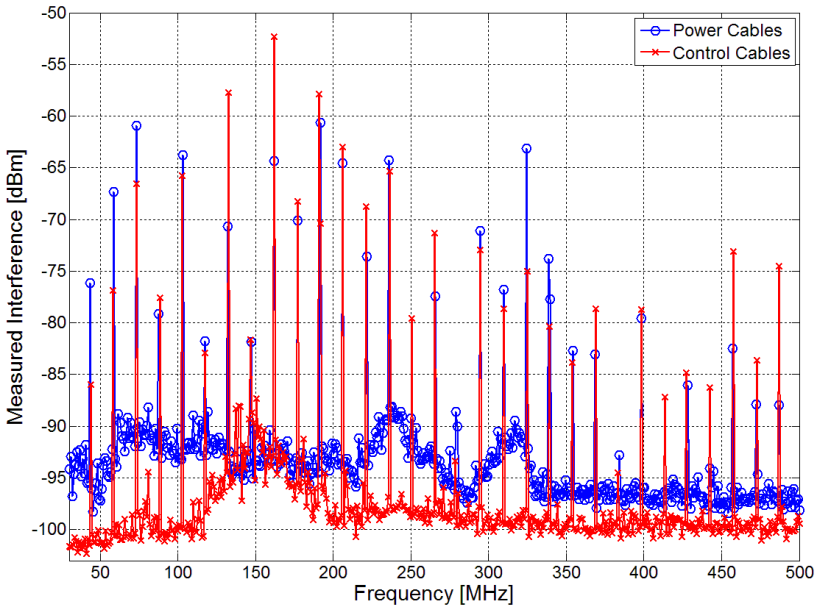

Figure B14: Comparing the control and power cable interference shows that all interference is common to both cables.

Figure B14 shows that the interference is common to both the power and control cables. This high level of coupling demonstrates the need to isolate the systems from one another as discussed in B.1.5.

B.3 References

[1] [Online]. Available: Groupe Schneider, "Electromagnetic Compatibility: Practical Installation Guidelines", https://www.google.co.za/?gws_rd=cr&ei=e909UqPzNOub0wXunoGoDQ#q=schneider+electronics+EMC&safe=off&spell=1, Last visited August 2013.

[2] Postgraduate EMC 813 course, given by Prof H.C. Reader, Topic: "The Twin Flex Wire Experiment", Dept. of EE Engineering, Stellenbosch, 2012.

[3] T.E.W Stewart, H.C. Reader, "Apparently Simple Low Frequency Measurements: An EMC View", IEEE/SAIEE Symposium on Communications and Signal Processing, COSMIG '98, Cape Town, Sept 1998, paper AP-19.

[4] Postgraduate EMC 813 course, given by Prof H.C. Reader, Topic: "Examination of the Transfer Impedance of Coaxial Cables", Dept. of EE Engineering, Stellenbosch, 2012.

Appendix C

The Post Processing of the Sparking Measurement Data

C.1 Deriving the Electric Field Profile

The typical steps taken in the processing of the sparking measurement data are described in this Appendix. To convert the measured data to electric field values, the Antenna Factor (AF) needs to be removed from the measured dBm values. To correct for the AF, the gain pattern of the antenna on the system is needed. A vertical and horizontal cut of the gain pattern is shown in Figure C1[1].

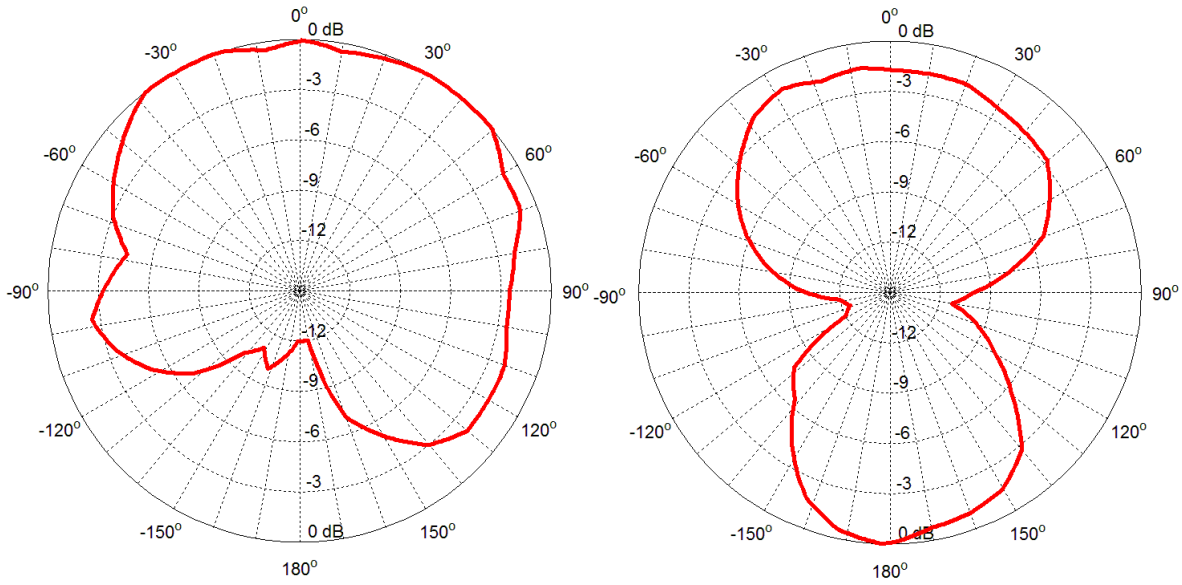

Figure C1: The Horizontal (a) and Vertical (b) cut of the antenna gain pattern on the UAV system at 216MHz.

The helical stub antenna used in the measurements was used at 239MHz. To determine the direction of the received power, the power line phase centre is assumed to be 5λ (10λ/2) from the spark gap. As explained in Section 5.6, this follows from the assumption that the power line radiates as an end-fire antenna [1].

[1] These measurements were carried out by Ls of SA (http://www.lsofsa.co.za/index.html).

The flight paths are broken up into grid lines as in Figure C2 [2] to determine the AF of the system in the direction of the received sparking radiation.

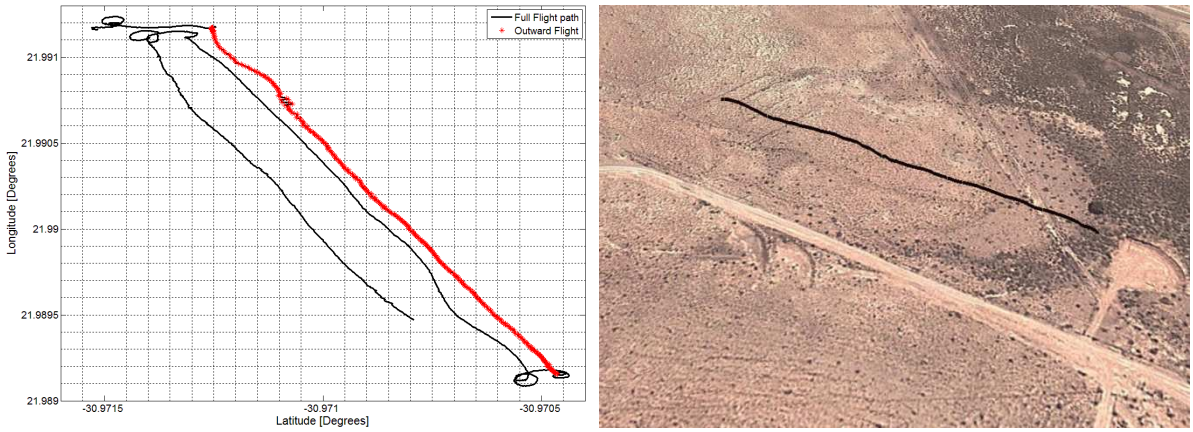

Figure C2: The flight paths are broken up into grid lines for processing.

The angle of the antenna relative to the power line's phase centre is determined by considering the geometry of the problem (Figure C3).

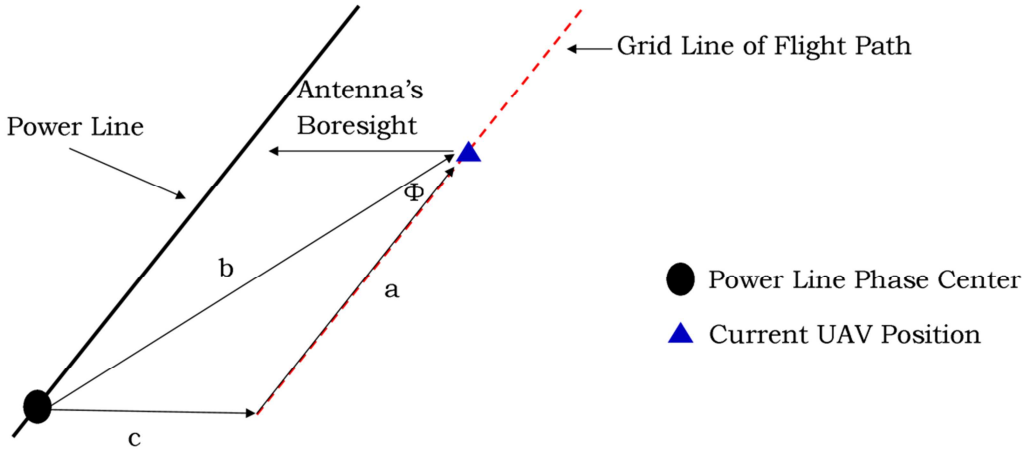

Figure C3: The geometry considered to calculate the position of the power line's phase centre relative to the antenna.

The flight log data is provided in GPS coordinates at each time stamp. To find the distance between two GPS coordinates (needed to determine a, b and c), the great circle formulation [3] is used.

$$CA = \arccos(\mathrm{Sin}(\mathrm{lat}_1) * \mathrm{Sin}(\mathrm{lat}_2) + \mathrm{Cos}(\mathrm{lat}_1) * \mathrm{Cos}(\mathrm{lat}_2) * \mathrm{Cos}(\mathrm{lon}_2 - \mathrm{lon}_1)) \qquad [C1]$$

The Central Angle, CA, is derived from the law of spherical cosines [3]. The distance between GPS coordinates is the radius of the earth multiplied by the CA [3]:

$$d = r * CA \qquad [C2]$$

Equation C2 gives the distance between two GPS coordinates at the same height in metres. The angle Phi in Figure C3 is determined from the distances a, b and c according to the cosine rule:

$$\Phi = \mathrm{Cos}^{-1}\left((a^2 + b^2 - c^2) / (2 * a * b)\right) \qquad [C3]$$

The distances a, b and c are plotted in Figure C4 as a function of the UAV's distance along the grid line. All distances are plotted moving away from the spark gap along the line.

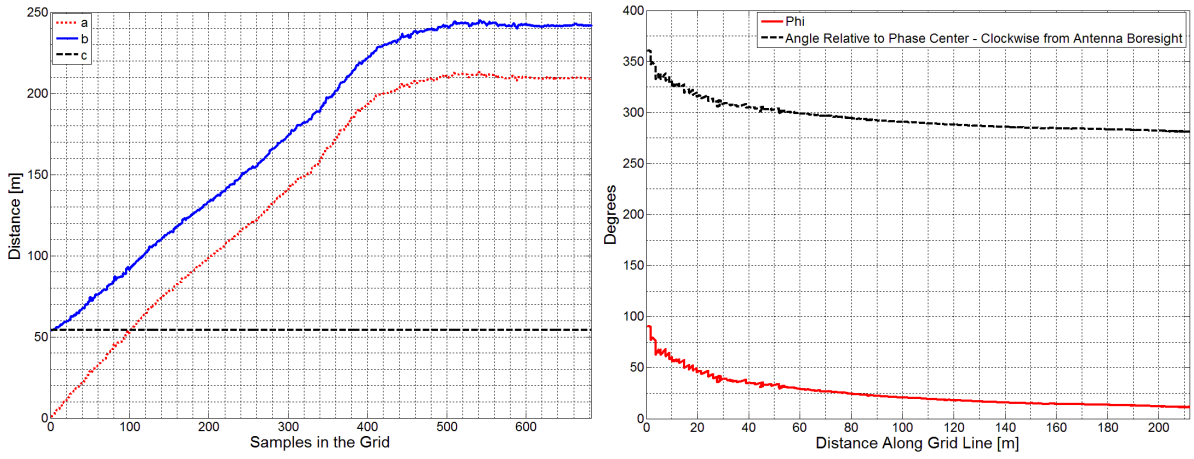

(a) (b)

Figure C4: (a) The distances a, b and c are used to determine (b) the angle as a function of position relative to the power line's phase centre.

The angle Phi (Figure C4(b)) is used to determine the gain of the system (from Figure C1) in the direction of the power line's phase centre. The gain is displayed in Figure C5 along with its corresponding AF.

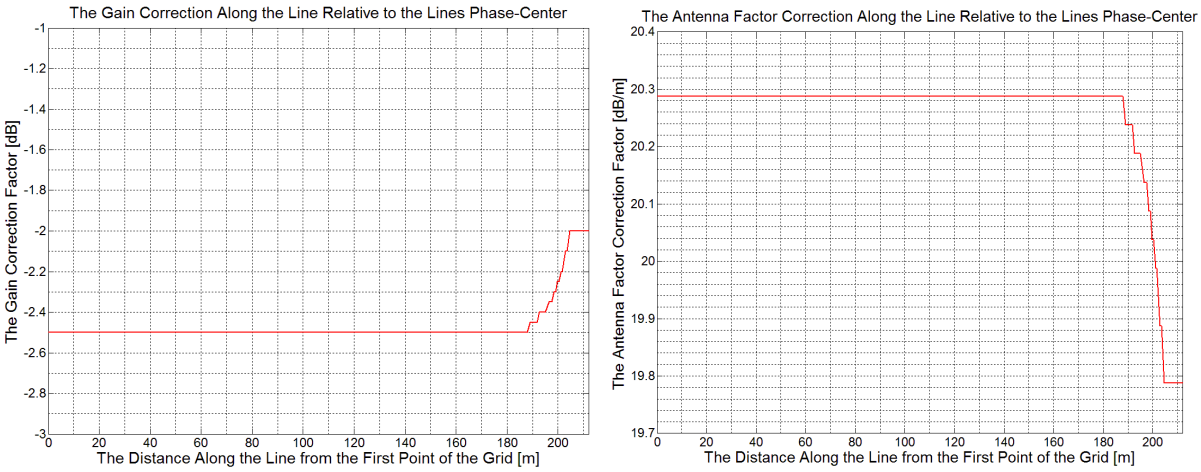

(a) (b)

Figure C5: The gain and corresponding antenna factor are shown as a function of distance away from the spark gap.

The gain of the antenna is converted to an AF using [4]:

$$\mathrm{AF} = 9.73/\left(\lambda\sqrt{\mathrm{G}}\right) \qquad [C4]$$

Once the AF is determined, it can be removed from the measured signal level, V to give electric field, E [4], [5]:

$$\mathrm{E} = \mathrm{V} + 107 + \mathrm{AF} \qquad [C5]$$

The electric field and its envelope at the sampled flight path are shown in Figure C6.

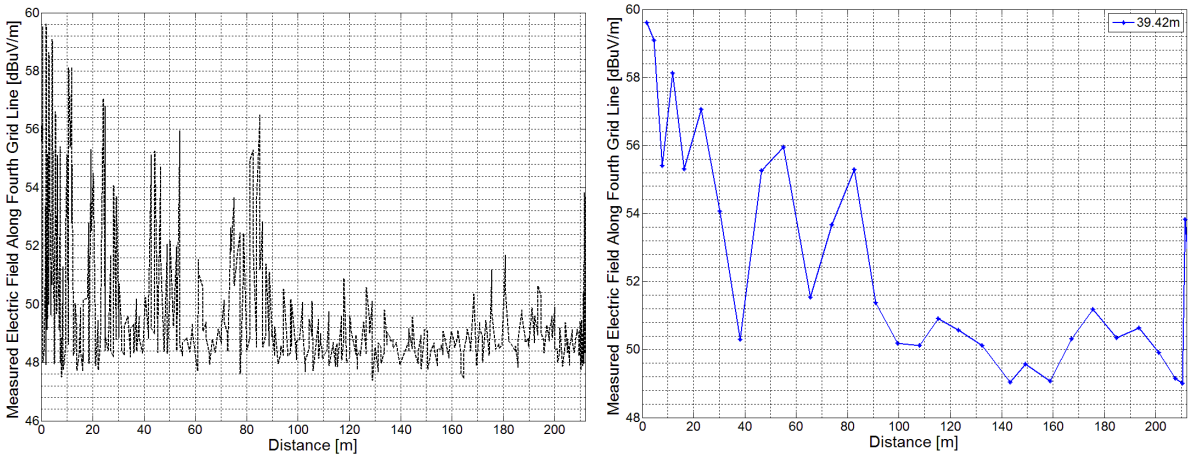

(a) (b)

Figure C6: The electric field (a) and its envelope (b) are shown for one grid line of a flight path.

This method was applied to all grid lines of the flight paths using MATLAB R2009a.

C.2 References

[1] C.A. Balanis, 'Antenna Theory Analysis and Design', John Wiley and Sons, 2006, New Jersey.

[2] [Online]. Available: Rafael Fernandes de Oliveira, KML Toolbox v2.7, http://www.mathworks.com/matlabcentral/fileexchange/34694-kml-toolbox-v2-7/content/kmltoolbox%20v2.71/@kml/kml.m, Last visited, August 2013.

[3] [Online]. Available: J.R. Clynch, "Paths Between Points on Earth: Great Circles, Deodesics, and Useful Projections", http://www.gmat.unsw.edu.au/snap/gps/clynch_pdfs/navpaths.pdf, Last visited August 2013.

[4] McLean J., Sutton R., and Hoffman R. 2002, 'Interpreting antenna performance parameters for EMC applications. Part 3: Antenna Factor', TDK RF Solutions Inc.

[5] P Kibet-Langat, "Power line Sparking noise Characterisation in the SKA Environment", Ph.D dissertation, Dept. Elect. Eng., Stellenbosch University, Stellenbosch, December 2011.

Appendix D

The Resistively-Loaded Monopole Antenna

The ideal antenna for aerial measurements is a small, broadband (lowest frequency possible) antenna with a large beam-width to ensure that the signal is received. The aerodynamic properties of the antenna also need to be considered due to the harsh environment involved in aerial measurements. Therefore, the antenna must also be light and offer little wind resistance.

The monopole (Figure D1) offers all of these characteristics, yet they are narrow-band as they operate as resonant antennas. To bypass the narrow-band characteristics, the antenna can be made active. Active antennas are risky in such an uncontrolled environment as strong signals can damage the on-board equipment. Another option is to sacrifice efficiency for broad bandwidth by resistively loading the antenna along its length.

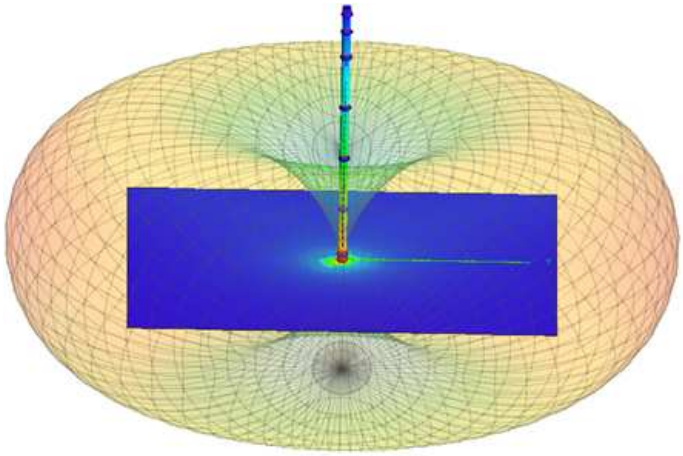

Figure D1: The far field pattern of a monopole in its operating band.

Three antennas were considered for their different bands of operation. A low frequency (50 cm) antenna, mid-frequency (25 cm) and high-frequency (12.5 cm)

antennas were designed and constructed for operation in the band indicated in Figure D1[1].

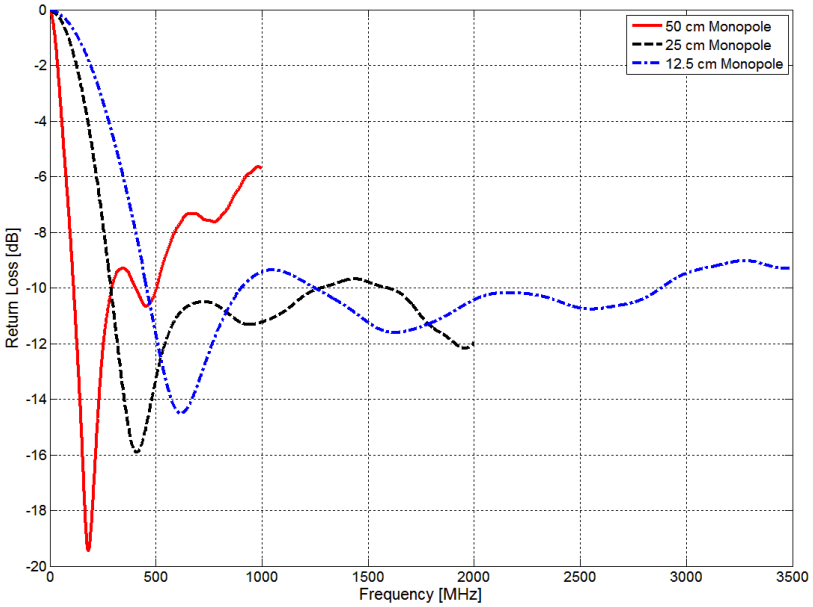

Figure D2: The three considered antennas return loss profiles as simulated in CST.

The high and low frequency antennas were deemed sufficient to cover the band from 30MHz to around 4GHz. A 20dB battery-driven pre-amplifier can be used to increase the sensitivity of the antenna.

To create a broadband monopole antenna, its characteristics need to be changed from a resonant, standing wave antenna to a non-resonant, travelling wave antenna. Resistive loading accomplishes this by damping internal and open-ended reflections by absorbing the reflected waves in the resistive elements. The Wu-King profile was used and adapted to design the antennas.

D.1 The Wu-King Profile

The Wu-King impedance profile per unit length, z, is determined along the total element length, h, from equation A1.

[1] With many thanks to Professor K.D. Palmer for his assistance in the design process.

$$z^{i}(z) = 15\psi/(h - |z|) \qquad [D1]$$

The expansion parameter, Ψ, is defined by:

$$\psi = 2\left[\sinh^{-1}\left(\frac{h}{a}\right) - C(2ka, 2kh) - jS(2ka, 2kh)\right] + \frac{1}{kh}\left(1 - e^{-j2kh}\right) \qquad [D2]$$

where a is the element radius, k is the free space wave number, and C and S are the generalised Sine and Cosine integrals in D3 and D4.

$$C(a, x) = \int_0^x \left(\frac{1 - \cos\left((u^2 + a^2)^{1/2}\right)}{(u^2 + a^2)^{1/2}}\right) du \qquad [D3]$$

$$S(a, x) = \int_0^x \left(\frac{1 - \sin\left(u^2 + a^2\right)^{1/2}}{(u^2 + a^2)^{1/2}}\right) du \qquad [D4]$$

The resistive loading profile was found by executing equations D1 through D4 in a MATLAB script.

```
%Resistively-loaded Profile
clc
clear all

a = 0.005;
u = 0:(0.2*pi/100):(0.2*pi);
i = numel(u);
h = 0.5;
j = 1;

while (j <= i)

    C(j) = ((1 - cos(sqrt((u(j)).^2+(0.042).^2)))/(sqrt((u(j)).^2+(0.042).^2)));
    S(j) = ((sin(sqrt((u(j)).^2+(0.042).^2)))/(sqrt((u(j)).^2+(0.042).^2)));
    j = j + 1;
end

Zc = trapz(u,C);
Zs = trapz(u,S);
A = asinh(h/a);
B = abs(-exp(-sqrt(-1)*pi*0.2));

Phi = (2 * (A - Zc - sqrt(-1) * Zs)) + (sqrt(-1)*2/(0.1*pi) * (1 + B));
```

```
i = 1;
Z = 0:(h/100):h;
j = numel(Z);

while(i <= j)

    z(i) = 0.1*(15 * Phi)/(h - abs(Z(i)));
    i = i + 1;

end

z0 = 15*Phi

plot(100*Z,z,'r','LineWidth',3)
grid on
hold on
plot(100*Z,z,'xk')
xlabel('Length [cm]', 'fontsize', 20)
ylabel('Resistance [Ohms]', 'fontsize', 20)
set((findobj('type','axes')),'fontsize',16)
```

Implementation of the equations in a MATLAB script results in a resistive profile as in Figure D3.

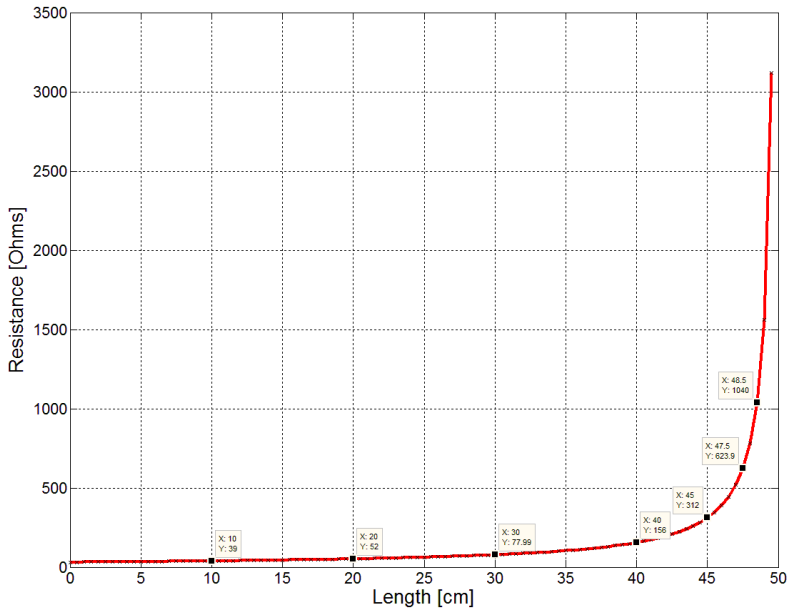

Figure D3: The WuKing impedance loading profile for a 50cm monopole element.

The exponential taper is then used to selected discrete points at which to place the lumped chip resistors.

D.2 Optimisation of the Antenna Designs Using Simulation Packages.

To optimise the loading profile, the antenna was designed in FEKO and CST (Figure D4). From here on in, the focus will be on the design of the 50cm monopole.

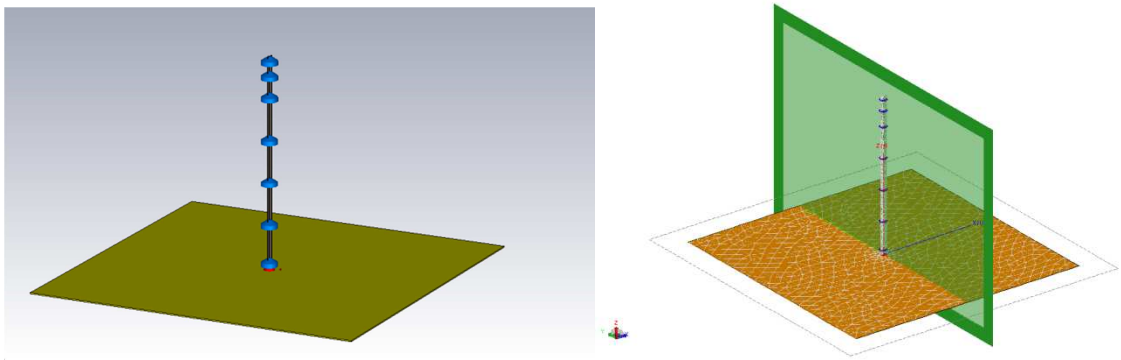

Figure D4: The respective CAD models of the antenna design in CST and FEKO.

Initially, line models were used in FEKO to save on runtime (Figure D5). This was proven to be accurate at low frequencies and is used to get an idea of the antenna's performance [2]. The FEKO line prediction method is compared to CST in Figure D5 to determine if the modelling is accurate.

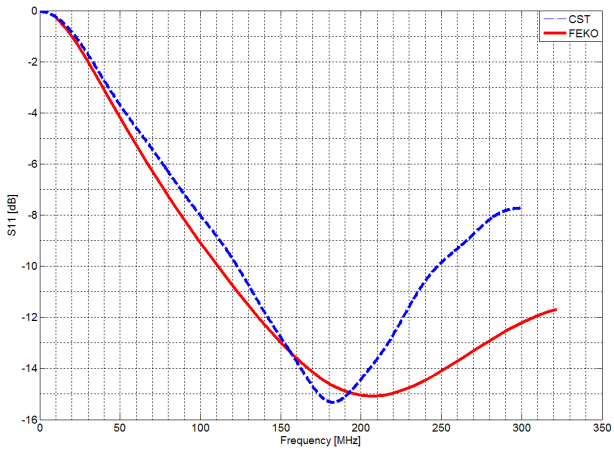

Figure D5: The 50cm resistively-loaded monopole's return loss as predicted by FEKO (using line elements) and CST.

A good correlation is achieved in the modelling up to around 200MHz. A substrate was implemented in FEKO (Figure D6) to ascertain whether FEKO could handle the problem and the runtime required in solving it.

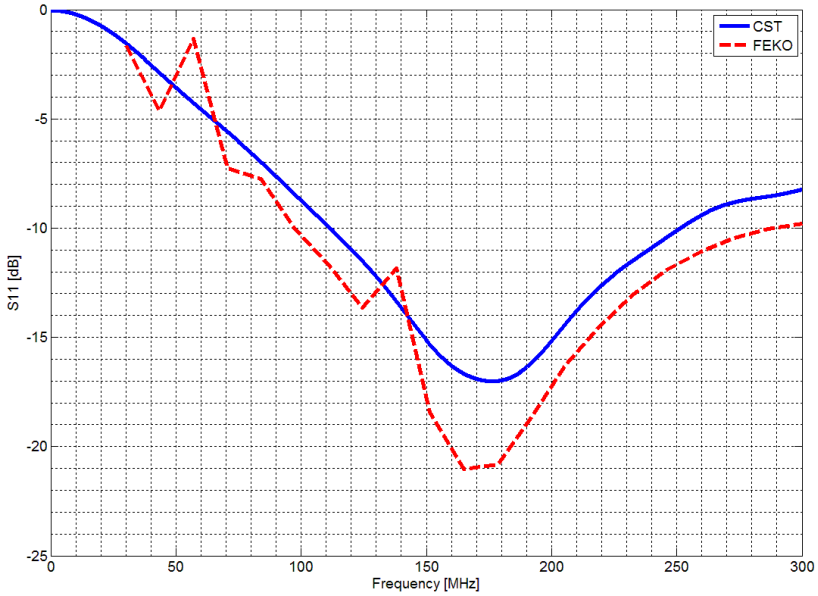

Figure D6: The 50cm resistively-loaded monopole's return loss as predicted by FEKO using a substrate model and CST.

CST is more suited to solving this problem as FEKO is not well suited to modelling substrate mediums. Additionally, CST's powerful parameter sweep and optimisation functionality allows for easy manipulation of the model. The CST model will be used from here on.

Before an impedance matching circuit is designed and tested, the manufactured antenna is tested against simulations to ensure that it has been properly constructed.

The simulated and measured return loss performance was compared for the 50cm monopole (Figure D7) in its unmatched state. The measurement was done using a calibrated Vector Network Analyser (VNA) in an open environment.

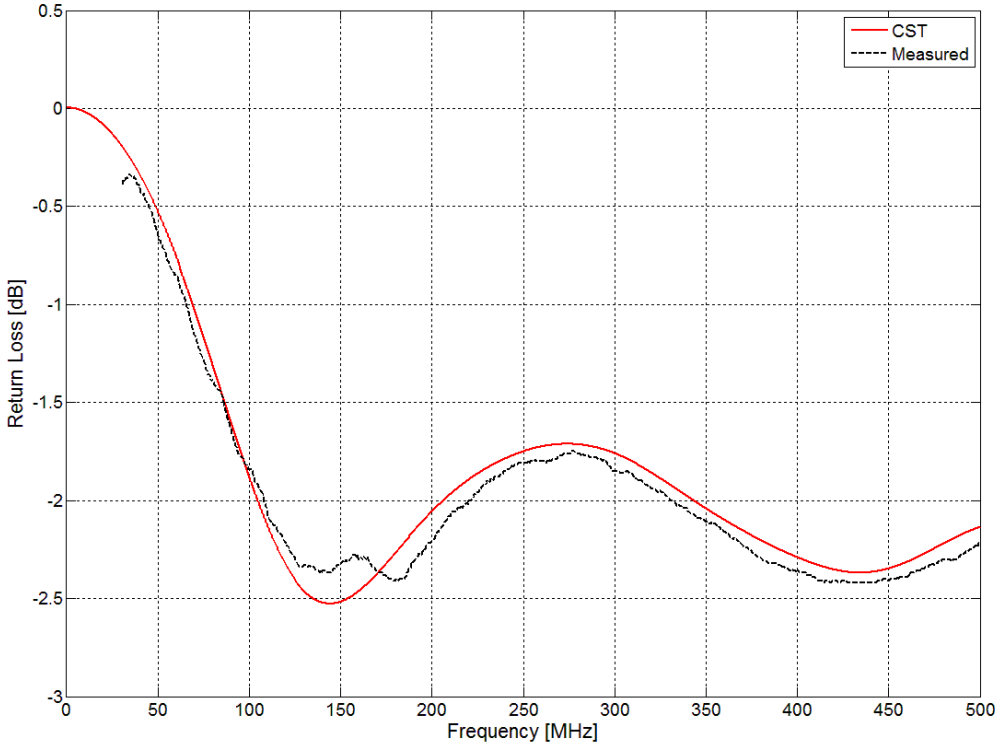

Figure D7: The CST prediction versus the measured return loss of the constructed 50cm antenna.

Good correlation was found between the measurement and the simulation. The simulations can now be used to optimise the design to a point where it meets the requirements specific to its intended purpose.

The optimised resistance values (Table D1) were obtained by parameter sweeping the resistive element values.

	Distance From Feed	**Resistance**
Z_1	10cm	56 Ω
Z_2	20cm	75 Ω
Z_3	30cm	120 Ω
Z_4	40cm	240 Ω
Z_5	45cm	470 Ω
Z_6	48.5cm	1.5 kΩ

Table D1: The lumped element parameters distance from the feed point and the element's resistance.

The antennas input impedance was found computationally by parameter sweeping the input impedance until the best return loss was achieved (Figure D8).

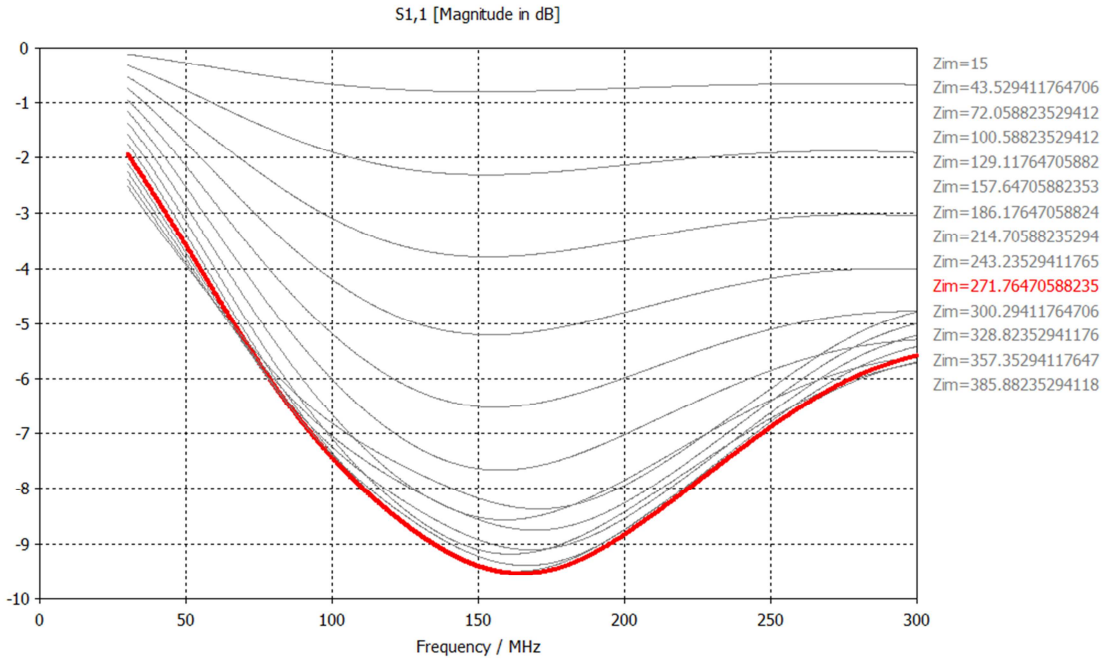

Figure D8: The CST parameter sweep of the 50cm antenna's input impedance while monitoring the return loss, S_{11}.

The loading profile for the 50cm antenna results in an input impedance of 271Ω. To improve the low frequency response, a 159Ω resistor was inserted close to the feed (1cm from the feed). The input impedance (found in the same way) was subsequently increased to 400Ω.

Confidence in the CST model's accuracy allows generation of the polar pattern (Figure D9).

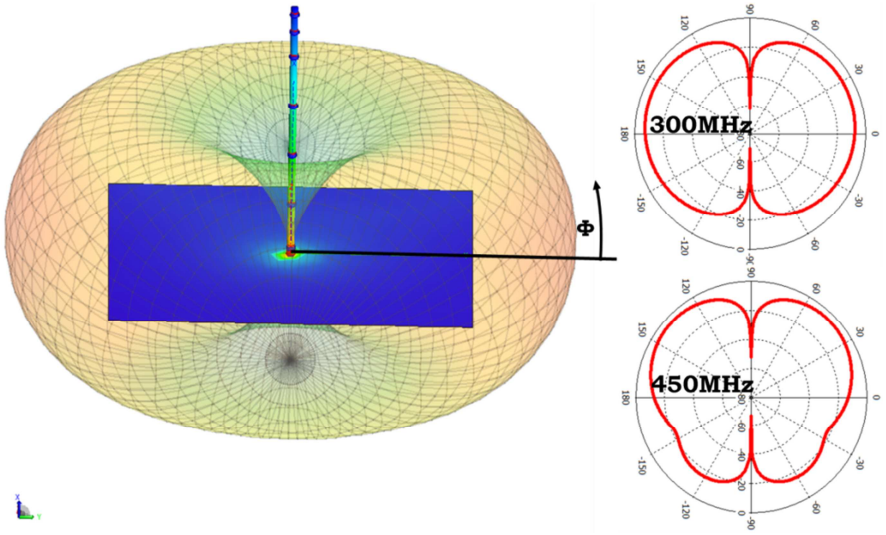

Figure D9: The polar pattern (Φ cut) of the 50cm monopole as predicted by CST.

Characterising low frequency antennas can be done at the open area test site (OATS) or at Stellenbosch University's antenna range. It is, however, best to characterise the antenna in its intended environment – mounted on the antenna.

D.3 The Monopole's Ground Plane

The ideal reflector is the same size for the best frequency response. The ideal reflector size for the frequency range of interest (30MHz – 300+MHz) is 1.28m x 1.28m. In an attempt to negate this effect, the size of the ground plane was increased (in CST) by placing square bars on the reflector to increase the length of the current path (Figure D10).

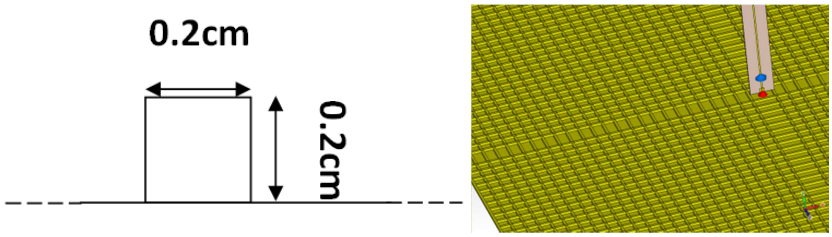

Figure D10: The square bars placed on the ground plane. The intention is to increase the effective size of the ground plane to increase the return loss of the antenna.

50 bars were placed in a grid formation along the length and width of the reflector to make up a pattern as shown in Figure D10. This allows a reflector size of 50cm x 50cm and yields the results in Figure D11.

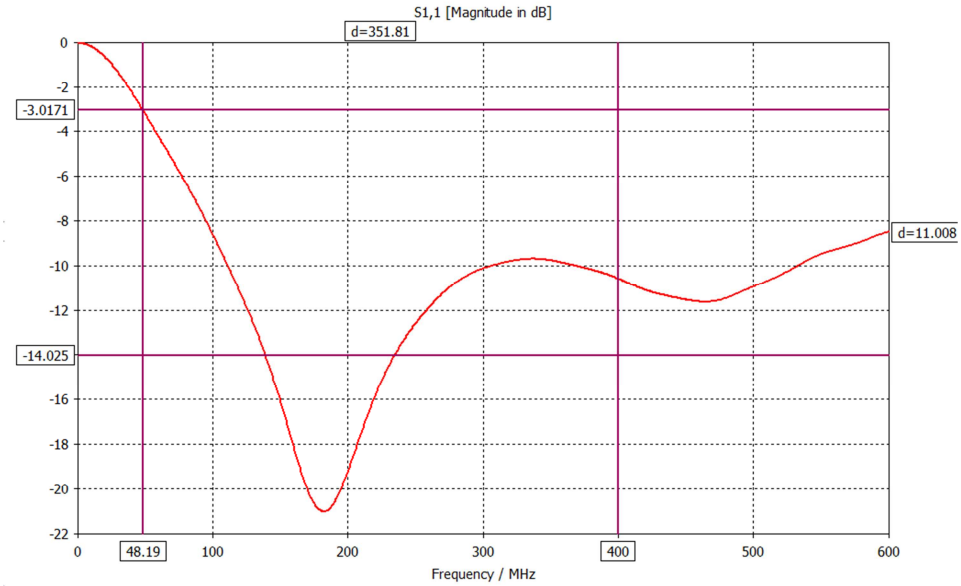

Figure D11: The antenna return loss with the modified grid ground plane.

It can be seen that the S_{11} is appreciably better (5dB at 180MHz). The extra length for the current path does not affect the radiation pattern. The main lobe direction, however, is increasing – this is called beam elevation. Other ground planes were experimented with to study the effect on return loss and beam elevation (Figure D12).

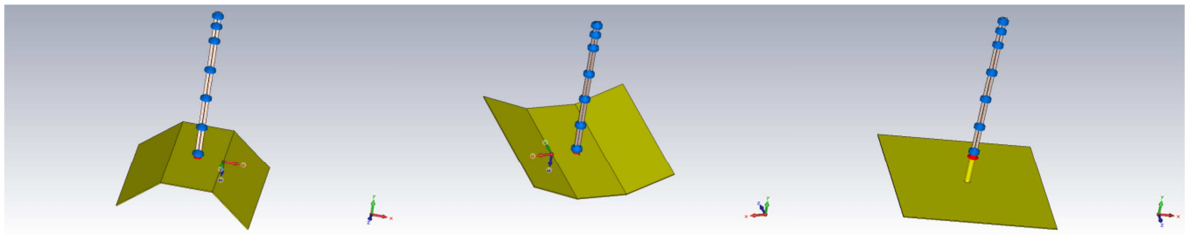

(a) (b) (c)

Figure D12: The different ground planes experimented with which performed the best.

The main lobe direction is indicated by the angle Φ as in Figure D13.

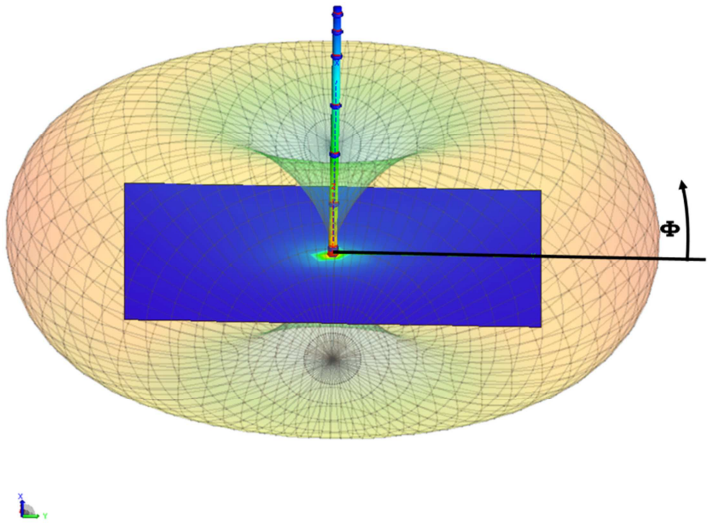

Figure D13: The main lobe direction is indicated by Φ in Table D2.

The best-performing ground plane configurations are presented in tabular form in Table D2, showing the return loss at discrete frequencies as well as the beam elevation angle, Φ.

S_{11} Φ	180MHz	300MHz	400MHz	450MHz	500MHz
Matched	-16dB	-9dB 22°	-8.6dB 35°	-9.1dB 40°	-8.4dB 44°
Corrugated Figure D10	-21dB	-10dB 26°	-10.4dB 39°	-11.4dB 44.5°	-11dB 47.5°
Bent Upwards Figure D12(a)	-20.6dB	-10dB 25°	-10.8dB 39°	-11.5dB 43.5°	-11.2dB 45°
Bent Inwards Figure D12(b)	-22dB	-10.6dB 26°	-11dB 38°	-12.2dB 44°	-11.7dB 48.5°
Elevated Figure D12(c)	-29dB	-12dB	-14dB	-10.5dB	-7.7dB

Table D2: The comparison of the return loss and the main lobe direction between the different reflector schemes.

While the results are encouraging, the improved performance in the band of interest (up to 300MHz) is not worth the extra weight or compromising the mechanical integrity further. It was therefore decided to stick with a rectangular tin ground plane of appropriate size for mounting on the UAV.

D.4 Finalised Antenna Results

An RF transformer from Coilcraft was used to match the 400Ω antenna to 50Ω (Figure D14).

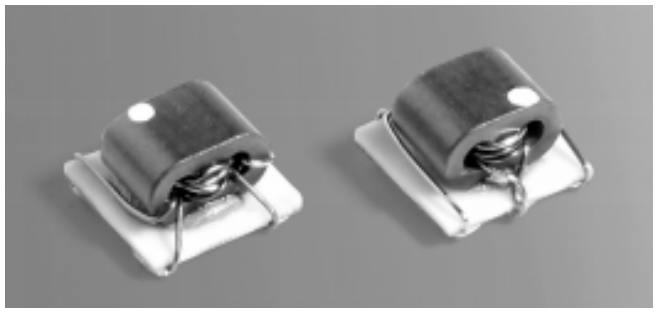

Figure D14: The 1:8 RF transformer (WBC8-1LB) from Coilcraft used to match the antenna to 50Ω.

The 1:8 WBC8-1LB RF transformer is operable from 0.15 – 600MHz (Figure D15) and has a 0.6dB insertion loss.

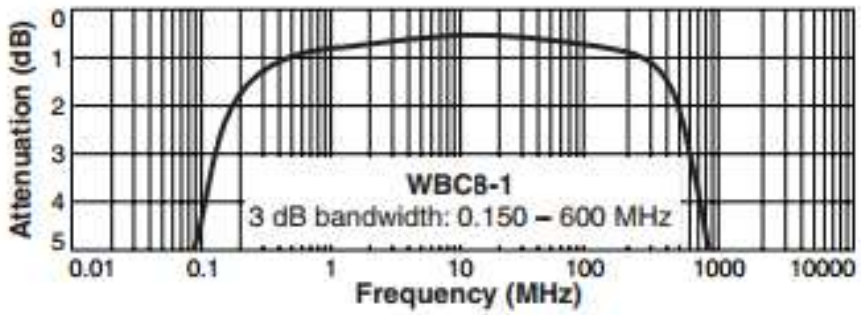

Figure D15: The bandwidth of operation of the WBC8-1LB RF transformer.

Once the antenna was matched, the return loss was once again measured on ZVB8 VNA (Figure D16).

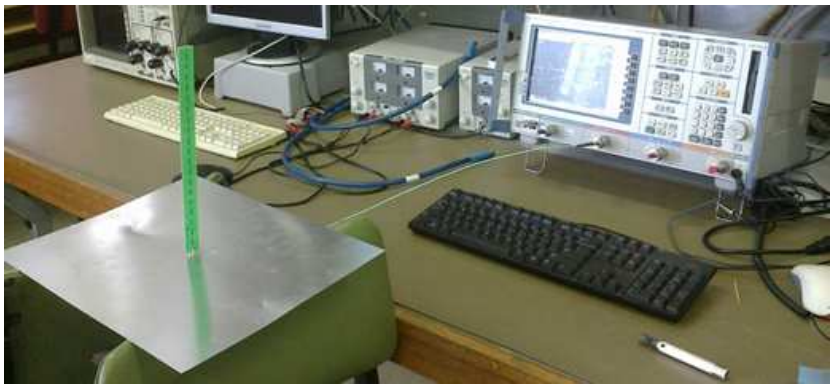

Figure D16: Measuring the return loss of the 25cm resistively-loaded monopole antenna.

The matched and unmatched antenna measurements are compared in Figure D17.

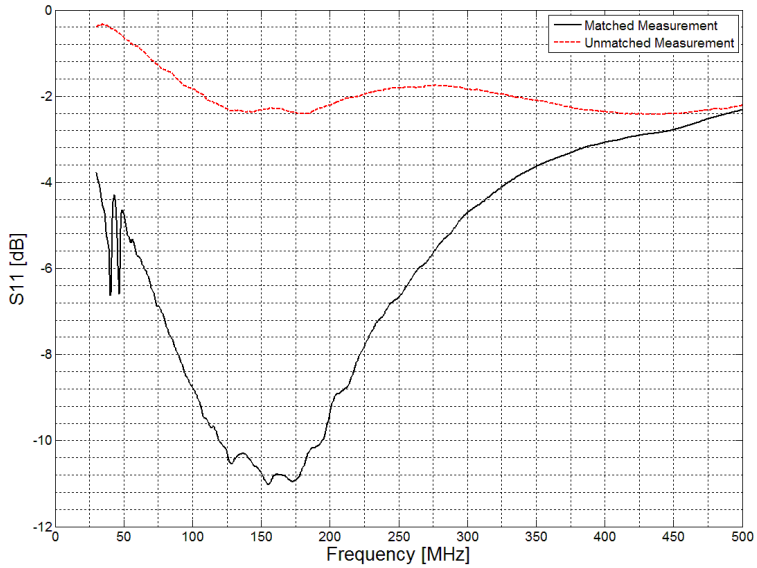

Figure D17: The 50cm antenna's return loss – comparison between the matched and unmatched antenna.

The measured return loss shows that the 50cm antenna is operable in the 30 – 400MHz range. A rough calibration can be done with the antenna mounted on the UAV to determine the polar pattern of the system at various heights.

The 12.5cm antenna was constructed and packaged in Styrofoam and heat shrink. The small, compact shape of the antenna allows for easy mounting as shown in Figure D18.

Figure D18: The 12.5cm antenna mounted on the UAV.

The 50cm antenna is more difficult to mount and cannot be packaged in the same way. Mounting this large antenna is only possible in a vertical orientation (Figure D19).


Figure D19: The 50cm antenna mounted underneath the UAV.

D.5 Conclusions

Three resistively-loaded monopole antennas were designed for their consideration in aerial (UAV) measurements.

The 12.5cm monopole antenna covers the range from 400MHz-4GHz, the 25cm from 200MHz-2GHz and the 50cm from 40MHz-350MHz.

Although the resistively-loaded antennas were not used, due to technical challenges and time constraints, it is recommended that their use be revisited for aerial measurement campaigns. Their broad bandwidth, beam-width and small size offer great advantage in field measurements of this kind. When sensitivity is an issue, LNAs can be inserted into the measurement chain.

D.6 References

[1] T.T. Wu and R.W.P King, "The Cylindrical Antenna with Non-Reflecting Resistive Loading", IEEE Trans. Antennas Propag., pp. 369-373, May 1965.

[2] B.K. Woods, Development of an Active Pulsed Radar Received for a Mono-Static Borehole-Radar Tool, March 2003, Masters Thesis.

[3] [Online]. Available: Coilcraft, http://www.coilcraft.com/, Last visited, August 2013.